Magneto-Raman spectroscopy in the regime of the persistent spin helix

Dissertation
zur Erlangung des Doktorgrades der Naturwissenschaften
(Dr. rer. nat.)
der Fakultät für Physik der Universität Regensburg

vorgelegt von

Sven Gelfert
aus Bayreuth

im Jahr 2020

Das Promotionsgesuch wurde eingereicht am: 29.04.2020
Die Arbeit wurde angeleitet von: Prof. Dr. Christian Schüller.

Prüfungsausschuss:	Vorsitzender:	Prof. Dr. Gunnar Bali
	1. Gutachter:	Prof. Dr. Christian Schüller
	2. Gutachter:	Prof. Dr. Sergey Ganichev
	weiterer Prüfer:	Prof. Dr. Josef Zweck

Contents

Chapter 1

Introduction

The fast progress of digitalization and connectivity is encountering increasingly complex limits in its technical realization. Not only in the aspect of environmental protection we are obliged to design modern technologies in a resource-saving and energy-efficient manner. It is also important to develop better encryption techniques to ensure data security in the future. The progress in information technology has been mainly dominated by semiconductor-based devices, where data encoding and processing is implemented by means of the electrical charge of electrons. Since the development of the first transistor in the year 1948 [Bar48] and the invention of integrated electric circuits [Kil63, Kil76] with a structure size in the micrometer range, advances in information technology have so far been achieved by scaling down the device sizes and reaching higher transistor densities. Modern conventional CMOS[1] transistors are approaching length scales of single atoms and molecules, where parasitic resistances and capacitances [Tho06], as well as quantum mechanical tunneling of charge carriers are limiting factors. This is associated with an increasing power consumption and an uncontrollable heat production of modern devices. The demand for more computing power is thus in contrast to an energy-efficient future and requires new concepts.

Interestingly, a possible way out might me to harness complex quantum mechanical effects instead of viewing them as an invincible barrier. A very promising candidate is the field of the semiconductor-based spintronics, where the magnetic dipole moment of electrons is utilized instead of their charge. This field was pioneered by P. Grünberg and A. Fert in the year 1988 with the discovery of the giant magnetoresistant (GMR) effect [Bai88, Bin89]. The implementation of this technology in commercial hard drives enabled a drastic increase of the storage capacity and paved the way for

[1] CMOS: complementary metal oxide semiconductor

a rapid development in computer technology. Another very prominent concept in the field of spintronics was proposed by S. Datta and B. Das in the year 1990: the so-called spin field-effect transistor [Dat90]. In such a device, spin-polarized electrons are injected into a semiconducting channel where they travel ballistically to a detection contact. Inside this channel region, dominated by spin-orbit coupling, the spins perform a precession movement, which can be manipulated via an external gate. Because of a "spin-dependent" transmission, the spin at the detection contact is either blocked or let passed, depending on its orientation. This corresponds to the off/on state of a transistor. The realization of such a device was demonstrated at operating temperatures in the millikelvin range [Koo09]. However, the ballistic electron transport makes the controllability of the spin precession very error-prone and impedes its commercial realization. A promising candidate to circumvent this problem is the so-called nonballistic spin transistor, proposed in the year 2003 by J. Schliemann [Sch03]. It takes advantage of a unique spin-orbit field symmetry, arising from an interplay of the Bychkov-Rashba [Byc84b] and the Dresselhaus [Dre55] spin-orbit field. By balancing the strengths of both contributing fields, the spins arrange in a helical structure, which is often referred to as the persistent spin helix (PSH). Thus, the spin transport through the channel is tolerant against spin-independent scattering mechanisms and allows the operation in a diffusive regime. A few years later this concept was reinforced by Bernevig et al. [Ber06], who theoretically showed that the electron spin is conserved in the PSH regime, which protects the spin from dephasing. Subsequently, the first experimental evidence of the PSH was achieved by Koralek et al. [Kor09], utilizing transient spin grating spectroscopy. The first direct mapping of the PSH was demonstrated by Walser et al. [Wal12a] via time-resolved and spatially resolved magneto-optical Kerr rotation. Furthermore, photocurrent measurements from Kohda et al. [Koh12] contributed to a better understanding of the PSH.

Here, resonant inelastic light scattering (RILS) is utilized to investigate electronic excitations in two-dimensional electron systems (2DES) embedded in GaAs-AlGaAs heterostructures. This field was pioneered more than two decades ago in the seminal work of Jusserand and Richards et al. [Jus92, Ric93, Jus95, Ric96], who demonstrated the first experimental proof of the interplay between the Bychkov-Rashba and the Dresselhaus spin-orbit field via RILS. The present thesis is intended to continue the work of C. Schönhuber [Sch14, Sch16a], who investigated the spin-orbit field induced my means of spin splitting of a 2DES via RILS and was able to verify the PSH state with this method for the first time. To gain a deeper understanding of the PSH mechanisms, here, a new measurement setup with in-situ sample rotation on a rotary stage was de-

veloped, which allows us to precisely map the spin-splitting anisotropy of two different samples, each with the condition of the PSH. In particular, two configurations of the PSH, due to different doping profiles are investigated. Furthermore, the realization of various scattering geometries and the application of external magnetic fields enables the manipulation of the intrinsic spin-orbit fields of our samples. This allows us to quantitatively deduce important spin-orbit field parameters, the electron $|g|$ factor and the single-particle scattering time from our observations.

This thesis is structured as follows: In the first part of Chapter 2, a basic overview of the used semiconductor material will be presented, including the crystal structure, the electronic band structure and fundamental considerations of GaAs-AlGaAs quantum well heterostructures. Furthermore, a detailed discussion about the structural design of each used sample is given. After this, spin-orbit interaction and the resulting spin splitting induced by the Bychkov-Rashba and the Dresselhaus field contributions are elucidated. This will lead us to the special situation, where both field parameters are of equal strengths, giving rise to the PSH state. Next, the concept of inelastic light scattering is introduced, starting with a phenomenological description of elementary electronic excitations in 2DES and a detailed discussion about intrasubband spin-density excitations in (001)-grown quantum wells. This chapter is closed by introducing the influence of external magnetic fields in our experiments.
Chapter 3 provides a description of the experimental setup, the installed magnetocryostat and the used measurement geometries for all experiments in this work. The second part of this chapter, introduces the computational Lindhard-Mermin line-shape analysis method, used for simulating the spectral line shape of intrasubband spin-density excitations.
Chapter 4 starts with the experimental characterization of all samples used in this work. In the next part, a sample with an external electric gate is examined. After basic characteristic measurements, an effective manipulation of the charge carrier density via the electric gate is demonstrated. Also a tuning of the intrinsic Bychkov-Rashba parameter can be shown by analyzing the RILS spectra. This is followed by magnetoluminescence measurements in out-of-plane external magnetic fields. Next, the impact of out-of-plane magnetic fields on spin-density excitations is elucidated. An indication of the collective character of spinflip SDE is given by a comparison with measurements in polarized measurement geometry, where non-spinflip excitations are investigated. In the last part of this chapter, in-plane external magnetic fields are utilized to manipulate the intrinsic spin-orbit fields. As a result, we can extract the effective spin-orbit

field strengths and the $|g|$ factors of our investigated samples.
Finally, all relevant measurement results are summarized in Chapter 5 together with an outlook for future studies.

Chapter 2

Basics

2.1 GaAs-AlGaAs heterostructures

For several decades, gallium arsenide has been a key material for optoelectronic devices in both science and industry. The fields of application of this direct band gap III-V semiconductor range from commercially usable infrared LEDs and high-frequency devices up to spin transistors and qubits, which play an important role in the area of quantum computing research. With advanced molecular beam epitaxy and modulation doping techniques, ternary alloys between GaAs and AlGaAs are established, forming heterostructures. By confining the dimensionality, quasi two-dimensional (2D) quantum wells with highly mobile electrons are achieved. The electron spin in such materials is mainly influenced by spin-orbit interaction, which in turn is caused by crystal symmetry and intrinsic electric fields. This section provides an overview of the material system GaAs/AlGaAs, beginning with the crystal structure and the resulting electronic properties. It is followed by the basics of a quasi 2D quantum well structure and the consequences for the confined electron states in such a system.

2.1.1 Crystal structure of GaAs

GaAs is one of the most important representatives of III-V compound semiconductors, which crystallizes in zinc blende structure. Figure 2.1 illustrates the atomic composition of its constituents. The structure can be described by shifting two face-centered cubic sublattices, one containing Gallium, the other Arsenic, shifted by $(\frac{a}{4}, \frac{a}{4}, \frac{a}{4})$ towards the space diagonal with the lattice constant $a_{\,\mathrm{GaAs}} = 5.6533\,\text{Å}$ (at $300\,\mathrm{K}$) [Pea67]. The crystal symmetry corresponds to the point group T_d, which is the same as for the regular tetrahedron, consisting of 24 symmetry operations, bringing it into coincidence

with itself [Yu96]. Because of the two-atomic basis, the zinc blende structure differs from the diamond structure and therefore has no inversion symmetry [Dre55].

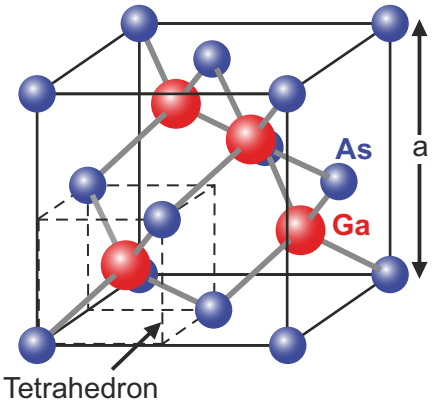

Figure 2.1 | 3D illustration of bulk GaAs in zinc blende structure. It consists of two face-centered cubic lattices of Ga and As atoms, shifted by $(\frac{a}{4}, \frac{a}{4}, \frac{a}{4})$ towards the space diagonal, with the lattice constant a. Figure taken from [Sze07] and slightly adapted.

2.1.2 Electronic band structure

The first Brillouin zone of the zinc blende lattice with its high-symmetry points described in the reciprocal lattice is sketched in Figure 2.2 (a). GaAs is a direct band gap semiconductor with its valence band maximum and the conduction band minimum located at the Γ-Point at the center of the Brillouin zone.

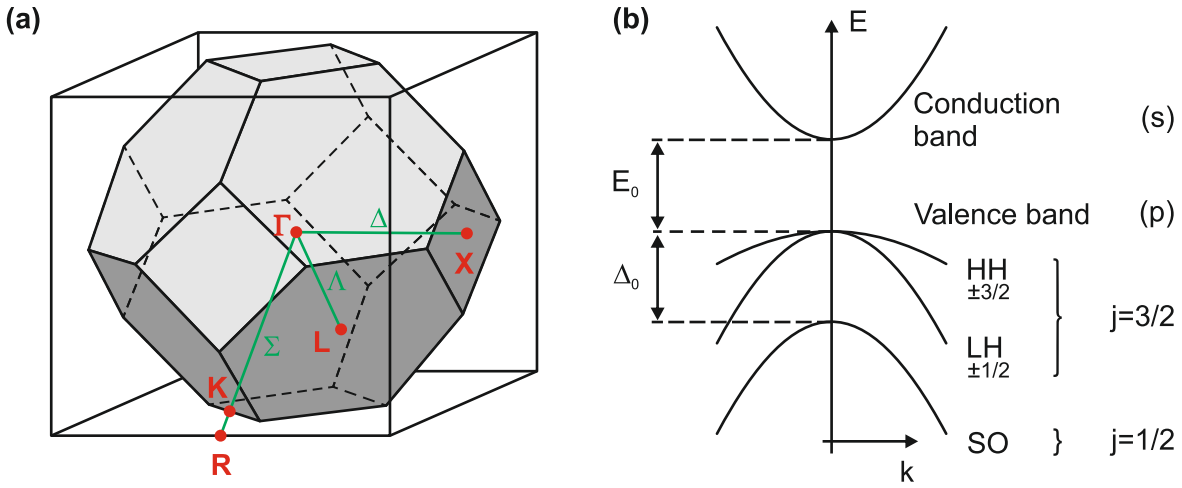

Figure 2.2 | (a) First Brillouin zone of a face-centered cubic lattice with high-symmetry points. Figure taken from [Sch06] and slightly adapted. (b) Qualitative sketch of the band structure of GaAs close to the fundamental gap at the Γ-point. Taken from [Win04].

For optical excitations with laser energies in the range of the fundamental gap, only band edges in the vicinity of the direct band gap are relevant, since the momentum

transfer of light is much smaller than the dimensions of the Brillouin zone. This makes optical spectroscopy a very powerful tool to investigate direct band gap semiconductors, because electron-hole pairs can be generated very effectively in the valence- and conduction band.
Figure 2.2 (b) depicts the band structure of bulk GaAs close to the fundamental gap at the Γ-point in an effective mass approximation. For T = 0 K, the band gap energy is $E_0 = 1.51914\,\text{eV}$ [Skr84]. Due to overlapping of the electron orbitals of neighboring atoms, new bands form: The s antibonding conduction band and three p bonding valence bands. In the s-like conduction band, two electrons may occupy the energetically lowest s orbital with the angular momentum quantum number $l = 0$ leading to a two-fold spin degeneracy $s = \pm 1/2$. For bulk GaAs, the effective mass of the conduction band is $m^* = 0.067 m_e$ [Ada85]. The angular momentum for the bonding p-like valence band orbitals is $l = 1$, resulting in the magnetic quantum number $m_j = \pm 3/2$ for the heavy hole band (HH) and $m_j = \pm 1/2$ for the light hole band (LH), which are degenerate at the Γ-point. Their names arise from the different effective masses. Due to spin-orbit coupling, the degeneracy of the so-called split-off band (SO, $m_j = \pm 1/2$) is lifted.
A detailed description of the band structure for arbitrary directions in the reciprocal space requires complex theoretical models like the pseudopotential method, which is not discussed here. For further information refer to [Che76] or [Ihn10].

2.1.3 Quantum well structure

A two-dimensional electron system (2DES) is formed by confining electrons in a quantum well. One common way is to embed GaAs in a barrier material with an increased band gap. The ternary alloy $Al_xGa_{1-x}As$ is well suitable for this purpose, where a fraction x of the Ga atoms is replaced by Aluminum (Al). By increasing the amount of x in the alloy, the magnitude of the direct band gap becomes larger and is described by [Men86]

$$E_\text{G}(x) = 1.5177 + 1.30\,x \;\; \text{(in eV)}.$$

For values of $x > 0.45$ it becomes an indirect band gap semiconductor with a minimum at the X-point of the Brillouin zone (see Fig. 2.2 (a)). However, in this work, only direct band gap materials with $x = 0.30$ and 0.33 are used.

The heterojunction of a single GaAs quantum well embedded in an AlGaAs barrier is depicted schematically in Fig. 2.3. The relative alignment of the conduction- and

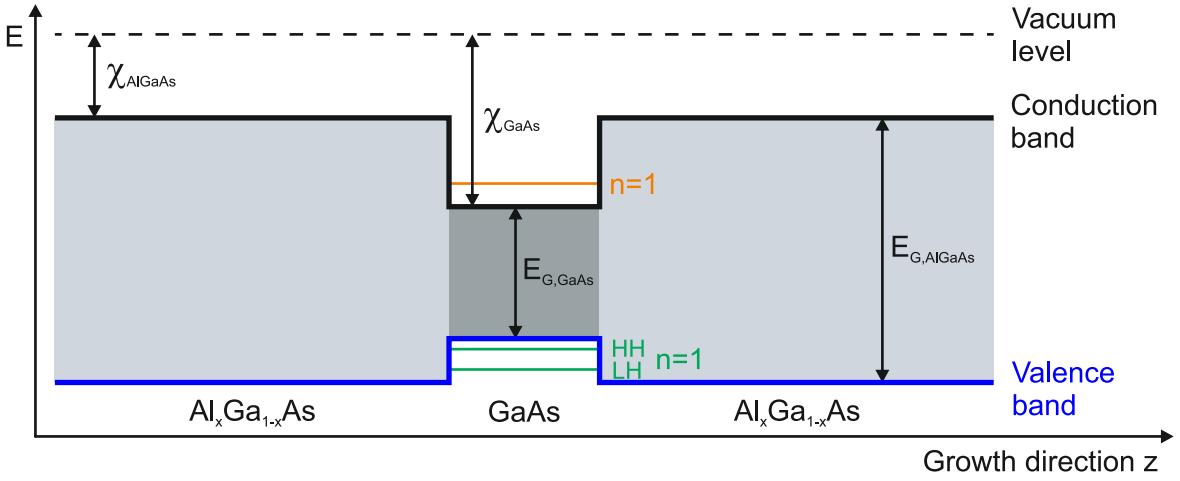

Figure 2.3 | GaAs single quantum well structure embedded in AlGaAs. The alignment of the band edges is described by Anderson's rule, based on aligning the vacuum levels. Based on [Dav97].

valence band edges (black and blue solid lines) can qualitatively be described by Anderson's rule [And62, Dav97]. This rule is based on the electron affinity χ, measuring the required energy to move an electron from the conduction band bottom to the vacuum level (dashed line). The formation of a type I heterostructure, as shown in Fig. 2.3, is the result of Anderson's rule, stating that the vacuum levels of the involved materials line up. By fabricating a thin layer of GaAs sandwiched between two thick AlGaAs barriers, one obtains a confinement of the electrons perpendicular to the growth direction in the x-y-plane and a quasi two-dimensional electron system is formed. In the simplest scenario, the energy levels of the confined electrons are approximated using the textbook example of an infinitely high potential well. They are described by [Sch04]

$$E_{n,k} = E_{n,k_z} + E_{k_\parallel} = \frac{\hbar^2}{2m^*}\left(\frac{n\pi}{d}\right)^2 + \frac{\hbar^2 k_\parallel^2}{2m^*}. \tag{2.1}$$

Here, $n > 0$ is the discrete energy subband index, d the width of the quantum well and $k_\parallel = (k_x, k_y, 0)$ the in-plane dispersion of the confined electrons. In Fig. 2.3, the lowest electron subband for $n = 1$ (solid orange line) is illustrated. As a consequence of the different effective masses m^* for the heavy- and light hole states in the valence band, a splitting of $\Delta E_{\mathrm{HH,LH}}$ at the Γ-point for $n = 1$ can directly be obtained from Eq. (2.1)

$$\Delta E_{\mathrm{HH,LH}} = \frac{1}{2}\left(\frac{1}{m_{\mathrm{HH}}} - \frac{1}{m_{\mathrm{LH}}}\right)\left(\frac{\hbar\pi}{d}\right)^2. \tag{2.2}$$

The HH and LH valence bands for this case are schematically sketched in Fig. 2.3 as

the two green horizontal lines.

2.2 Sample growth and design

In the course of this work, three different samples with highly specialized properties were investigated. This section starts with a brief introduction into the molecular beam epitaxy (MBE) method, which was used for manufacturing the samples. This is followed by a detailed discussion of the structural composition of each sample, supported by valence- and conduction band potential profile simulations, conducted with the self-consistent Poisson-Schrödinger solver "nextnano++" [Tre06, Bir07]. Also, the application process of an electrical top gate will briefly be discussed.

2.2.1 MBE growth

Figure 2.4 shows the simplified illustration of a molecular beam epitaxy chamber. The whole system is held under ultra high vacuum (background pressure below 10^{-11} mbar) to avoid contamination with impurities and to increase the mean free path of molecules between collisions to operate in the molecular-flow regime of a gas (also called Knudsen regime). The furnaces containing the elements to be deposited are called Knudsen cells (K-cells). They have individual orifices pointing towards the sample holder which are controlled by mechanical shutters. When a shutter is opened, the evaporated substance inside a K-cell is forming a molecular beam that enters the MBE chamber and is deposited on the substrate layer by layer. For optimal growth conditions, the substrate is heated and rotated during the deposition. The whole process is monitored, utilizing RHEED (reflected high-energy electron diffraction), where an electron beam is scattered at the sample surface in grazing geometry. For each fully grown monolayer, the scattered intensity of the electron beam, displayed on a screen, differs from incomplete layers, resulting in a periodically changing signal from which the grown layer number can be measured very precisely.

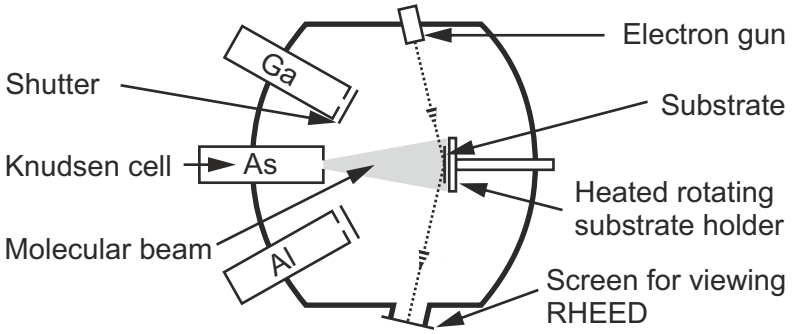

Figure 2.4 | Schematic cross section of a MBE chamber in top view. Taken from [Dav97].

2.2.2 Investigated samples

All three samples used in this work are n-doped, 12 nm wide GaAs/AlGaAs quantum wells grown in [001] and [110] crystal direction. A prerequisite of the structural composition was to choose all growth parameters deliberately to obtain a special symmetry of the intrinsic spin-orbit coupling, forming a persistent spin helix regime (see Sec. 2.3.3). An overview over the important sample parameters is given in Table 2.1.

Sample name	z	δ-profile	Density n ($10^{15}\frac{1}{\mathrm{m}^2}$)	Mobility μ ($10^6\frac{\mathrm{m}^2}{\mathrm{Vs}}$)	$\lvert\alpha\rvert = \beta$ (meV Å)	|g| factor	m*/m$_0$	$\boldsymbol{B}_{\mathrm{SO}}$ (Tesla)	Wafer name
A	001	dsd	2.7 (5.0)	(33)	3.50	0.17	0.079	18	D110831A
B/B*	001	ssd	5.8 (5.9)	(84)	-3.25	0.24	0.079	18	C130117A
C	110	dsd	(5.0)	(60)					D160408A

Table 2.1: Overview of all investigated samples with their most important parameters. The values in brackets were determined by the manufacturer using magneto-transport measurements. All other values were extracted from optical measurements in this work. The abbreviations "dsd" and "ssd" stand for double sided doping and single sided doping.

Sample A

The wafer of this n-doped [001]-grown GaAs-$Al_xGa_{1-x}As$ ($x = 0.30$) sample was manufactured at the ETH Zürich under guidance of Prof. Werner Wegscheider in collaboration with Gian Salis from IBM-Research Zürich. It was designed to reach balanced strengths of the Bychkov-Rashba (α) and Dresselhaus (β) parameters (see Sec. 2.3). Since the strength of the linear Bychkov-Rashba coefficient is determined by the built-in electric field, it was a great challenge to establish the correct doping concentrations yielding an asymmetric wave function inside the 2DES. One sample piece of this wafer was used in the experiments of Matthias Walser et al. [Wal12a] where for the first time a direct mapping of the helical spin state could be shown in time-resolved Kerr rotation measurements (TRKR). In the work of Christoph Schönhuber et al., another sample

piece of this wafer was used and the spin splitting anisotropy for two different in-plane crystal directions via resonant inelastic light scattering experiments on intrasubband spin-density excitations was first demonstrated [Sch14]. From our spectroscopic data (see Sec. 4.6.1) we could extract the electron density of $n = 2.7 \times 10^{15}\,\mathrm{m}^{-2}$ (see Tab. 2.1). It is lower than the value which was determined in magneto-transport measurements by the manufacturer ($n = 5.0 \times 10^{15}\,\mathrm{m}^{-2}$). This deviation could stem from a redistribution of electrons from the quantum well to the ionized donors inside the barriers due to laser radiation. Another reason for this quite large difference could be due to fluctuations in the donor distribution, since different pieces of the wafer were used. The mobility of this sample is $\mu = 33 \times 10^6\,\frac{\mathrm{m}^2}{\mathrm{Vs}}$.

A schematic growth pattern of this sample is sketched in Fig. 2.5 (a), where the growth direction (z) points from left to right. The sample hosts a nominally 12 nm-wide single quantum well, located 100 nm below the sample surface and has a so-called inverted doping profile with its dominant Silicon δ-doping layer grown before the quantum well. It is separated by a 20 nm AlGaAs barrier from the quantum well, preventing the ionized donors to act as scatterers in the 2DES region to ensure a high electron mobility. The secondary doping layer was grown for fine tuning of the intrinsic electric field, which is present due to structure inversion asymmetry (see Sec. 2.3.2). The two superlattices located near the GaAs substrate are consisting of thin GaAs/AlGaAs layers, and are designed to prevent impurity atoms from entering the quantum well region during the growth process. An inverted doping profile is not commonly used, because dopants can "float" into the quantum well region during the growth process and act as impurities, reducing the mobility of the 2DES.

Figure 2.5 (b) shows the valence- and conduction band potential profile, simulated with the self-consistent Poisson-Schrödinger solver "nextnano++". The exact doping concentrations are unknown, but the ratio between dominant and secondary doping is known to be 5:1, so for the simulation, the total doping concentration amount was varied until the simulation output of the electron density matched the optically measured value $n = 2.7 \times 10^{15}\,\mathrm{m}^{-2}$ (see Table 2.1). At the sample surface, a 5 nm thick GaAs cap layer is grown to prevent oxidation of the AlGaAs barrier. Due to δ modulation doping, a space-charge zone emerges from positively charged Si atomic nuclei leading to a bending of the potential curvature towards lower energies at the two doping regions. Figure 2.5 (c) is a zoom into the quantum well region of the conduction band with the squared envelope wave function $|\chi_0|^2$ (orange line) of the lowest confined subband level that can be interpreted as the probability density of electrons. The asymmetric con-

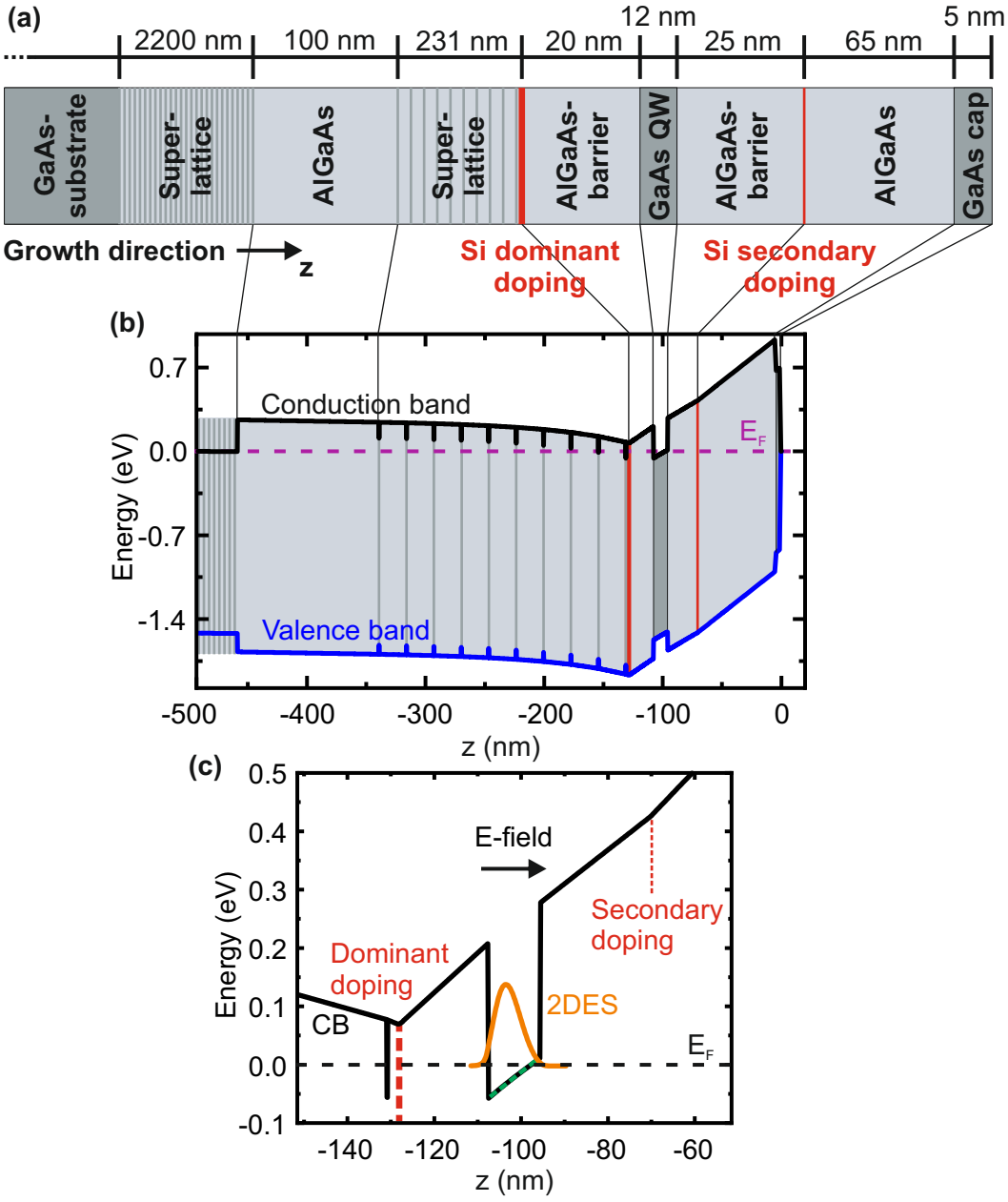

Figure 2.5 | (a) Schematic growth pattern of sample A (not to scale). The growth direction (z) points from left to right. The different Si-doping concentrations lead to an asymmetric band edge profile. (b) Potential profile of the valence- and conduction band computed with "nextnano++". (c) Zoom into the quantum well region of the conduction band potential profile (black solid line) with the probability density of electrons $|\chi_0|^2$ (orange line). The green dotted line follows the conduction band potential curvature inside the QW and is sketched for comparison with sample B (see Fig. 2.6 (c)).

centration of the two doping layers leads to the formation of an electric field, pointing in growth direction (see Fig. 2.5 (c)). Therefore $|\chi_0|^2$ has an asymmetric shape with its maximum inclined to the left side (in direction of the substrate). From the simulations

of Fig. 2.5 (b), we extract a transition energy of $E_G \sim 1.5319\,eV$ by measuring the distance between the first quantized states of electrons in the conduction band and heavy holes in the valence band inside the quantum well region.

Sample B

This n-doped, [001]-grown GaAs-$Al_xGa_{1-x}As$ ($x = 0.33$) wafer was fabricated at the University of Regensburg in the group of Prof. Dominique Bougeard. As for sample A, the aim was to achieve balanced Bychkov-Rashba (α) and Dresselhaus (β) strengths. In contrast, here a single sided doping profile, where the doping layer is grown after the quantum well to reduce incorporation of donor impurities inside the quantum well during the growth process was used. A piece of the same wafer was also used in the work of Markus Schwemmer et al. [Sch16b], where the authors demonstrated the existence of a persistent spin helix state for this sample utilizing time-resolved Kerr rotation measurements. The electron density $n = 5.9 \times 10^{15}\,m^{-2}$ and the mobility $\mu = 84 \times 10^6\,\frac{m^2}{Vs}$ were determined by the sample grower. Again there is a deviation for the extracted value from our spectroscopic data $n = 5.8 \times 10^{15}\,m^{-2}$ (see Tab. 2.1 and Sec. 4.6.1). The higher mobility compared to sample A is possibly explained by the single-side doping profile: On the one hand, impurities inside the quantum well are minimized due this growth technique as stated before. On the other hand, the electrons are more confined on one side of the quantum well, reducing the scattering on interface imperfections compared to a double-sided doping, where the electrons "feel" two interfaces [Sch06].
Figure 2.6 (a) illustrates the schematic sample structure with the growth direction pointing to the right side. It has a simplified growth structure, compared to sample A. The quantum well with a nominal thickness of 12 nm is located 500 nm below the surface. Between quantum well and doping layer is a 20 nm AlGaAs barrier. Figure 2.6 (b) sketches the conduction- and valence band profile simulated with "nextnano++".
A zoom into the quantum well region is shown in Fig. 2.6 (c). Due to the doping layer on the right side, the intrinsic electric field points to the left hand side (in direction of the substrate), vice versa as in sample A. This causes the probability density of electrons $|\chi_0|^2$ to be inclined towards the sample surface (orange line). Because the quantum well is markedly deeper below the sample surface as compared to sample A, and there is no doping layer between quantum well and substrate, the slope of the conduction band on both sides of the quantum well is significantly different. On the substrate side it is nearly horizontal, whereas facing towards the doping layer, it is very steep. This has a considerable effect on the curvature of the conduction band at the

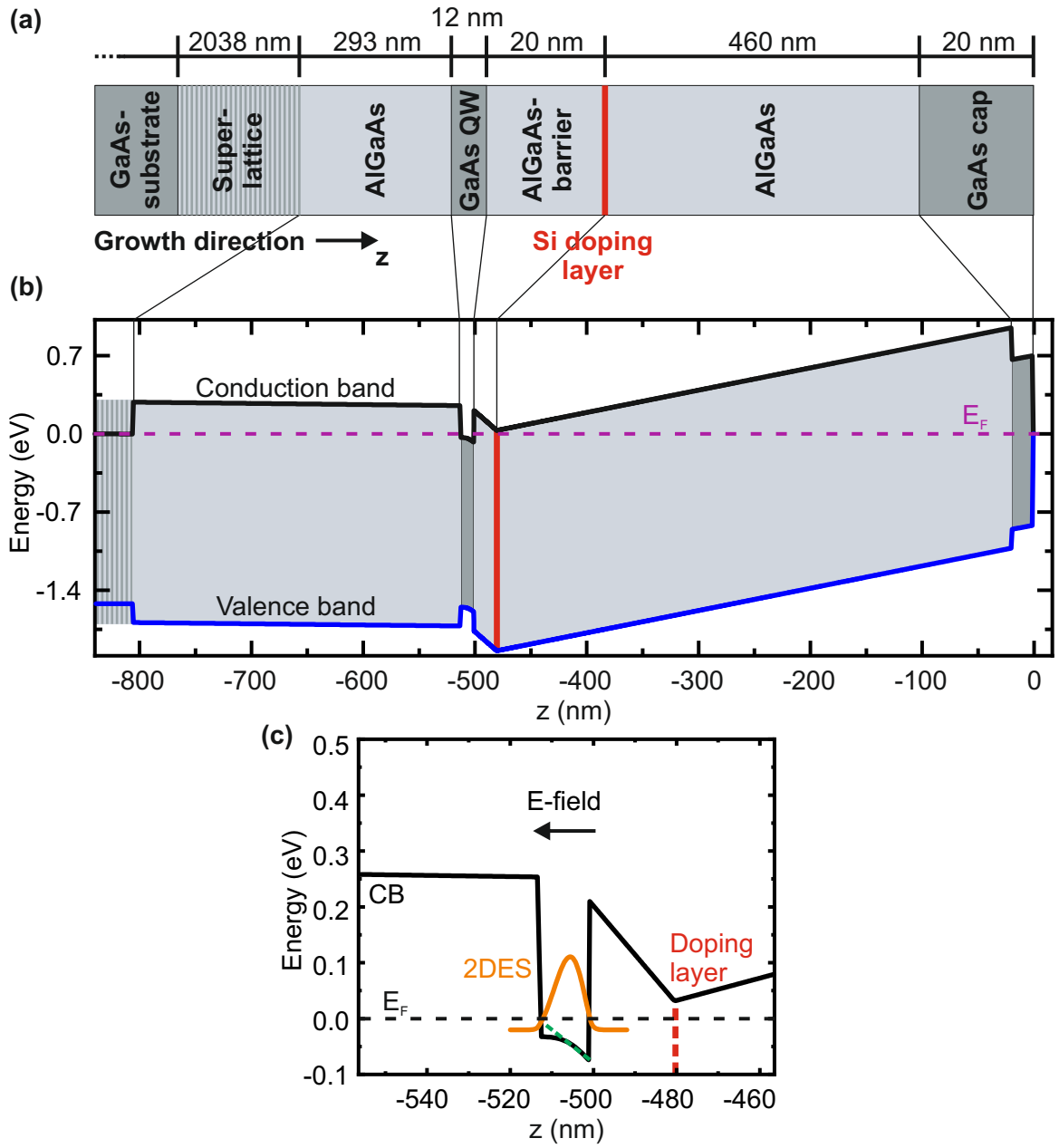

Figure 2.6 | (a) Schematic growth pattern of sample B (not to scale). The growth direction (z) points from left to right. Compared to sample A, the simpler design with one-sided doping on the opposite side also leads to an asymmetric band edge profile. (b) Potential profile of the valence- and conduction band computed with "nextnano++". (c) Zoom into the quantum well region of the conduction band potential profile (black solid line) with the probability density of electrons $|\chi_0|^2$ (orange line). The green dotted line follows the conduction band potential curvature inside the QW and is sketched for comparison with sample A (see Fig. 2.5 (c)).

bottom of the quantum well which is quite different for both samples A and B. For comparison, the curvature of this region for sample A (see Fig. 2.5(c)) was mirrored, and plugged in Figure 2.6(c) as a green dashed line. This might be an indication that

for sample B there is no homogeneous electric field across the quantum well. From the simulation in Fig. 2.6 (b), we extract a transition energy of $E_G \sim 1.5414\,eV$, which is slightly higher than for sample A, and might originate from the increased band bending of sample B.

Sample B* (gated)

This sample stems from the same wafer as sample B, but was equipped with a semi-transparent Nickel-Chrome (Ni-Cr) top gate to apply an electric field perpendicular to the sample surface. The gate was fabricated in cooperation with Johannes Holler and Dr. Michaela Trottmann at the vapor deposition chamber of Prof. Dominique Bougeard in the cleanroom of the University of Regensburg. Here, we will give a brief overview about the top gate fabrication process, a detailed description can be found in previous publications from our research group [Kug12, Gra17]. Figure 2.7 (a) shows a sectional view of sample B*. The 2DES is used as a back gate contact. By applying a voltage between the back- and the top gate, electrons are injected or depleted in the 2DES, depending on the polarity of the voltage. Before the Ni-Cr top gate is applied in the vapor deposition chamber, the desired top gate position is delimited by applying Scotch©-tape to shade the area, where the back gate contacts should be installed, avoiding a short circuit between top- and back gate. Next, $\sim 15\,nm$ Ni-Cr are deposited in a vapor deposition chamber. At this thickness, the top gate is semitransparent, and its transmission ratio is measured to be ~ 0.5 in transmissivity experiments. To establish a contact to the 2DES, the top gate free sample surface area, which was shaded before with Scotch-tape, is scratched with a Tungsten pin and four separated solder points of Indium are applied and subsequently alloyed at $350\,°C$ for 60 seconds in a furnace under forming gas atmosphere. In the last step, the sample is mounted on a circuit board (see Fig. 2.7 (b)), where the four back gate contacts and two top gate contacts are bonded with gold wires to larger connection panels to be installed inside the cryostat.

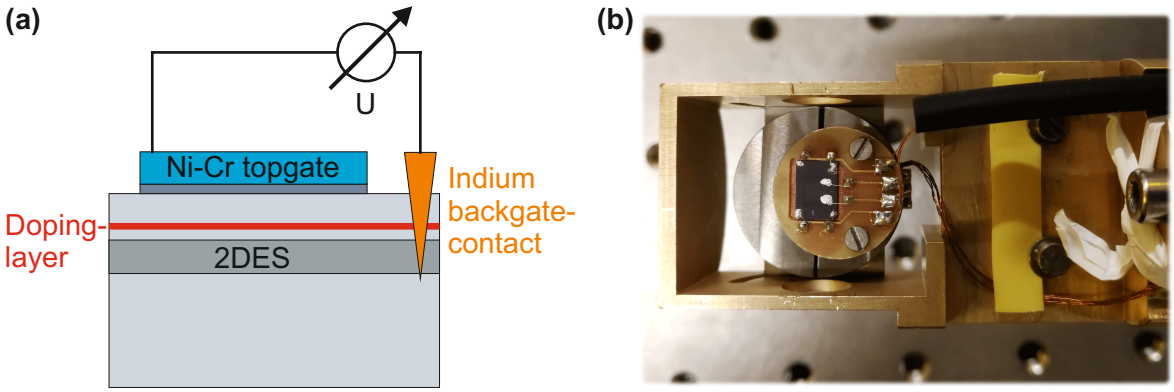

Figure 2.7 | (a) Schematic cross section of sample B* with Ni-Cr top gate and back gate contacts. (b) Sample B* mounted on the circuit board, attached to the cryostat insert.

Sample C

In the course of this work, an attempt was made to examine the persistent spin helix state in grazing-incidence measurements, utilizing resonant inelastic light scattering experiments. Therefore Prof. Wegscheider supplied us with a [110]-grown GaAs-$Al_xGa_{1-x}As$ ($x = 0.30$) sample, hosting a 12-nm wide single quantum well with symmetric doping profile. With this doping symmetry, no structure inversion asymmetry is present in the 2DES, and the apparent spin-orbit interaction is only due to the Dresselhaus contribution, which points out-of plane for [110]-growth direction (see Sec. 2.3.1). In this special case, a persistent spin helix (PSH) regime forms for the out-of plane direction (see Sec.2.3.3).

Figure 2.8 (a) sketches the sample structure with the growth direction pointing to the right hand side. The 12 nm wide quantum well is located 230 nm below the surface and is embedded in a 58 nm thick AlGaAs barrier. It is symmetrically doped with three doping layers. The utilized doping technique is called quantum well doping [Uma09], where every Silicon doping layer lies inside a thin, 2 nm wide GaAs single quantum well, surrounded by 1 nm AlAs barrier material. The ratio of the doping concentrations was set by the manufacturer to 80:72:40 (shown in Fig. 2.8 (a) as QW doping 1-3).

The resulting "nextnano++" band edge profile simulation of the conduction band in the quantum well area is shown in Fig. 2.8 (b). Located on the left and right hand side of the 2DES, the spikes in the conduction band stems from the AlAs barrier material of the quantum well doping layers, the Silicon doping is marked as the red dashed lines. The simulation was conducted in the same way as for sample A and B, by fixing of the doping concentration ratio for all QW doping layers, until the resulting electron density was consistent with the specified value $n = 5.0 \times 10^{15}\,\mathrm{m}^{-2}$ (see Tab. 2.1.) The

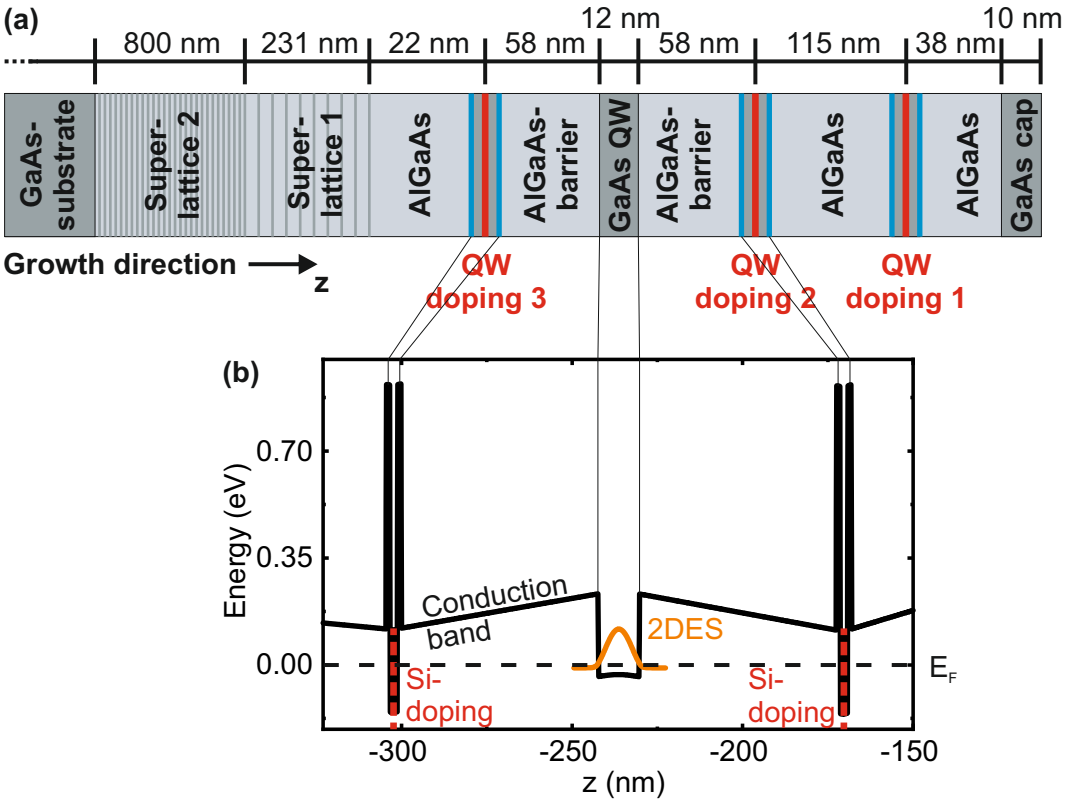

Figure 2.8 | (a) Schematic structural composition of sample C (b) Band edge profile simulation of the quantum well region of sample C.

orange line shows the probability density $|\chi_0|^2$ of electrons inside the quantum well. Due to the symmetrical slope of the conduction band in the quantum well region, no electric field along the growth direction is present, as it is the case for sample A and B. The extracted transition energy from the simulation is $E_G \sim 1.5463\,\text{eV}$.

2.3 Spin-orbit interaction

Spin-orbit (SO) interaction describes the interplay between the spin and orbital degrees of freedom of the electrons. The SO interaction originates from a relativistic description, where a moving electron in an electric field "feels" an effective magnetic field. The interaction of the spin of the moving electron and this effective magnetic field is then referred to as spin-orbit interaction. This section will outline the two main contributions to spin-orbit coupling in GaAs-AlGaAs semiconductor heterojunctions and the resulting lifting of the spin degeneracy in 2DES. The interplay of both contributions, originating from the bulk inversion asymmetry (BIA) and the structure inversion asymmetry (SIA), is leading to the formation of a persistent spin helix state,

which will be discussed at the end of this section.

The relativistic interaction between electron spin and orbital angular momentum leads to an additional splitting of the energy bands for $|\boldsymbol{k}| > 0$. The corresponding spin-orbit interaction Hamiltonian derives from the Dirac equation and is written as [Fab07]

$$H_{\mathrm{SO}} = -\frac{\hbar}{4m_0^2c^2}\boldsymbol{\sigma} \cdot \boldsymbol{p} \times (\nabla V_0). \tag{2.3}$$

Here, $\boldsymbol{p}$ is the momentum operator of the involved particle, $\boldsymbol{\sigma}$ is the vector of Pauli matrices and m_0 is the free electron mass.

In semiconductor heterostructures, this intuitive picture becomes more complicated, since confinement effects cause band bending, creating an intrinsic electric field (see Sec. 2.2.2). In addition, moving electrons in polar semiconductors such as GaAs are subjected to a periodically changing potential, and the effect of this potential on the spin of the electron can be described by a $\boldsymbol{k}$-dependent magnetic field $\boldsymbol{B}_{\mathrm{eff}}(\boldsymbol{k})$. Therefore, the symmetry of a semiconductor crystal plays an important role for the description of the spin energy eigenvalues and the spin degeneracy of such a system. For inversion symmetric crystals like Silicon, the spin-up ($\uparrow$) and the spin-down ($\downarrow$) states are degenerate:

$$E_{\uparrow}(\boldsymbol{k}) = E_{\downarrow}(\boldsymbol{k}), \tag{2.4}$$

which is a consequence of the combined effect of inversion symmetry in space and time [Kit63]. Space-inversion symmetry changes the wave vector $\boldsymbol{k}$ into $-\boldsymbol{k}$, resulting in $E_{\uparrow}(\boldsymbol{k}) = E_{\uparrow}(-\boldsymbol{k})$ and time-inversion symmetry, besides changing $\boldsymbol{k}$, also flips the spin, resulting in $E_{\uparrow}(\boldsymbol{k}) = E_{\downarrow}(-\boldsymbol{k})$, also known as the Kramers relation [Dre55, Fab07].

There are two possible ways to lift this spin degeneracy: On the one hand, the space inversion asymmetry can be broken by internal or external electric fields even in the absence of magnetic fields, where a horizontal splitting of the parabolic subbands emerges. This is sketched in Fig. 2.9 (a). For materials like GaAs, the space inversion symmetry is already broken due to a lack of crystal inversion symmetry. On the other hand, the time inversion symmetry can be broken by applying an external magnetic field. This leads to a Zeeman splitting [Zee97] of the parabolic subbands, sketched in Fig. 2.9 (b), where a vertical splitting $\Delta E_{\mathrm{Zeeman}}$ of the parabolic subbands occurs.

As stated above, the SO-coupling-induced band splitting may be considered as an intrinsic, effective $\boldsymbol{k}$-dependent magnetic field $\boldsymbol{B}_{\mathrm{SO}}(k)$, and so Eq. (2.3) can be written as

$$H_{\mathrm{SO}} = \frac{\hbar}{2}\boldsymbol{\Omega}(\boldsymbol{k}) \cdot \boldsymbol{\sigma}, \tag{2.5}$$

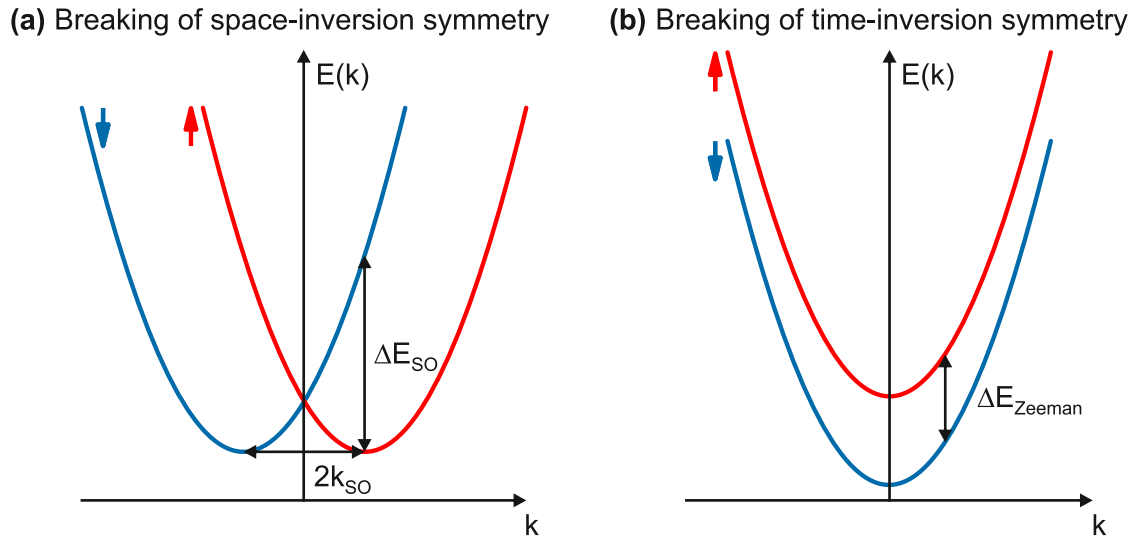

Figure 2.9 | The parabolic spin-split subbands of the lowest conduction band are sketched for two cases: (a) Breaking of the space-inversion symmetry is leading to a horizontal subband splitting, where for $|\boldsymbol{k}| > 0$ the energy splitting ΔE_{SO} is determined by the strength of the spin-orbit interaction. (b) Breaking of the time-inversion symmetry is leading to a vertical splitting $\Delta E_{\mathrm{Zeeman}}$ of the subbands, also known as Zeeman splitting.

with the Larmor precession vector $\boldsymbol{\Omega}(\boldsymbol{k}) = (g\mu_B/\hbar)\,\mathbf{B}_{\mathrm{SO}}(\boldsymbol{k})$.
One usually differentiates between three different space inversion asymmetries: The bulk inversion asymmetry (BIA), the structure inversion asymmetry (SIA) and the natural interface asymmetry (NIA). In GaAs, the impact of NIA is negligibly small, since it originates from heterostructure interfaces in which the adjacent layers share no common atom (e.g. InAs) [Kre96, Win03, Dya08]. For the present work on GaAs, BIA and SIA is essential and will be discussed in more detail below.

2.3.1 Bulk inversion asymmetry - BIA

The lack of inversion symmetry in zinc blende III-V compounds like GaAs (see Sec. 2.1.1), gives rise to a spin splitting of the energy dispersion in bulk materials at zero external fields. This was theoretically proposed by G. Dresselhaus [Dre55], who derived an expression for the Larmor precession vector from Eq. (2.5) by using general group-theoretical arguments. In the lowest order of perturbation theory, $\boldsymbol{\Omega}(\boldsymbol{k})$ is cubic in $\boldsymbol{k}$ and has the following form[1]:

$$\boldsymbol{\Omega}(\boldsymbol{k})_{\mathrm{BIA,\ bulk}} = \frac{2\gamma}{\hbar}\,[k_x\,(k_y^2 - k_z^2),\ k_y\,(k_z^2 - k_x^2),\ k_z\,(k_x^2 - k_y^2)]^T. \tag{2.6}$$

[1]The superscript ^{T} means "transpose".

It includes the material-dependent spin-splitting Dresselhaus parameter [Dya71, Dya86, Žut04]

$$\gamma = \frac{\alpha_D \hbar^3}{m^* \sqrt{2 m^* E_g}}. \tag{2.7}$$

The dimensionless parameter α_D expresses the magnitude of the Dresselhaus SO-field strength. For moderately n-doped bulk GaAs, a value of $\alpha_D = 0.07$ was experimentally determined [Mar83]. Additionally, the Dresselhaus SO coupling strength depends on the effective electron mass m^*, and the band gap size E_g.
The spin-splitting Dresselhaus parameter γ depends on the confinement energy of the quantum well and the penetration depth of the wave function into the barrier material. For a higher confinement energy, the value of γ decreases [Win03]. In quantum wells, the orientation of the Dresselhaus SO field depends on the growth direction, since the wave function is confined and momentum $\hbar k_z$ quantizes along the growth direction.

001-grown quantum well

By choosing a coordinate system with k_z pointing in growth direction, i.e., $x \parallel [100], y \parallel [010], z \parallel [001]$, Eq. (2.6) can be expressed for a 2DES, substituting the quantized momentum k_z by its expectation value $\langle k_z \rangle = 0$ and $\langle k_z^2 \rangle = (\pi / d_{\mathrm{qw}})^2$, with d_{qw} being the quantum well width [Dya86, Žut04]:

$$\boldsymbol{\Omega}(\boldsymbol{k})^{[001]}_{\mathrm{BIA,\ 2D}} = \frac{2\gamma}{\hbar} \left[k_x \left(k_y^2 - \langle k_z^2 \rangle \right),\ k_y \left(\langle k_z^2 \rangle - k_x^2 \right),\ 0 \right]^T. \tag{2.8}$$

In a 2DES, cubic terms in the in-plane momentum are often neglected. This is justified, since the in-plane momentum $(k_\parallel)^2$ is much smaller than $\langle k_z^2 \rangle$ for the samples presented in this thesis. With this, the Larmor frequency of the Dresselhaus SO field can be approximated, and is written as

$$\boldsymbol{\Omega}(\boldsymbol{k})^{[001]}_{\mathrm{BIA,\ 2D,\ linear}} = \frac{2\beta}{\hbar} \left[k_x,\ -k_y,\ 0 \right]^T. \tag{2.9}$$

β is called the linear Dresselhaus parameter, and is given by $\beta = -\gamma \langle k_z^2 \rangle$. Note that γ is negative for GaAs [Wal12b]. A sketch of $\boldsymbol{\Omega}(\boldsymbol{k})$ is shown in Fig. 2.10 (a). It only has components lying in the 2DES plane. The strength of the Dresselhaus SO field is expressed by the parameter β, that will be experimentally determined later in this work (see Sec. 4.6.1).

110-grown quantum well

The symmetry of the Dresselhaus field changes significantly when the crystal is grown in different crystallographic directions. For a GaAs heterostructure grown along the [110]-crystal direction, one typically chooses a coordinate system with $x \parallel [1\bar{1}0], y \parallel [00\bar{1}], z \parallel [110]$. For a 2DES in $\boldsymbol{k}$-linear approximation the Dresselhaus SO field can be expressed as [Dya86, Has97]

$$\boldsymbol{\Omega}(\boldsymbol{k})^{[110]}_{\text{BIA, 2D, linear}} = \frac{2\beta}{\hbar}\,[0,\ 0,\ k_x]^T. \tag{2.10}$$

For this case, $\boldsymbol{\Omega}(\boldsymbol{k})$ is sketched in Fig. 2.10 (b). The Dresselhaus SO field points along the growth direction.

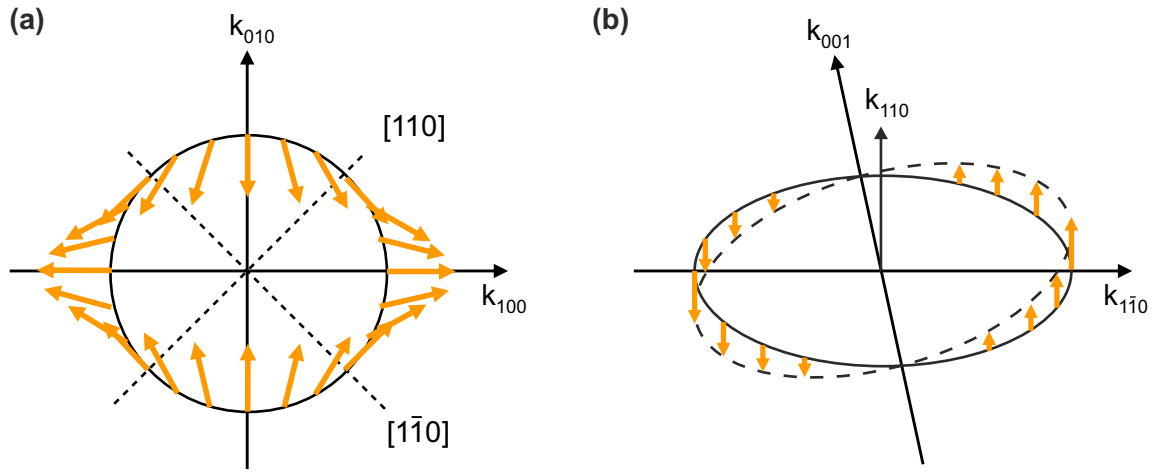

Figure 2.10 | (a) Orientation of the linear Dresselhaus SO field for a 2DES grown in [001]-direction at the Fermi level (black circle). The orientation and amplitude of $\boldsymbol{\Omega}(\boldsymbol{k})$ is represented by the orange arrows. (b) Linear Dresselhaus SO field for a 2DES grown in [110]-direction. $\boldsymbol{\Omega}(\boldsymbol{k})$ is pointing out of the 2DES plane for every direction of $\boldsymbol{k}$.

2.3.2 Structure inversion asymmetry - SIA

For low-dimensional semiconductors with an asymmetric conduction band potential profile (cf. Fig. 2.5 (c)), which can be realized by, e.g., different alloy compositions or single-sided modulation doping, intrinsic electric fields may arise alongside the growth direction and break the space inversion symmetry, which is often referred to as the Bychkov-Rashba effect [Ras60, Byc84a, Byc84b]. The same effect can also be induced by external electric fields via electrical gates [Nit97, Stu09].

As we have seen previously for BIA, the contribution of SIA can be considered as an effective magnetic field coupling to the spin degree of freedom, as shown in Eq. (2.5).

In lowest order in $\boldsymbol{k}$ and $\boldsymbol{E}$ it is given by

$$\boldsymbol{\Omega}(\boldsymbol{k})_{\mathrm{SIA}} = \frac{2\alpha_R}{\hbar}\,\boldsymbol{k} \times \boldsymbol{E}. \tag{2.11}$$

Here, α_R is a material dependent parameter, and has been determined for GaAs, using an extended Kane model as $\alpha_R = 5.2$ eÅ^2 [Win03]. For electric fields pointing parallel to the growth direction z, which is the case for asymmetrically doped GaAs/AlGaAs heterostructures, Eq. (2.11) can be expressed as

$$\boldsymbol{\Omega}(\boldsymbol{k})_{\mathrm{SIA}} = \frac{2\alpha}{\hbar}\,[k_y,\, -k_x,\, 0]^T. \tag{2.12}$$

Here, the common Bychkov-Rashba parameter $\alpha = \langle \alpha_R E_z \rangle$ is obtained by averaging the electric field and the material dependent parameter over barrier and quantum well. $\boldsymbol{\Omega}(\boldsymbol{k})_{\mathrm{SIA}}$ from Eq. (2.12) is sketched in Figure 2.11. It is independent of the growth direction and always lies in the quantum well plane, perpendicular to the electron $\boldsymbol{k}$-vector. The sign of α is determined by the orientation of the electric field E_z and therefore may be tuned to positive or negative values.

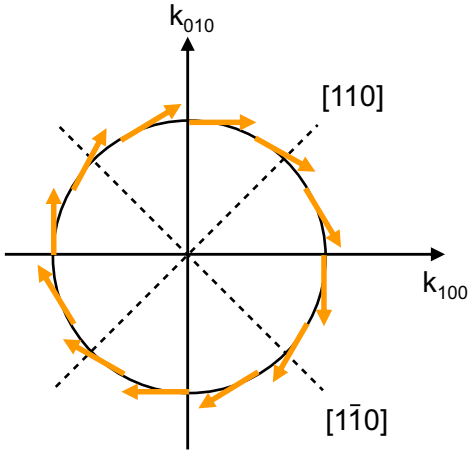

Figure 2.11 | Orientation of the Bychkov-Rashba SO field at the Fermi surface, for an electrical field E_z pointing in [001] growth direction.

In semiconductor heterostructures, the interplay of both the Dresselhaus and the Bychkov-Rashba SO field are of great interest. Experiments to separate these two effects were presented by Ganichev et al. [Gan04], who used the spin-galvanic effect in photocurrent measurements to deduce the ratio between Dresselhaus and Bychkov-Rashba SO field for different samples. For future spintronic devices, a configurable SO interaction would be of great benefit. In contrast to the Dresselhaus SO contribution, which is determined by the crystal structure of the used material, the Bychkov-Rashba SO contribution can be modified not only by intrinsic fields, arising from an asymmetric doping profile in the growth process, but also temporarily via external gating.

Nitta et al. [Nit97] were the first who demonstrated the tunability of SO interaction in a 2DES, using a top gate electrode by investigating Shubnikov-de Haas oscillations. However, in this study, no separation between Dresselhaus and Bychkov-Rashba SO-field effects was possible. In the work of Studer et al. [Stu09], a tuning of just the Bychkov-Rashba SO coupling was achieved using back- and top gate in time-resolved Kerr rotation measurements. They found a linear dependence between the externally applied field (perpendicular to the 2DES) and the Bychkov-Rashba induced SO-field strength α and could determine its sign.

2.3.3 The persistent spin helix

We have seen that the previously introduced Dresselhaus and Bychkov-Rashba SO-coupling mechanisms can both be present in two-dimensional semiconductor heterostructures. In [001]-grown GaAs quantum wells, these fields lie in the 2DES plane (cf. Fig. 2.10 (a) and Fig. 2.11). For the distinct case of balanced strengths of the SO contributions, i.e., $|\alpha| = \beta$, the resulting total effective SO field forms a unidirectional SO field that gives rise to a special spin rotation symmetry, the so-called persistent spin helix (PSH). Based on this, Schliemann et al. [Sch03] proposed a nonballistic spin-transistor which has gained a lot of interest in spintronic research, e.g., [Kor09, Wal12a, Koh12]. In such a device, the spin transport is tolerant against spin-independent scattering mechanisms. An external gate is used to switch between the two states $|\alpha| = \beta$ and $|\alpha| \neq \beta$, which allows to switch spin dephasing on and off. A few years later, this concept was reinforced by Bernevig et al. [Ber06], with a proposal exploiting the SU(2) symmetry of the spin, present in such systems which should lead to the formation of a PSH. The remarkable suppression of spin dephasing is explained by the fact that spin precession depends only on the traveling direction parallel to the helix direction (maximum strength of the SO field), whereas for the perpendicular direction no SO field is present. Thus, in such a nonballistic spin-transistor device, the spin information transport is independent of the traveling direction through the device. The first experimental proof of this PSH state was subsequently demonstrated by Koralek et al. [Kor09] using transient spin-grating spectroscopy. In the work of Walser et al. [Wal12a] a direct mapping of the PSH was realized using time-resolved Kerr rotation measurements. Via weak (anti-) localization experiments on gated samples, Kohda et al. [Koh12] showed, that the PSH-type state is relatively robust if $|\alpha| \sim \beta$ are comparable without external gate voltage. With this prerequisite, the PSH state is still present even when α is detuned via a gate voltage.

Most important for the present work are the experiments from Schönhuber et al. [Sch14], where a huge spin splitting anisotropy stemming from the unidirectional effective SO field in a GaAs-AlGaAs sample with $\alpha \sim \beta$ was shown, utilizing resonant inelastic light scattering experiments. The sample used in this work is from the same wafer as in Ref. [Wal12a].
However in GaAs, the PSH state is not only limited to the [001] growth direction. As we have seen in Sec. 2.3.1, for the [110] growth direction, the Dresselhaus field has also a unidirectional character (see Fig. 2.10 (b)). Consequently in such a structure, without Bychkov-Rashba SO interaction, a PSH state for out-of plane crystal directions is present. This was experimentally investigated by Chen et al. [Che14]. Kammermeier et al. [Kam16] predicted that the PSH state is achievable for any n-doped zinc-blende semiconductor quantum well, with the prerequisite that the growth direction points along an axis where two of the Miller indices have the same modulus.

Now we will focus on the symmetry of the effective spin-orbit field for the [001]-grown samples used in the present work, only considering terms linear in $\boldsymbol{k}_{\parallel}$ for the Bychkov-Rashba and Dresselhaus contributions. The intrinsic electric field of sample A is pointing along the growth direction (see Fig. 2.5 (c)), which induces a Bychkov-Rashba SO field, oriented in clockwise direction (cf. Fig. 2.11).
By adding up the Bychkov-Rashba (Eq. (2.12)) and the Dresselhaus SO field (Eq. (2.9)), one obtains the total effective SO field

$$\boldsymbol{\Omega}(\boldsymbol{k})_{\mathrm{SO}}^{\mathrm{linear}} = \frac{2}{\hbar}\,[(\alpha k_y + \beta k_x)\boldsymbol{e}_x - (\alpha k_x + \beta k_y)\boldsymbol{e}_y]. \tag{2.13}$$

Here, the typical coordinate system $x \parallel [100], y \parallel [010], z \parallel [001]$, with z pointing in the growth direction is used. When Bychkov-Rashba and Dresselhaus contributions are balanced, i.e., $\alpha = \pm\beta$, Eq. (2.13) reduces to

$$\boldsymbol{\Omega}(\boldsymbol{k})_{\mathrm{SO}}^{\mathrm{linear}} = \frac{|\alpha| + \beta}{\hbar}\,(k_x \pm k_y)(\boldsymbol{e}_x \mp \boldsymbol{e}_y). \tag{2.14}$$

The resulting effective magnetic field $\mathbf{B}_{\mathrm{SO}}$ ($\boldsymbol{\Omega}(\boldsymbol{k}) = (g\mu_B/\hbar)\,\mathbf{B}_{\mathrm{SO}}(\boldsymbol{k})$) is sketched in Fig. 2.12 (a) for $\alpha = \beta$. For every wave vector $\boldsymbol{k}$, $\mathbf{B}_{\mathrm{SO}}$ (orange arrows) is pointing (anti-) parallel towards the $[1\bar{1}0]$ crystal direction, directly showing the unidirectional character of the effective SO field.

The parabolic dispersion for the quasi-free electrons with spins (anti-) parallel to $[1\bar{1}0]$ splits into two symmetrical shifted paraboloids at the Fermi contour of the 2DES, which

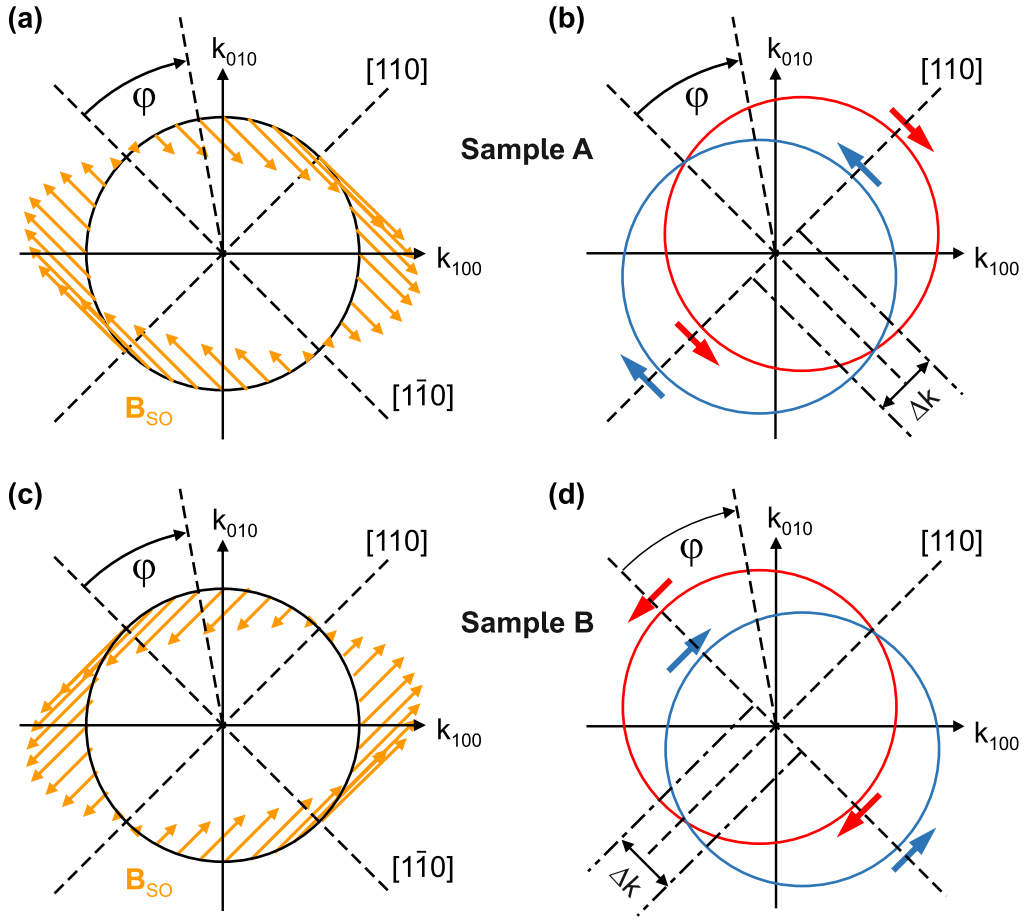

Figure 2.12 | (a) Schematic of the unidirectional effective spin-orbit field $\boldsymbol{B}_{\mathrm{SO}}$ of a 2DES with balanced Bychkov-Rashba and Dresselhaus spin-orbit strengths $\alpha = \beta$ (sample A). The angle φ is measured clockwise with respect to the $[\bar{1}10]$ in-plane direction. (b) Fermi contour for spins parallel and antiparallel to $\boldsymbol{B}_{\mathrm{SO}}$ for sample A. (c) Schematic picture of $\boldsymbol{B}_{\mathrm{SO}}$ for sample B ($\alpha = -\beta$). (d) Fermi contour for sample B.

is schematically shown in Fig. 2.12 (b). The maximum displacement Δk_{110} along the [110] crystal direction for $\alpha = \beta$ (sample A) is given by [Ber06]

$$\Delta k_{110} = \frac{4m^*\alpha}{\hbar^2}. \tag{2.15}$$

For arbitrary in-plane $\boldsymbol{k}$ directions (denoted by φ), the displacement of the two parabolas can be calculated by geometric considerations, and is written as [Sch16a]

$$\Delta k_{\varphi} = \Delta k_{110} |\sin\varphi|. \tag{2.16}$$

In this work, a sample with the configuration $\alpha = -\beta$ (sample B) was also investigated. To obtain the effective SO field for this situation, the patterns in Figs. 2.12 (a) and

(b) are time-reversed and rotated clockwise by 90°, so the effective SO field is pointing (anti-) parallel to the [110] crystal direction, which is depicted in Figs. 2.12 (c) and (d).

2.4 Inelastic light scattering on 2DES

Raman spectroscopy was pioneered by Chandrasekhara Venkata Raman, who was awarded the Nobel price in physics for his discovery in 1930 [Ram28]. This non-destructive, optical technique has become indispensable for understanding the structure of matter in chemistry and physics. The applications range from scientific interest to automated material characterization devices in industry. In solids, various elementary excitations (phonons, magnons, etc.) can be accessed by Raman scattering. Historically, the scattering on optical phonons and internal molecule vibrational modes are called Raman scattering, whereas scattering on acoustic phonons is referred to as Brillouin scattering. In two dimensional electronic systems, scattering mediated by electronic excitations is commonly called inelastic light scattering [Sch06]. The main focus in the present work is on resonant inelastic light scattering (RILS) by intrasubband spin-density excitations which will be explained in this section. First experimental evidence of the interplay between Bychkov-Rashba [Byc84b] and Dresselhaus [Dre55] spin-orbit interaction in GaAs-AlGaAs quantum wells was presented in the seminal work of Jusserand and Richards et al. [Jus92, Ric93, Jus95, Ric96], utilizing RILS spectroscopy.
Let us start with the general concept of inelastic light scattering, followed by an overview about electronic elementary excitations in 2DES, elucidating the theory of single-particle transitions and collective charge- and spin-density excitations. Then, the resonant scattering processes will be discussed, covering the scattering cross section and the polarization selection rules. Finally, the intrasubband spin-density excitations, which are important for the experimental part of this work, will be considered.

General concept

An incoming photon with energy $\hbar\omega_I$ either creates or annihilates an excitation inside the material with energy $\hbar\omega$ (depending, e.g., on the material temperature). After the scattering process, the energy of the emitted photon $\hbar\omega_S$ has either increased (Antistokes, "+") or lowered (Stokes, "−") by the amount of $\hbar\omega$. The energy and

momentum conservation law of the scattered photon is then given by

$$\begin{aligned} \hbar\omega_S &= \hbar\omega_I \pm \hbar\omega, \\ \boldsymbol{k}_S &= \boldsymbol{k}_I \pm \boldsymbol{q}. \end{aligned} \tag{2.17}$$

In this work, only experiments at low temperatures were performed. Under this circumstance the intrinsic excitations in the material may be neglected, and only the Stokes process is of importance. All inelastic light spectra shown in the present work are displayed with a relative energy axis, where $E = 0$ represents elastic scattering, i.e., $\hbar\omega_S = \hbar\omega_I$, and the energy axis is flipped horizontally. This convention is done for the sake of simplicity, since the Stokes excitations would otherwise be located at negative energies.

A major advantage of inelastic light scattering is the possibility to transfer a finite quasi-momentum, or wave vector, represented by $\boldsymbol{q}$ in this work, into the investigated system during the scattering process. This allows a detailed study of spin-orbit coupling effects in 2DES semiconductor heterostructures, since with the transfer of a momentum $\boldsymbol{q}$, time-reversal symmetry is broken in the quantum-well plane, and spin-splitting effects can be observed (see Sec. 2.3). In exact backscattering geometry, the maximum transferred momentum is twice the momentum of the incoming photon, and is calculated by [Sch06]

$$q_{\max} = \frac{4\pi}{\lambda_I}. \tag{2.18}$$

Here, the difference of the incoming and scattered wavelength is neglected ($\lambda_I = \lambda_S$), since the excitation energy is small compared to the incident laser energy. In quantum wells with lateral 2DES, the translational symmetry is not conserved in growth direction, so that a quasi-continuous momentum transfer is only possible parallel to the 2DES plane. This is realized by tilting the sample towards the incident laser direction, enabling a tunable momentum transfer into the 2DES system. A detailed discussion of the utilized measurement geometries is given in Sec. 3.1.3.

2.4.1 Elementary electronic excitations in 2DES

In GaAs-AlGaAs heterostructures hosting 2DES, inelastic light scattering experiments give rise to electronic excitations, which are typically distinguished between charge density excitations (CDE) and spin-density excitations (SDE). Also single-particle excitations (SPE) exist in such systems. The nature of SPEs was discussed controversially,

since they were first subjected to be excluded from collective effects [Pin89]: Under certain conditions, many-particle effects may partly cancel, so that the energies are close to single-particle excitations of a noninteracting system. However, it has turned out, that they actually have collective character [Sar99, Sch06], but historically they are labeled SPEs.

Single-particle transitions

Let us start by discussing single-particle transitions in n-doped 2DES, where only the lowest conduction band is occupied. At this point all collective effects are neglected. In Fig. 2.13 (a) the two lowest conduction bands, which are three dimensional rotational symmetric paraboloids, are depicted as a 2D cut in the k_x-, k_y-plane. One distinguishes between intersubband transitions, taking place between different subbands (blue arrows), or intrasubband transitions within an occupied subband (green arrow). These transitions have to be initiated at an occupied state below the Fermi energy E_F, and end at an unoccupied state above E_F. Every transition contributes to the single-particle continuum, sketched in Fig. 2.13 (b). If no wave vector is transferred into the 2DES plane ($q = 0$), which is the case for exact backscattering geometry (see Eq. (2.18)), only intersubband transitions are possible. This transition is shown as the straight vertical arrow in Fig. 2.13 (a). In parabolic approximation, these transitions lead to a discrete energy between the equally spaced energy parabolas $n = 0$ and $n = 1$. By transferring

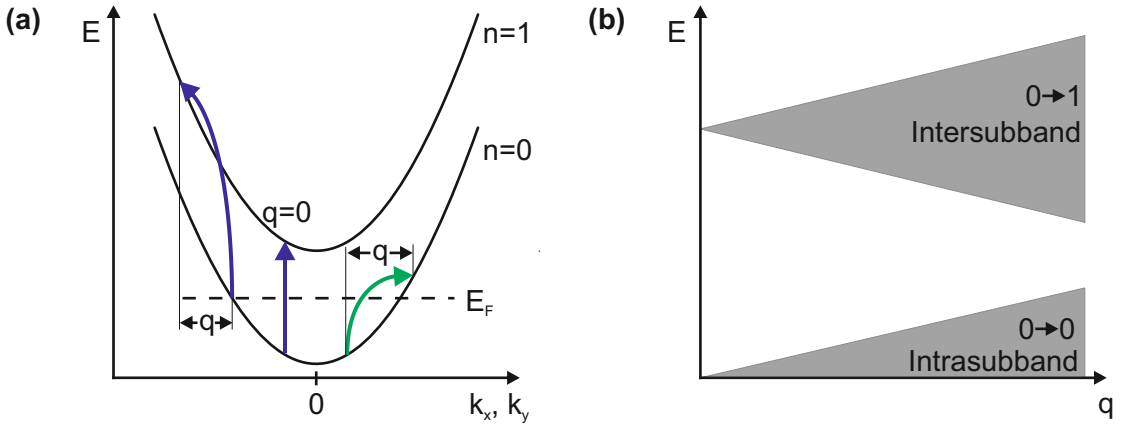

Figure 2.13 | (a) Schematic of the two lowest conduction bands in a 2DES with the Fermi energy E_F lying in the lowest $n = 0$ band. The blue arrows are indicating intersubband single-particle transitions, and the green arrow indicates an intrasubband single-particle transition. (b) Single-particle continua for all possible intersubband and intrasubband transitions in and between $n = 0$ and $n = 1$.

a finite wave vector ($\boldsymbol{q} \neq 0$) into the 2DES plane, additional intersubband excitations and intrasubband excitations are enabled (curved arrows in Fig. 2.13 (a)) and spread

into a continuum of possible transitions, shown in Fig. 2.13 (b). The unfolding into a continuum for finite wave-vector transfers can be explained by the three dimensional shape of the energy parabolas, allowing different transition energies, when considering all possible cuts in the k_x-, k_y-plane, shown in Fig. 2.13 (a). The cut in the k_x-, k_y-plane, i.e., through the paraboloid centers shown in Fig. 2.13 (a) is representing the maximum possible energy transfer for a fixed wave-vector transfer $\boldsymbol{q}$. This corresponds to the upper branch of the intrasubband continuum from Fig. 2.13 (b), and is given by [Sch06]

$$E(k_F + q) - E(k_F) = \frac{\hbar^2(k_F + q)^2}{2m^*} - \frac{\hbar^2 k_F^2}{2m^*} = \frac{\hbar^2 q k_F}{m^*} + \frac{\hbar^2 q^2}{2m^*} \simeq \frac{\hbar^2 q\, k_F}{m^*}. \tag{2.19}$$

The approximation on the right side in Eq. (2.19) is valid if the Fermi wave vector k_F is much larger than the transferred wave vector, $k_F \gg q$. The lower bound of the intrasubband continuum of zero energy is also explained by the above given argumentation, that for all wave-vector transfers $q < 2k_F$, in the 3D energy paraboloid, there exist transitions with infinitesimally small energies if one moves far enough away from the k_x-, k_y-plane. The upper and lower limits of the intersubband continuum ($n = 0 \rightarrow n = 1$), shown in Fig. 2.13 (b) are given by

$$E_{01} + E(k_F \pm q) - E(k_F) = E_{01} \pm \frac{\hbar^2 q k_F}{m^*} + \frac{\hbar^2 q^2}{2m^*}. \tag{2.20}$$

$E_{01} = E_1 - E_0$ is the spacing between the subbands for all given, but fixed in-plane (k_x, k_y) wave vectors $k_\parallel$. In Secs. 3.2 and 4.6.1, we will see, that the upper branch of the intrasubband continuum, described by Eq. (2.19) can directly be used to determine the charge-carrier density N_s from the measured spectra of intrasubband transitions via the relation

$$k_F = \sqrt{2\pi N_s}. \tag{2.21}$$

Collective charge- and spin-density excitations

Until now, only electronic excitations in an independent-particle picture have been considered. Taking collective effects into account, in 2DES, one distinguishes between charge-density excitations (CDE) and spin-density excitations (SDE). In inelastic light scattering experiments, there are underlying polarization selection rules, which will be discussed later. At this point it is stated, that CDEs are allowed in polarized measurement geometry (linear polarization of incoming and outgoing laser beam is oriented parallel to each other), whereas SDEs are allowed in depolarized geometry (linear

polarizations of both beams are oriented perpendicular to each other). Figure 2.14 gives a schematic overview of the collective electronic excitations in 2DES. CDEs (also called plasmons) are oscillations of the 2DES, where the electrons are coupled by full Coulomb interaction. In a macroscopic picture (Fig. 2.14 (a)) they can be seen as a collective, in-phase oscillation of the quasi free electrons from the 2DES against the positively charged background of the crystal lattice. In total, the charge center of mass

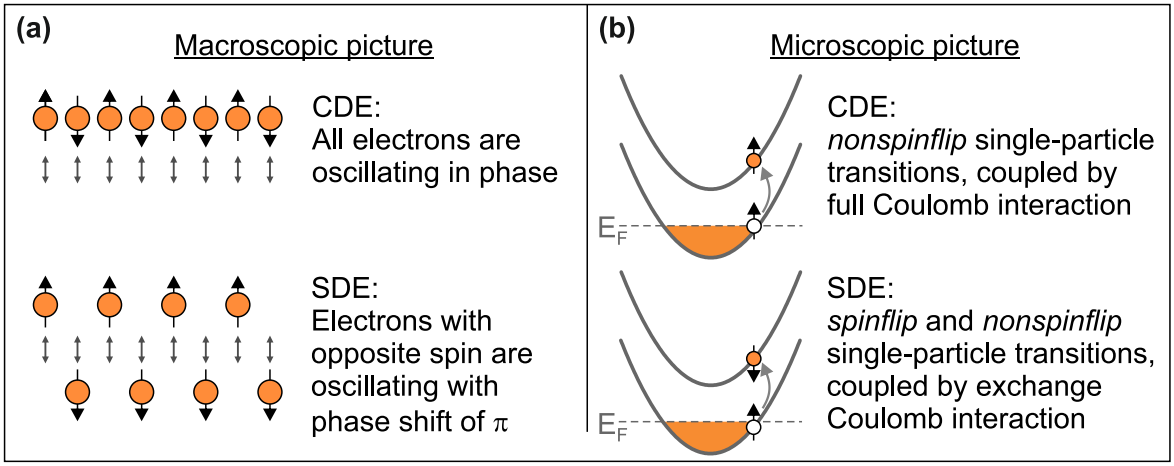

Figure 2.14 | Collective electronic excitations in 2DES in (a) macroscopic and (b) microscopic picture. Taken from [Sch06] and slightly adapted.

is performing an oscillation, which can be described in a microscopic single-particle picture (Fig. 2.14 (b)), consisting of nonspinflip single-particle transitions, coupled via the full Coulomb interaction. The direct part of full Coulomb interaction is repulsive for electrons and causes a depolarization field, shifting CDEs towards higher energies compared to SPEs. In contrast, SDEs in a macroscopic picture, can be described as electrons with opposite spin, oscillating with a phase shift of π towards each other (see bottom of Fig. 2.14 (a)). In total, this motion does not result in an oscillation of the center of mass of the charge, leading to a vanishing dipole moment. Thus, they are not subject to depolarization-field effects, only enabling exchange Coulomb interaction, which is attractive for electrons. Therefore, the energy of SDEs is redshifted compared to SPEs. In a microscopic picture, SDE transitions consist of spinflip and nonspinflip single-particle transitions, which is exemplary sketched at the bottom of Fig. 2.14 (b). It should be stressed that, in 2DES, electrons are oscillating perpendicular to the 2DES plane for intersubband transitions, whereas for intrasubband transitions (when a wave vector $\boldsymbol{q}$ is transferred into the system), electrons are oscillating in the 2DES plane.
To bridge the gap between the single-particle and the many-particle picture, Fig. 2.15 shows the single-particle continua (cf. Fig. 2.13 (b)) together with the dispersion of

the collective electronic excitations for the schematic two conduction band levels. The transitions are subscripted with numbers indicating intraband as '00' and interband as '01'. The collective character of the eigenmodes of the 2DES is only robust when their dispersion lies outside the single-particle continua. Otherwise they instantaneously decay into uncorrelated electron-hole pairs and can then be described in the single-particle picture [Wen88, Pin89, Gam90, Yu91, Gam92a, Gam92b]. This decay effect is called

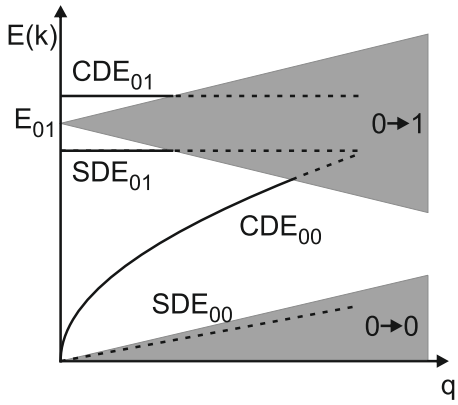

Figure 2.15 | Dispersion of collective electronic excitations, together with the single-particle continua from Fig. 2.13 (b). Taken from [Sch06] and slightly adapted.

Landau damping [Lan46], and is illustrated as the dotted lines inside the single-particle continua in Fig. 2.15. The dispersion of the intrasubband CDE_{00}-mode (depending on the in-plane wave vector $q_{\|}$) is given by [Ste67]

$$E_{\mathrm{CDE}_{00}} = \sqrt{\frac{N_S \hbar^2 e^2}{2\epsilon_\infty \epsilon_0 m^*} q_{\|}}. \tag{2.22}$$

As we can see in Fig 2.15, the CDE_{00}-mode has a square-root dependency and lies outside the single-particle continuum and is not affected by Landau damping. The intrasubband SDE_{00} mode, which is of main interest in this work, is strongly Landau damped since it lies inside the single-particle continuum for every possible wave vector. The exchange interaction is known to be rather small [Ber90], and the dispersion is described by the upper edge of the single-particle continuum (see Eq. (2.19)). The SDE_{01} and CDE_{01} are sketched in Fig. 2.15 for sake of completeness, but will not be discussed further. More information can be found in Ref. [Sch06].

2.4.2 Resonant scattering processes

In this section, a microscopic approach to the scattering mechanisms of *resonant* inelastic light scattering on electrons in 2DES will be discussed. Resonant in this context means that valence-band states are involved as intermediate states in the scattering process [Sar99]. Laser excitations in the vicinity of the optical band gap transition

energy are fulfilling a resonance condition, which is increasing the scattering cross section significantly and will be discussed later. We will see that SDEs are only visible for *resonant* conditions in inelastic light scattering experiments, whereas CDEs can also be probed in nonresonant excitation scenarios.
To describe the inelastic scattering process quantum mechanically, the transition of a photon from the initial state (ω_I, $\boldsymbol{k}_I$, $\boldsymbol{e}_I$) to the final state (ω_S, $\boldsymbol{k}_S$, $\boldsymbol{e}_S$) has to be taken into account, $\boldsymbol{e}_{I,S}$ represents the polarization vector of the corresponding incoming and scattered light. Omitting the explicit notation of $\boldsymbol{p}$ and $\boldsymbol{r}$ as operators, the Hamiltonian of the perturbed system can be written as [Sch06]

$$\begin{aligned} H &= \frac{1}{2m}\sum_i \left[(\boldsymbol{p}_i + e\boldsymbol{A}(\boldsymbol{r}_i))^2 + U(\boldsymbol{r}_i)\right] + V_{e-e} + V_{e-ph} \\ &= H_0 + \frac{1}{2m}\sum_i \left[(\boldsymbol{A}(\boldsymbol{r}_i))^2 + \boldsymbol{p}_i\boldsymbol{A}(\boldsymbol{r}_i) + \boldsymbol{A}(\boldsymbol{r}_i)\boldsymbol{p}_i\right]. \end{aligned} \tag{2.23}$$

For simplicity, spin-orbit interaction is neglected here. To consider the interaction between the incoming electromagnetic wave and the electronic system, the electron momentum $\boldsymbol{p}$ has to be replaced by $\boldsymbol{p} + e\boldsymbol{A}$ in the Hamiltonian of the unperturbed system H_0, where $\boldsymbol{A}$ is the vector potential of electromagnetic fields. The term V_{e-e} represents the Coulomb interaction, V_{e-ph} is the electron-phonon interaction and U describes the sum of lattice-periodic and external potentials. The last three terms in Eq. (2.23) can be treated as a perturbation, where $\boldsymbol{A}^2$ contributes in *first* order and $\boldsymbol{pA}$ terms in *second* order perturbation theory. If the $\boldsymbol{pA}$ terms are additionally extended by the interaction between electrons and phonons (V_{e-e}, V_{e-ph}), one gets contributions in *third* order perturbation theory. The scattering processes involving phonons V_{e-ph} will not be discussed here. In inelastic light scattering, the second-order (SOP) and third-order (TOP) scattering processes have been found to be dominant, since they include a resonant behavior with the valence band. Burstein et al. [Bur80] proposed a microscopic model for the inelastic light scattering processes of single-particle and collective intersubband excitations on 2DES for backscattering geometry with no wave-vector transfer involved ($q = 0$). Schönhuber et al. [Sch16a] adapted the model from [Bur80], and transferred it to intrasubband excitations, including a wave-vector transfer into the 2DES, shown in Fig. 2.16.

Let us start by describing the two-step SOP from Fig. 2.16 (a): In the first step, an electron is excited from the valence band into the conduction band above the Fermi energy with a change in $k_\parallel$, leaving a hole behind in the valence band. In the second step, an electron from the Fermi sea recombines with the hole, which in total either

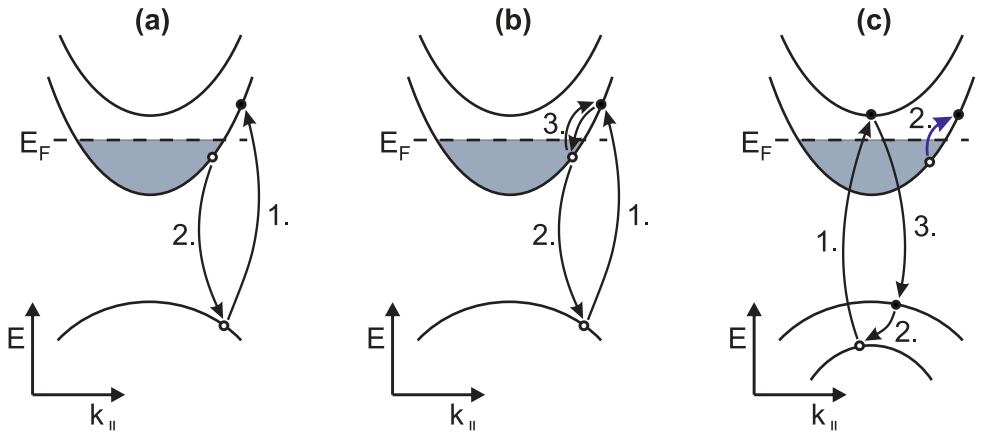

Figure 2.16 | Microscopic models for resonant inelastic light scattering processes in a 2DES. The black dots represent electrons, the open circles are indicating holes. (a) Two-step second-order scattering process, describing spinflip- and nonspinflip single-particle excitations in the conduction band. (b) Three-step second-order scattering process, describing the formation of collective CDE and SDE. (c) Three-step third-order scattering process, dominant for collective plasmons. Taken from [Sch16a] and slightly adapted.

results in a spinflip or a non-spinflip SPE, that has been created in the conduction band. In a third step, shown in Fig. 2.16 (b), an additional SPE is created due to Coulomb interaction. This happens due to screening effects of the SPE towards other SPEs present in the system, allowing the formation of collective CDE and SDE, which are coupled via direct- and exchange Coulomb interaction [Bur80, Sch06]. Collective modes are also found for excitations well above the fundamental band gap. The three-step TOP mechanism sketched in Fig. 2.16 (c) was proposed by Danan et al. [Dan89], and theoretically described by Govorov et al. [Gov97]. In the first step, an electron-hole pair (exciton) is created in a higher conduction- and valence band. Under direct and exchange Coulomb interaction with the Fermi sea, the exciton is scattered, and creates a collective excitation in the conduction band (blue arrow). Due to energy and momentum conservation, an electron from a higher valence band relaxes into the deeper situated valence band, simultaneously. In the last step, the exciton recombines. As can be seen from Fig. 2.16 (a), SPEs are resonant with the Fermi energy whereas the collective plasmon excitations from Fig. 2.16 (c) are related to excitons at the zone center and thus resonant to noticeably different incident energies. The resonance condition was furthermore found to be delicately dependent on the involved specific wave-vector transfer of the excitation [Jus00].

Scattering cross section

As mentioned above, SDEs only occur in *resonant* conditions, which can be derived from the differential cross section. This was described by Hamilton and McWhorter [Ham69]

$$\frac{d^2\sigma}{d\Omega d\omega} \propto \frac{\omega_S}{\omega_I} S(\omega). \tag{2.24}$$

The differential cross section is proportional to the structure factor $S(\omega)$, which reads

$$S(\omega) = \left\langle \sum_S \left| \langle S \left| V_{\text{eff}} \right| I \rangle \right|^2 \ \delta(E_I - E_S - \hbar\omega) \right\rangle. \tag{2.25}$$

The operator V_{eff} describes the transition of the system from the initial many-particle state $|I\rangle$ to the final state $|S\rangle$ with the corresponding energies E_I and E_S. This effective light scattering operator V_{eff} for many-particle systems can be expanded, using the second-quantization technique, which then reads [Gov97]

$$V_{\text{eff}} = \sum_{\alpha,\beta} \gamma_{\alpha\beta} \hat{c}_\beta^\dagger \hat{c}_\alpha. \tag{2.26}$$

Here, a single electron state is characterized by a set of Bloch waves, written as α and β. The creation and annihilation operator of the mode α are represented by $\hat{c}_\alpha^\dagger$ and $\hat{c}_\alpha$, respectively. By neglecting the excitonic electron-hole interaction, the scattering amplitudes $\gamma_{\alpha\beta}$ can be approximated as [Blu70, Gov97]

$$\begin{aligned} \gamma_{\alpha\beta} \sim \left\langle \alpha \left| e^{i\boldsymbol{qr}} \right| \beta \right\rangle \boldsymbol{e}_I \boldsymbol{e}_S \ &+ \frac{1}{m} \sum_{\beta'} \frac{\langle \alpha \left| \boldsymbol{pA}_S \right| \beta' \rangle \langle \beta' \left| \boldsymbol{pA}_I \right| \beta \rangle}{E_\beta - E_{\beta'} - \hbar\omega_I} \\ &+ \sum_{\nu\nu'} \frac{\langle \beta \left| \boldsymbol{pA}_S \right| \nu' \rangle \langle \nu' \left| V_{e-e} \right| \nu \rangle \langle \nu \left| \boldsymbol{pA}_I \right| \alpha \rangle}{(E_\beta - E_{\nu'} - \hbar\omega_S)(E_\alpha - E_\nu - \hbar\omega_I)}. \end{aligned} \tag{2.27}$$

The scalar product of the incident and scattered photon $\boldsymbol{e}_I$ and $\boldsymbol{e}_S$ in the first term of Eq. (2.27) shows, that this nonresonant term in first-order perturbation theory only contributes to non-spinflip light scattering on plasmons (CDEs). However, spinflip excitations, necessary for SDEs are only allowed under resonant conditions. The second term in Eq. (2.27) describes second order resonant processes, which we have seen in Fig. 2.16 (a). They lead to single-particle excitations, which are of main interest in this work, and will be discussed in more detail in Sec. 2.4.3. Third order resonance processes from Fig. 2.16 (c) are described by the last term of Eq. (2.27). The denominators of the two last terms directly show the resonant character of these processes.

Polarization selection rules

From the scattering cross section, the polarization selection rules can be derived, allowing an experimental separation of SDEs and CDEs. In Eq. (2.27) the polarization vectors $\boldsymbol{e}_{I,S}$ are directly visible in the first term, whereas for the other terms they are included in the vector potentials $\boldsymbol{A}$. According to Hamilton and McWhorter [Ham69], one can select CDEs in parallel polarization ($\boldsymbol{e}_I \parallel \boldsymbol{e}_S$) and SDE in depolarized ($\boldsymbol{e}_I \perp \boldsymbol{e}_S$) measurement geometry. This follows from the Bloch parts of the corresponding wave functions, and is independent of the dimensionality of the electron system. As a direct consequence of the confinement in 2DES, also products of the overlap integrals of the corresponding envelope wave functions have to be taken into account, leading to additional parity selection rules. Due to the two-photon character of Raman scattering, only excitations with even parity are allowed. This only holds for symmetrical quantum well potentials, for asymmetrical structures they are softened. A detailed discussion of the selection rules can be found in Ref. [Sch06].

2.4.3 Intrasubband SDEs in [001]-grown quantum wells

In this section, it will be demonstrated how spinflip intrasubband SDEs can be utilized to investigate the spin-orbit coupling effects in a [001]-grown GaAs-AlGaAs quantum well in the regime of the persistent spin helix. In general, single-particle intrasubband SDEs consist of spin-flip as well as non-spin-flip processes, as previously discussed based on Fig. 2.14. In the following, it will be shown that for [001]-grown 2DES samples, as used in this work, only spin-flip transitions should contribute to the RILS spectra, recorded in depolarized scattering geometry, which was demonstrated by Schönhuber et al. [Sch14].

If one assumes a constant band gap transition energy ($E_\beta - E_{\beta'} = \text{const.}$ in Eq. (2.27)) and uses the band-edge Bloch functions [Sch06], the scattering amplitude A_{fi} can be derived from the second term in Eq. (2.27). It is given by [Ham69, Mal97]

$$A_{fi} = \gamma_{fi}(\boldsymbol{e}_i \times \boldsymbol{e}_s^*) \langle \psi_f | \boldsymbol{\sigma} | \psi_i \rangle , \tag{2.28}$$

where $\psi_{i,f}$ represents the initial and the final spin state of an electron in a SDE scattering process, $\boldsymbol{e}_{i,s}$ the polarization vector of the incident and scattered light wave, and γ_{fi} contains resonance enhancing effects [Ham69]. For a fixed excitation laser energy and negligibly small single-particle transition energies, γ_{fi} can be considered as a constant. By choosing the [001] direction (z-axis) as the spin quantization axis, and considering experiments in exact backscattering geometry ($\theta = 0°$), the cross product

of $\boldsymbol{e}_i$ and $\boldsymbol{e}_s$ only has a z-component. This approximation is reasonable because of the high refractive index of GaAs (≈ 3.6). The spin-dependent part of the electron wave function for in-plane spins is then given by [Mal97]

$$|\psi_{\pm\boldsymbol{k}}\rangle = \frac{1}{\sqrt{2}} e^{-i\phi_k/2} \left[\, |\uparrow\rangle \pm e^{i\phi_k} \, |\downarrow\rangle \, \right]. \tag{2.29}$$

ϕ_k denotes the angle between the spin-orbit field and the [100] crystal direction (x-axis), measured counterclockwise. The spin eigenvectors parallel and antiparallel towards the z-axis are symbolized as $|\uparrow\rangle$ and $|\downarrow\rangle$ respectively. For samples in the persistent spin helix regime, i.e., $\alpha = \beta$ (sample A), we can either have $\phi_k = -45°$ or $135°$ and write down the two possible spin eigenfunctions for in-plane spins [Sch14]

$$|\psi_{\pm\boldsymbol{k}}\rangle = \frac{1}{\sqrt{2}} e^{i\pi/8} \left[|\uparrow\rangle \pm \frac{1}{\sqrt{2}}(1-i) \, |\downarrow\rangle \right]. \tag{2.30}$$

The plus (minus) sign stands for spin orientations parallel (antiparallel) to $[1\bar{1}0]$ crystal direction. It should be noted, that for $\alpha = -\beta$ (sample B), ϕ_k has to be rotated clockwise by 90°, and the signs $\pm$ in Eqs. (2.29) and (2.30) are flipped to $\mp$. This is because of the changed spin and field patterns, visualized in Figs. 2.12 (a) and (c). By plugging Eq. (2.30) into Eq. (2.28), a finite scattering amplitude $A_{+-} = A_{-+} = \gamma_{fi}$ for spin-flip, and zero scattering amplitude $A_{++} = A_{--} = 0$ for non-spin-flip excitations can be verified (explicitly shown in Ref. [Sch16a]). This also means, that the SDE can be interpreted as a triplet excitation, only consisting of the magnetic quantum numbers $m_s = \pm 1$, whereas $m_s = 0$ does not contribute [Bab12]. From this we can conclude that only transitions between different spin subbands have a finite possibility and contribute to the RILS spectra if deviations from the exact backscattering geometry are neglected [Sch14].

Let us now turn to a detailed discussion of spinflip intrasubband SDEs under influence of the spin-orbit field in the regime of the persistent spin helix, exemplary for sample A, i.e., $\alpha = \beta$. For sample B, one has to rotate φ clockwise by 90°, as previously discussed. In Figure 2.17 (a), an exemplary cut through the energy paraboloids from Fig. 2.12 (b) for $\varphi \neq 0°$ is shown. As we have seen in the discussion around Eq. (2.16), the parabolas are spin split by Δk_φ, with a maximum spin splitting at $\varphi = 90°$. The curved arrows represent spin-flip transitions between the spin-split subbands. Here, the energetically highest possible transitions, starting from an occupied electron level in the vicinity of the Fermi energy, are schematically sketched. For a finite wave-vector transfer

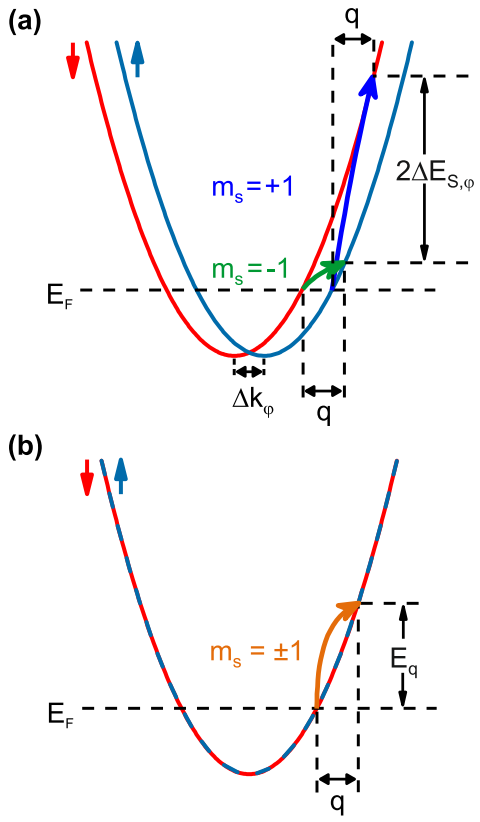

Figure 2.17 | (a) Cut through the energy paraboloids of sample A along $\varphi \neq 0°$ (cf. Fig. 2.12 (b)): Spinflip transitions (curved arrows), corresponding to the high-energy cutoffs of the single-particle continua. (b) Same as (a), for $\varphi = 0°$, where the spin splitting is zero.

$q > \Delta k_\varphi$, it becomes apparent from Fig. 2.17 (a), that two spin-flip transitions with different energies are enabled. According to Eq. (2.19), their high-energy cutoffs are given by $E_q^+ = \Delta E_{S,\varphi} + \frac{\hbar^2}{m^*} k_F\, q$ and $E_q^- = \frac{\hbar^2}{m^*} k_F\, (q - \Delta k_\varphi)$ (blue and green arrows in Fig. 2.17 (a)). $\Delta E_{S,\varphi}$ represents the maximum spin splitting for an in-plane direction φ at the Fermi energy and is given by [Gel20]

$$\Delta E_{S,\varphi} = \frac{\hbar^2}{m^*} k_F \Delta k_\varphi = 2(\alpha + \beta) k_F |\sin\varphi|. \tag{2.31}$$

For the situation $\alpha = -\beta$ Eq. (2.31) is then altered to

$$\Delta E_{S,\varphi} = 2(|\alpha| + \beta) k_F |\cos\varphi|. \tag{2.32}$$

As a consequence of Eq. (2.31), the difference between E_q^+ and E_q^- is just twice the spin splitting at the Fermi level for an arbitrary in-plane direction φ, $E_q^+ - E_q^- = 2\Delta E_{S,\varphi}$. This manifests as a double-peak feature in the measured intrasubband SDE spectra, with the energetic difference of the two emerging peaks of $2\Delta E_{S,\varphi}$.

For a wave-vector transfer along $\varphi = 0°$ (see Fig. 2.17 (b)), where no effective spin-orbit field is present, the spin subbands are degenerate, leading to a vanishing energetic

difference of the possible spin-flip transitions, inducing a single-peak feature in the measured intrasubband SDE spectra. The high-energetic cutoff of the corresponding single-particle continuum is given by $E_q = \frac{\hbar^2}{m^*} k_F q$ (see Eq. (2.19)), and is indicated by the orange arrow. In our experiments, a mapping of the intrinsic SO field was realized, by varying the direction of the transferred wave vector in arbitrary crystal directions φ. The spin splitting was extracted by measuring the energetic difference of the two contributing peaks for $\varphi \neq 0$. This procedure was supported by a numerical lineshape analysis (see Sec. 3.2), where an accurate extraction of $\Delta E_{S,\varphi}$ and other important material parameters was possible.

2.5 Two-dimensional electronic systems in external magnetic fields

In this work we are interested in the detailed study of the intrinsic spin-orbit field of persistent spin helix samples. For this purpose, external magnetic fields are utilized in two different configurations. On the one hand, in-plane external fields are applied to superimpose with the intrinsic spin-orbit field. From this approach we can deduce the direction and strength of the intrinsic SO field, as well as the effective electron g factor. On the other hand, external magnetic fields perpendicular to the 2DES plane (parallel to the confinement axis of the quantum well) are applied, enabling the transition from a well-defined system with lifted spin degeneracy into a Landau-quantized system. This allows us to deduce the charge-carrier density and the effective electron mass of the investigated 2DES.

2.5.1 Superposition of the intrinsic spin-orbit field with external in-plane magnetic fields

When applying an in-plane external magnetic field $\boldsymbol{B}_{\text{ext}}$, a superposition with the intrinsic spin-orbit field $\boldsymbol{B}_{\text{SO}}$ (see Fig. 2.12 (a)) occurs, influencing the spin splitting $\Delta E_{S,\varphi_x}$ shown in Fig. 2.12 (b). Note that for simplicity we will use the angle φ_x in the following, which is measured relative to the [100] (x-axis) direction. In the experimental part of this work, φ is measured relative to the $[\bar{1}10]$ direction. We will now deduce an expression for the electron spin splitting $\Delta E_{S,B}(\varphi_x)$ under the influence of an external in-plane magnetic field, which is always perpendicular to the transferred wave vector, i.e., $\boldsymbol{B}_{\text{ext}} \perp \boldsymbol{q}$. This is a consequence of the experimental backscattering geometry (see

Fig. 3.3 (a)). As we have seen in Sec. 2.3.3, the superposition of the linear Bychkov-Rashba and the Dresselhaus SO field with their strengths α and β is leading to a unidirectional total effective SO field $\boldsymbol{B}_{\mathrm{SO}}$ for $|\alpha| = \beta$. By vectorially adding $\boldsymbol{B}_{\mathrm{ext}}$, this unidirectionality is disturbed, and the resulting total effective field reads

$$\boldsymbol{B}_{\mathrm{tot}} = \boldsymbol{B}_{\mathrm{ext}} + \boldsymbol{B}_{\mathrm{SO}}. \tag{2.33}$$

As in the previous sections, we will here discuss the case $\alpha = \beta$ (sample A). For $\alpha = -\beta$, φ_x has to be rotated clockwise by 90°. For a clearer understanding, $\boldsymbol{B}_{\mathrm{tot}}$ from Eq. (2.33) is sketched in Fig. 2.18 (a) as the blue arrows. The in-situ sample rotation leads to the fact, that $\boldsymbol{q}$ (gray line) is rotating together with $\boldsymbol{B}_{\mathrm{ext}}$ (green arrow) by the angle φ for every measurement step. The intrinsic spin-orbit field $\boldsymbol{B}_{\mathrm{SO}}$ (orange arrows) vectorially adds with $\boldsymbol{B}_{\mathrm{ext}}$ for every configuration of φ, resulting in $\boldsymbol{B}_{\mathrm{tot}}$. In directions, where $\boldsymbol{B}_{\mathrm{SO}}$ is zero ($[\bar{1}10]$ and $[1\bar{1}0]$), the total effective field $\boldsymbol{B}_{\mathrm{tot}}$ is solely given by the external applied field $\boldsymbol{B}_{\mathrm{ext}}$. The resulting Fermi contours for in-plane spins parallel and antiparallel to $\boldsymbol{B}_{\mathrm{tot}}$ are sketched in Fig. 2.18 (b). In comparison to the case without an external magnetic field (cf. Fig 2.12 (b)), a finite spin splitting $\Delta E_{S,B}(\varphi_x)$ occurs for every in-plane direction of $\boldsymbol{k}$.

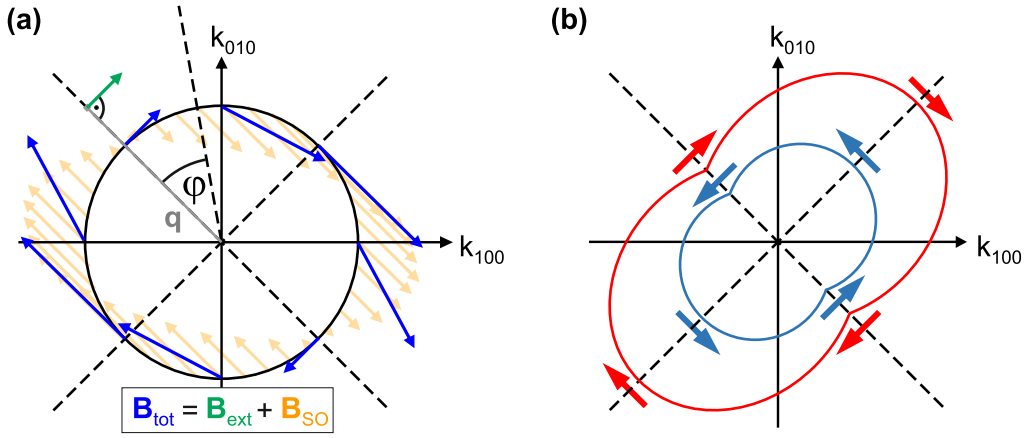

Figure 2.18 | (a) Schematic illustration of the total effective field $\boldsymbol{B}_{\mathrm{tot}}$ for sample A (blue arrows) for in-situ sample rotation, which results from the vectorial sum of $\boldsymbol{B}_{\mathrm{SO}}$ (orange arrows) and $\boldsymbol{B}_{\mathrm{ext}}$ (green arrow). Note, that $\boldsymbol{B}_{\mathrm{ext}}$ is always perpendicular to $\boldsymbol{q}$. (b) Fermi contour for spins parallel and antiparallel to $\boldsymbol{B}_{\mathrm{tot}}$. For every in-plane direction of $\boldsymbol{k}$, a spin splitting for in-plane spins occurs.

In the following we will express $\boldsymbol{B}_{\mathrm{ext}}$ and $\boldsymbol{B}_{\mathrm{SO}}$ in polar coordinates. The external magnetic field reads

$$\boldsymbol{B}_{\mathrm{ext}} = B_0 \left(\boldsymbol{e}_x \sin\varphi_x - \boldsymbol{e}_y \cos\varphi_x \right), \tag{2.34}$$

with B_0 being the external magnetic field strength. For electrons at the Fermi surface, $\boldsymbol{B}_{\mathrm{SO}}$ reads

$$\boldsymbol{B}_{\mathrm{SO}} = \frac{2\alpha k_F}{g\mu_B}\alpha k_F \left[(\cos\varphi_x + \sin\varphi_x)\boldsymbol{e}_x - (\cos\varphi_x + \sin\varphi_x)\boldsymbol{e}_y\right]. \tag{2.35}$$

Here, $\alpha = \beta$ is assumed for the sake of simplicity, g is the electron g factor and μ_B the Bohr magneton. The resulting spin splitting is expected to be of Zeeman type and is connected to $\boldsymbol{B}_{\mathrm{tot}}(\varphi_x)$ via

$$\Delta E_{S,B}(\varphi_x) = g\mu_B \left|\boldsymbol{B}_{\mathrm{tot}}(\varphi_x)\right|. \tag{2.36}$$

With this, we obtain the total magnetic field by calculating the squared absolute value $\left|\boldsymbol{B}_{\mathrm{tot}}\right|^2$

$$\begin{aligned}
|\boldsymbol{B}_{tot}|^2 &= |\boldsymbol{B}_{\mathrm{ext}} + \boldsymbol{B}_{\mathrm{SO}}|^2 \\
&= B_0^2 + \frac{8\alpha^2\boldsymbol{k}_F^2}{(g\mu_B)^2}\left(1 + 2\sin(\varphi_x)\cos(\varphi_x)\right) + \frac{4k_F\alpha}{g\mu_B}B_0\left(1 + 2\sin(\varphi_x)\cos(\varphi_x)\right) \\
&= B_0^2 + \left(\frac{8\alpha^2\boldsymbol{k}_F^2}{(g\mu_B)^2} + \frac{4k_F\alpha}{g\mu_B}B_0\right)\left(1 + \sin(2\varphi_x)\right).
\end{aligned} \tag{2.37}$$

By inserting Eq. (2.37) into Eq. (2.36) we obtain the spin splitting for arbitrary directions φ_x with an external magnetic field B_0 applied in-plane

$$\begin{aligned}
\Delta E_{S,B}(\varphi_x) &= g\mu_B|\boldsymbol{B}_{tot}(\varphi_x)| \\
&= \left[g^2\mu_B^2 B_0^2 + \left(8\alpha^2\boldsymbol{k}_F^2 + 4\alpha k_F g\mu_B B_0\right)\left(1 + 2\sin(\varphi_x)\cos(\varphi_x)\right)\right]^{\frac{1}{2}}.
\end{aligned} \tag{2.38}$$

2.5.2 Landau quantization

By applying an external magnetic field perpendicular to the 2DES (see Fig. 3.3 (b)), the spin-degenerate electronic states of the conduction band split into discrete Landau levels, which are energetically separated by the cyclotron energy $\hbar\omega_c$:

$$\begin{aligned}
E_{n,s}^i &= E_z^i + \left(n + \frac{1}{2}\right)\hbar\omega_c \pm s\, g\mu_B B, \\
\text{with} \quad \omega_c &= \frac{eB}{m^*}.
\end{aligned} \tag{2.39}$$

Here, E_z^i is the subband energy, $n = 0, 1, 2, ..$ the Landau quantum number, $s = \pm\frac{1}{2}$ the

spin quantum number, g the effective electron g factor, $\mu_B = \frac{e\hbar}{2m_e}$ the Bohr magneton, and B the external magnetic field component perpendicular to the 2DES plane. The Landau splitting is described by the second term in Eq. (2.39), while the last term takes the Zeeman splitting into account. With increasing B, the Landau levels move up in energy while the degeneracy of the Landau-levels increases, and levels with higher n are depopulated one after the other until all electrons lie in the lowest Landau level (n=0), which is called the magnetic quantum limit. This process is depicted in Fig. 2.19 (a), where the magnetic field dispersion of the Landau levels (thin black solid lines) is sketched. At every depopulation step, E_F (thick black solid and dashed line) "jumps" into the subjacent Landau level.

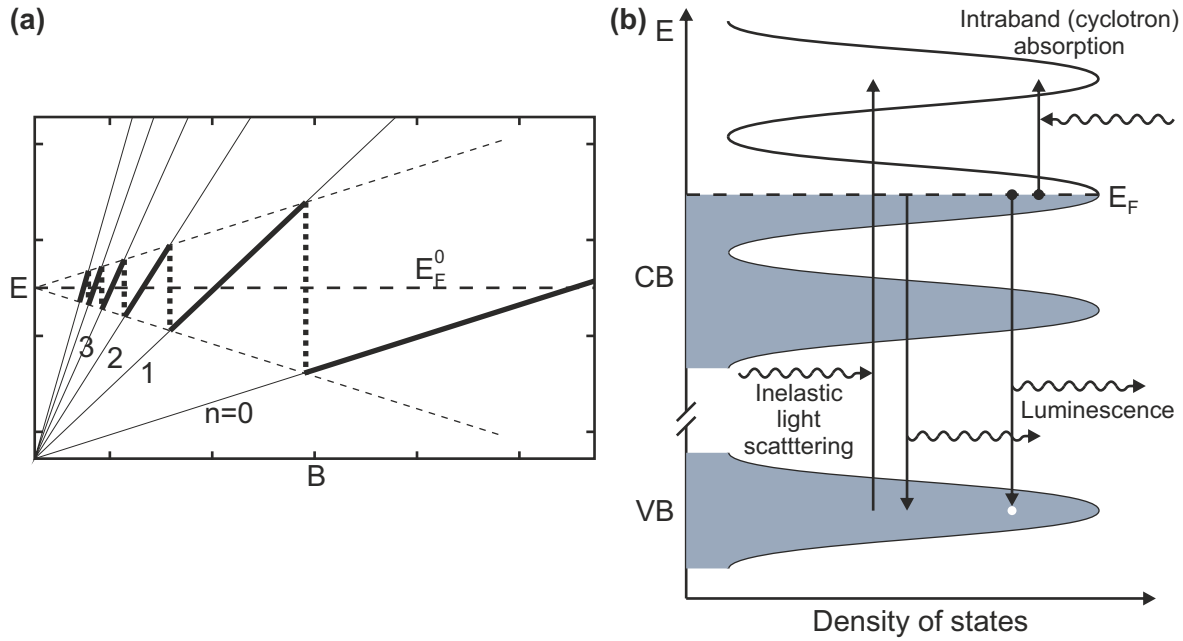

Figure 2.19 | (a) Magnetic field dispersion of a 2DES with δ-function Landau levels (thin black lines) and the progression of the Fermi energy (thick black solid and dashed line). Spin splitting is neglected. Taken from [Dav97] and slightly adapted.
(b) Density of states of a 2DES in the Landau regime. The energetic spacing between the broadened δ-peaks is $\hbar\omega_c$. Possible optical processes are sketched as the vertical black arrows. Spin splitting effects are neglected in this picture. Taken from [Nur93] and slightly adapted.

In a classical picture, electrons are forced to move on circular orbits, when a magnetic field is applied perpendicular to the 2DES plane. Their movement is defined by the cyclotron frequency ω_c. In resonant absorption measurements, when the external radiation matches this angular frequency, ω_c is called cyclotron resonance. Quantum

mechanically, the radius of a cyclotron motion is given by

$$r_n = \sqrt{2n+1}\, l_B, \quad \text{with the magnetic length} \quad l_B = \sqrt{\frac{\hbar}{eB}}. \tag{2.40}$$

The density of states of Landau levels in an idealistic scenario (by neglecting any scattering mechanisms) consists of δ-shaped functions, separated by the energy $\hbar\omega_c$. In a more realistic picture, due to scattering events, these δ functions are broadened, which is sketched in Fig. 2.19 (b). All Landau levels below E_F are occupied (gray shaded area), and cyclotron resonances can be described quantum mechanically as inter-Landau level transitions of electrons between occupied and unoccupied levels[2]. The degeneracy (the allowed number of states in each Landau level) is given by

$$n_B = \frac{eB}{h}. \tag{2.41}$$

The number of occupied Landau levels, often denoted by the filling factor ν, can be written as [Dav97]

$$\nu = \frac{n_{2\mathrm{D}}}{n_B} = \frac{h n_{2\mathrm{D}}}{eB}, \tag{2.42}$$

with the electron density $n_{2\mathrm{D}}$ and the Planck constant h. In luminescence and Raman scattering experiments, also states in the valence band are involved (see Fig. 2.19 (b)), which themselves are subjected to a much more complicated Landau quantization, due to the complex band structure. Inter-Landau level transitions are generally forbidden in inelastic light scattering experiments due to the $\Delta n = 0$ selection rule, stating that only transitions with the same Landau quantum number are allowed. By transferring an in-plane wave vector $\boldsymbol{q}$ into the system, this rule may be broken, and also transitions with $\Delta n \neq 0$ are possible for $q > 1/l_0$ [Wor83, Jus03].

[2]For far-infrared dipole transitions, the selection rule $\Delta n = \pm 1$ holds

Chapter 3

Methods

3.1 Experimental setup

The experimental setup for all measurements presented in this work is schematically depicted in Fig. 3.1. It allows photoluminescence and low-energy Raman measurements at tunable excitation laser wavelengths in the visible range for sample temperatures down to nominally 1.8 Kelvin.

As an excitation source, a continuous-wave Ti:Sapphire laser system (pumped by a diode-pumped Nd:YVO_4 solid state laser) is used, which is tunable in the range from 620 to 1000 nm. The laser light is guided into a laser line tunable filter, which operates with Bragg-filter technology. This device provides a narrow bandwidth of the transmitted laser light (FWHM ~ 0.3 nm) allowing the detection of low-energy Raman spectra. Before entering the cryostat, the polarization and the intensity of the laser light is adjusted by a combination of a $\lambda/2$ waveplate and a polarizer. Depending on the desired measurement geometry (see Sec. 3.1.3), the beam is guided either through the front window, facing towards the spectrometer (backscattering), or, through the side window (grazing incidence). Subsequently, the linearly polarized laser (vertically oriented) beam is focused onto the sample inside the cryostat with a spot size diameter of approximately 100 μm and a power density of about 80 W/cm^2. The backscattered light from the sample is collimated and focused by two achromatic lenses onto the entrance slit of the spectrometer. Measurements are performed either in depolarized geometry (linear polarization of incident laser is perpendicular to scattered light), or, in polarized geometry (linear polarization of incident laser is the same as the scattered light). Since the spectrometer is only sensitive for horizontal polarization, an optional $\lambda/2$ waveplate in combination with a polarizer is used before entering the spectrome-

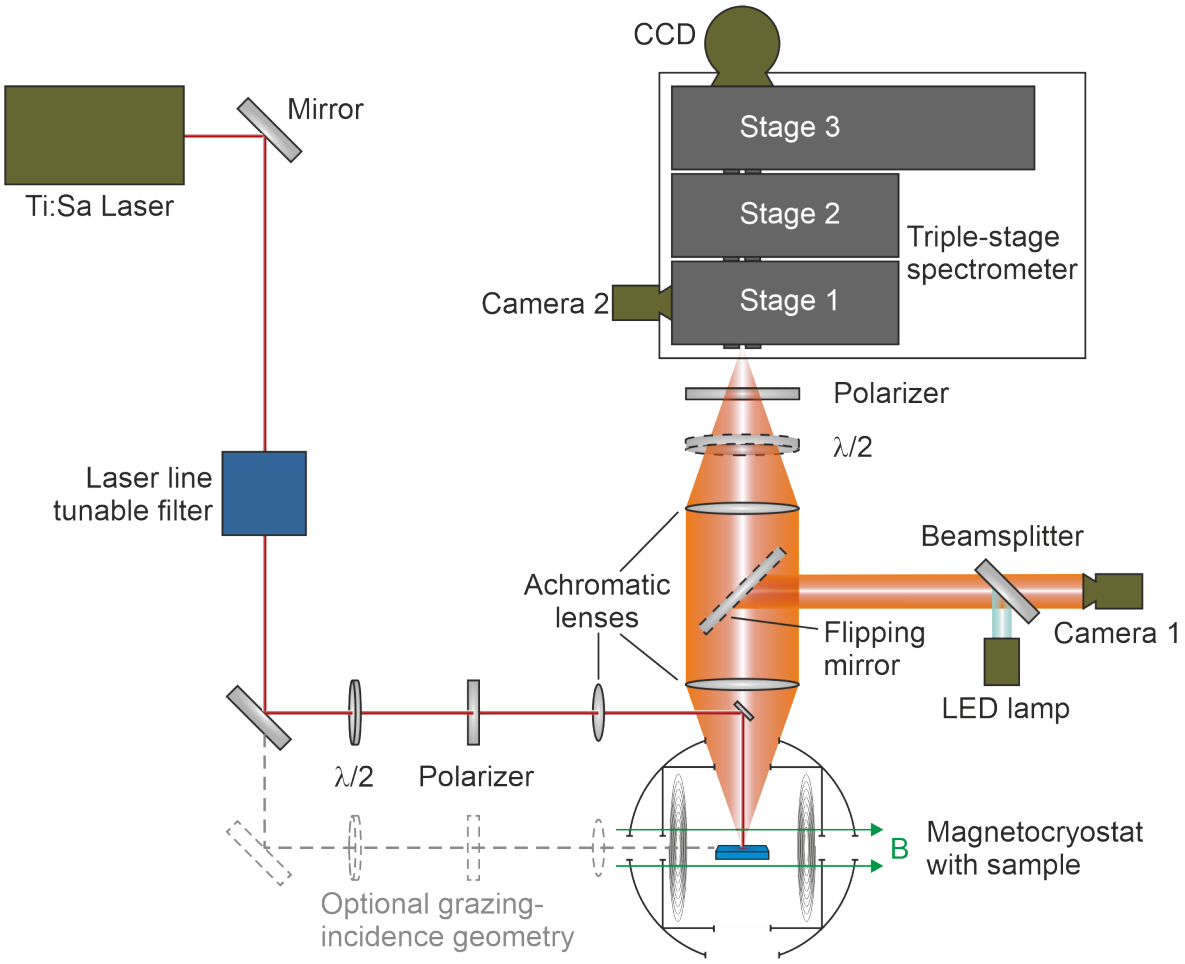

Figure 3.1 | Top view perspective of the optical setup used in this work for Raman and photoluminescence measurements. Here, the configuration for backscattering experiments with external magnetic fields B parallel to the sample surface is shown. The gray dashed beam line, on the lower left side, shows the alternative configuration for grazing-incidence measurement geometry (see Sec. 3.1.3).

ter for depolarized geometry. For polarized geometry, the $\lambda/2$ waveplate is removed. In our low-energy Raman measurements, the triple-stage spectrometer is operated in subtractive mode, where the first two stages act as a tunable bandpass filter for the in-coupled signal, which is crucial for suppressing the elastically backscattered laser light. The diffraction gratings used in the first two stages have 900 lines/mm. The spectral dispersion is carried out by the third stage, using a diffraction grating with 1500 lines/mm. The signal is recorded with a liquid-nitrogen-cooled charge-coupled device (CCD) and evaluated on a computer. A detailed description of the triple-stage spectrometer can be found in previous works from our group [Hir12, Sch16a]. The spectral resolution of this setup is about 34 μeV.

The sample is placed on a rotary stage, which requires a fixed laser position in the rotation center on the sample surface. This is important because of inhomogeneities of the investigated samples (changes of the QW width or doping concentration in lateral direction). In order to find this relative position of the laser spot, a flipping mirror is placed into the collimated lightpath between sample and spectrometer to guide an image of the sample to camera 1 (on the right hand side in Fig. 3.1). A white LED is used for illumination of the sample while adjusting the sample and the laser spot, which is coupled in by a beamsplitter. Once the rotation center is found, the backscattered light of the sample has to be adjusted into the spectrometer. Therefore, an automated flipping mirror inside stage 1 is used to guide the incoming light to camera 2, which can be monitored on an external screen to maximize the in-coupled light intensity. After the backscattered beam path is adjusted, the mirror inside stage 1 is flipped, and the signal is processed by the spectrometer.

3.1.1 Magnetocryostat

The ICEoxford magnetocryostat (^{4}ICE9T$^{\mathrm{Bath}}$) was installed in the course of this work. The main advantage of this system is the comparably large diameter of the sample space (33 mm), which was required for placing the sample on a rotary stage inside the sample space (see Sec. 3.1.2). The system provides a variable temperature insert (VTI) operating from nominally 1.8 to 300 Kelvin. It is specified to reach a magnetic field of 9 Tesla with lambda coil cooling[1] (7 T without lambda cooling) and have a holding time of 72 hours before liquid nitrogen (LN) and liquid helium (LHe) has to be refilled. However due to multiple quenches during the installation process and other significant deficiencies, the system was sent back to the manufacturer three times in the course of this work. However, under challenging operating conditions, measurements were carried out at temperatures of 1.8 K with magnetic fields up to 6 Tesla.

Figure 3.2 (a) shows a sectional drawing of the magnetocryostat. It consists of a LHe main bath at 4.2 K, a LN jacket at 77 K and a vacuum insulation which is evacuated by a turbo molecular pump. Four windows on each side allow optical access to the sample space from all directions. In the course of this work, the mounting of the cryostat on the optical table was specially designed for a more flexible use in different measurement geometries (see Sec. 3.1.3). The whole system is attached to linear rails, enabling a lateral movement for aligning purposes via a micrometer stage. In addition,

[1] An additional cooling circle in the region above the split coil magnet is used to cool the magnet down to ≈ 2.2 K in order to increase the critical field at which superconductivity collapses.

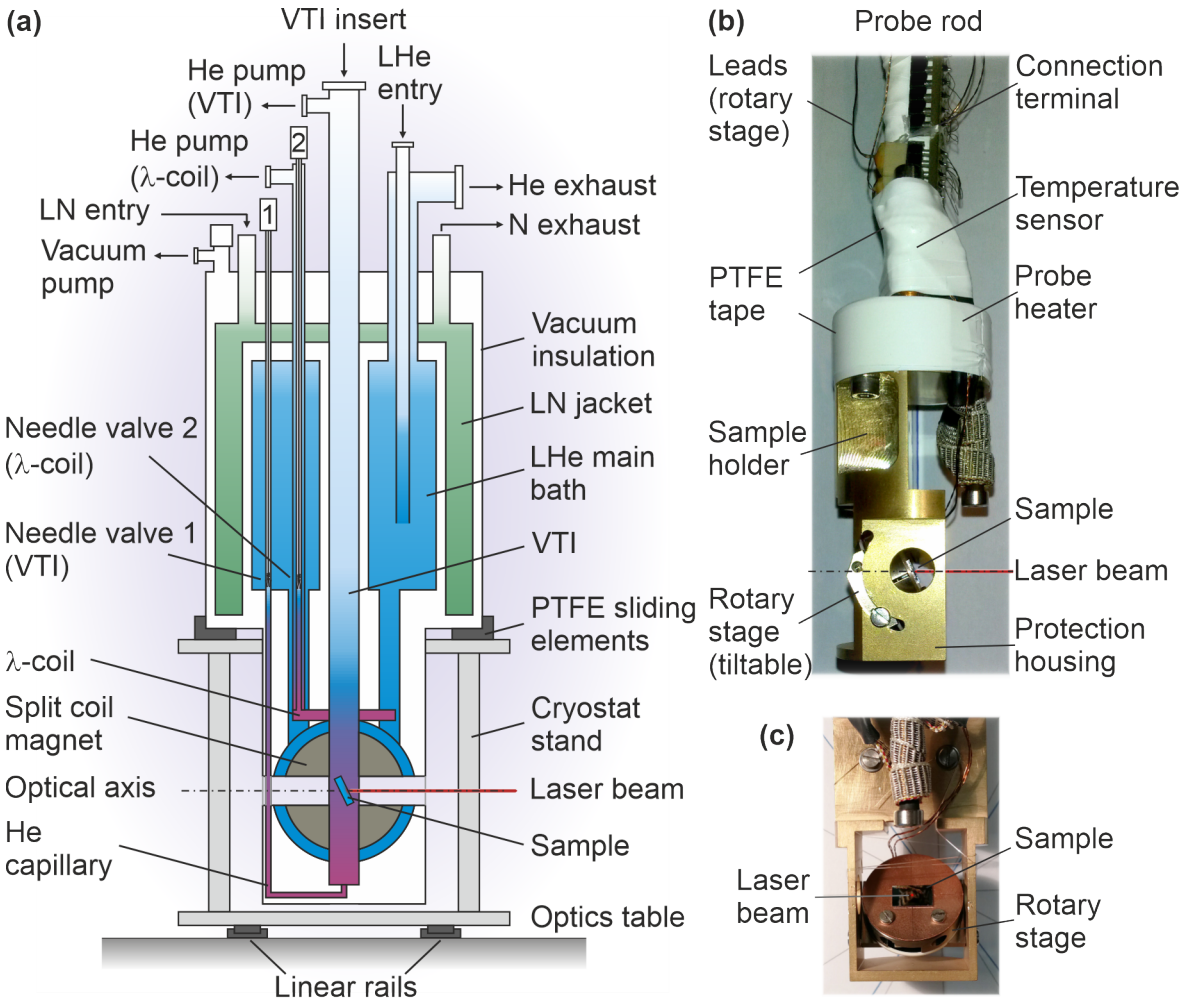

Figure 3.2 | (a) Sectional drawing of the ^{4}ICE9T$^{\mathrm{Bath}}$ magnetocryostat. Here, the configuration for backscattering geometry (see Sec. 3.1.3) is sketched with the magnetic field pointing perpendicular to the drawing layer. (b) Side view image of the cryostat insert (as sketched in (a)) including sample holder, rotary stage and sample. (c) Front view image of the sample holder, from the view of the spectrometer.

the cryostat can be rotated on PTFE sliding elements to adjust the magnetic field orientation parallel or perpendicular to the optical axis.

The colors in Fig. 3.2 (a) stand for the different temperature regions inside the cryostat. Green areas represent 77 K parts at LN temperature, blue represents 4 K parts at LHe temperature and purple indicates areas with temperatures lower than 4 K, which is achieved by evaporation of helium at low pressure. In measurement operation, a rotary-vane vacuum pump is connected to the VTI and needle valve 1 is slightly opened to enable LHe evaporating inside a capillary before entering the VTI to cool down the sample space. The VTI temperature is controlled by a heater and sensor, sitting at the connection between the capillary and the VTI. The cryostat insert with the mounted

sample is top loaded to the VTI and can be adjusted in height and rotation.

3.1.2 Cryostat insert

To perform angle-resolved RILS experiments, the particular measurement geometry required the design of a new cryostat insert, which allows to mount the sample on a tiltable rotary stage. The core part of this insert is the sample holder, which is depicted in Fig. 3.2 (b) and (c). It was CNC machined in our workshop from oxygen-free copper to improve thermal conductivity and reduce diamagnetic effects in external magnetic field measurements. To protect the surface from oxidizing, it was gold-plated.
The sample is mounted on an Attocube ANRv51/RES piezo driven rotary stage with resistive encoder. The angular resolution of the encoder, indicated by the manufacturer is $\approx$ 6 m°, and it is specified to operate in the temperature range between 10 mK and 373 K, at magnetic fields between 0 and 31 Tesla. However, the electrical supply lines between the rotary stage and its control unit had to be designed longer than recommended by the manufacturer, due to the height of the cryostat. This has a significant impact on the resolution and repeatability of the resistive encoder, which is why all angular-resolved measurements were supported by direct imaging with camera 1 (see Fig 3.1), where the twist angle φ of the sample (see Fig. 3.3) is determined by using the sample edges as orientation. The sample including the rotary stage is mounted on the sample holder with an adjustable tilting angle θ (see Fig. 3.3). To prevent damaging of the sample during loading/unloading of the cryostat insert, a protection housing is integrated into the sample holder with lateral bores (visible in Fig. 3.2 (b)) to enable optical access from as many directions as possible, allowing different measurement geometries (see Sec. 3.1.3). To connect the electrical supply lines of the rotary stage and additional wiring for sample gating, a connection terminal was manufactured in collaboration with our technician Christof Ermer from the University of Regensburg. For precise temperature control, a sensor and a heater is attached to the cryostat insert. PTFE tape is used to bundle the wiring and preserve it from being damaged during the loading/unloading process of the probe rod.

3.1.3 Measurement geometry

As already discussed in Sec. 2.4.1, for the investigation of intrasubband spin-density excitations via RILS experiments, it is indispensable to transfer a wave vector $\boldsymbol{q}$ into the 2DES. In this work, two different geometries are used, depending on the desired orientation of the external magnetic field either parallel or perpendicular to the sample

surface. Let us start by discussing the backscattering geometry, allowing experiments with the external magnetic field parallel to the 2DES. This technique was used in most of the experiments. The second geometry is the so-called grazing-incidence geometry, where the angle between incident and the backscattered light is 90°. This geometry has the advantage that the external magnetic field can be applied perpendicular to the 2DES, while the wave-vector transfer $\boldsymbol{q}$ into the 2DES plane is guaranteed.

Backscattering geometry

In backscattering geometry, the sample is tilted towards the incident laser beam, and the scattered light is gathered in the opposite direction as the incident laser. This is sketched in Figs. 3.1 and 3.2 in the context of the overall measurement environment. A detailed schematic of this configuration with all important quantities is shown in Fig. 3.3 (a). During the backscattering process, a part of the incoming laser light momentum is transferred into the 2DES, lying in the sample plane, which will be called $\boldsymbol{q}$ in the following. With simple geometric considerations, it is calculated by the formula [Sch06]

$$q \sim \frac{4\pi}{\lambda_\mathrm{I}} \sin\theta_\mathrm{I,S}, \tag{3.1}$$

with λ_I being the wavelength of the incoming laser light, and $\theta_\mathrm{I,S}$ the tilting angle of the sample-surface normal towards the incident/backscattered light. Due to the relatively small excitation energies compared to the incident laser energy, we assume the incoming laser wavelength being equal to the scattered wavelength ($\lambda_\mathrm{I} \approx \lambda_\mathrm{S}$). In this work, tilting angles of $\theta = 35°$ and 40° were used. As previously described in Sec. 3.1.2, the sample is mounted on a rotary stage, allowing a wave-vector transfer q into arbitrary in-plane crystal directions φ. For this configuration, the external magnetic field B is always perpendicular to $\boldsymbol{q}$, independent of φ.

Grazing-incidence geometry

The second measurement geometry used in this work is the so-called grazing-incidence geometry. As already sketched in Fig. 3.1, the incident laser can be positioned so that the beam enters the cryostat through a side window. This configuration allows the alignment of the external magnetic field perpendicular to the 2DES, while a wave-vector transfer $\boldsymbol{q}$ into the 2DES plane is guaranteed. In Fig. 3.1, this is realized by rotating the cryostat by 90°. Figure 3.3 (b) shows a schematic of all important quantities. Since the incident laser light direction varies from the backscattered beam

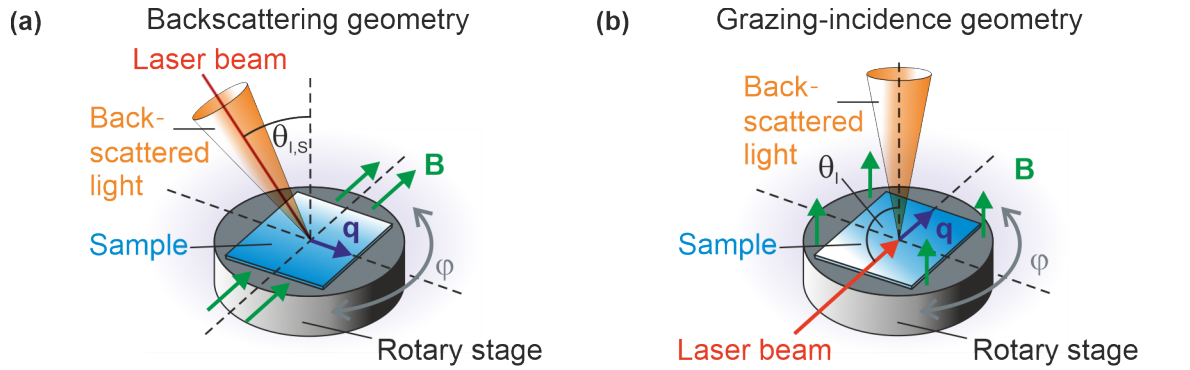

Figure 3.3 | Schematic of the experimental configuration for RILS experiments with a wave-vector transfer into the 2DES plane: (a) In backscattering geometry, the sample is tilted towards the incident/backscattered light by the angle $\theta_{\mathrm{I,S}}$. (b) In grazing-incidence geometry the incident laser beam is tilted by $\theta_{\mathrm{I}} = 90°$ towards the sample-surface normal. Here, the external magnetic field is pointing perpendicular to the 2DES.

direction, the wave-vector transfer is described more generally by [Sch06]

$$q = \frac{2\pi}{\lambda_I} \left[\sin\theta_I + \sin\theta_S\right]. \tag{3.2}$$

Here we have the case $\theta_I = 90°$ and $\theta_S = 0°$, resulting in a wave-vector transfer of $q = 2\pi/\lambda_{\mathrm{I}}$. In direct comparison with the backscattering geometry, one obtains the same result from Eq. (3.2) for a tilting angle of $\theta_{\mathrm{I}} = \theta_{\mathrm{S}} = 30°$, since $\sin 30° = \frac{1}{2}$. We also see, that Eq. (3.1) is a special case of Eq. (3.2).

This geometry also allows measurements with $\boldsymbol{q} \parallel \boldsymbol{B}$, which is achieved by the cryostat position, depicted in Fig. 3.1. One disadvantage of the grazing-incidence geometry is the lower signal yield, since the incident laser spot is stretched due to the grazing incidence, and thus the power density at the measurement spot decreases considerably. This can only be compensated by higher incident laser powers or longer exposure times of the spectrometer camera.

3.2 Computational Lindhard-Mermin line-shape analysis

All low-energy intrasubband spin-density excitation (SDE) spectra in this work were analyzed via a computational line-shape analysis, which is based on the Lindhard-Mermin line shape [Mer70, Fas87]. This procedure is an alternative to the analyzing method used for similar spectra in Ref. [Sch14], where the line-shape analysis was conducted via a phenomenological comparison of experimental spectra. The computational approach allows a very precise study of important material parameters like the effective electron mass m^*, the single-particle scattering time τ_{sp}, the electron temperature T_e, the electron density n, and its dependence on the wave vector $\boldsymbol{q}$, parallel to the 2DES. Ultimately this method can be used to determine the spin splitting $\Delta E_{S,\varphi}$ of double-peak spectra, which are present due to a non-vanishing spin-orbit field.
The source code was implemented in Python$^{\mathrm{TM}}$ together with Christian Frankerl, in the course of his Master's thesis [Fra17] associated to this project. It is based on a Python script, which was written by Dr. Andreas Rabenstein (Chair of Prof. Andreas Schäfer, University of Regensburg), who developed it as a project work within the "Forschungsstudiengang" under supervision of Dr. Cosimo Gorini (Chair of Prof. Klaus Richter, University of Regensburg). The title of this project work is: "Raman scattering on a two dimensional electron gas" [Rab15].
The initial version of the script was intended to reproduce Landau-quantized intrasubband spin-density excitations from a paper by Jusserand et al. [Jus03], in presence of an external magnetic field, perpendicular to the 2DES. In collaboration with Andreas Rabenstein, the script was further developed to be used as a line-shape analysis tool for our acquired intrasubband spin-density excitations under the influence of an intrinsic spin-orbit field in the regime of the persistent spin helix, i.e., $|\alpha| = \beta$.

3.2.1 Basic considerations

In Sec. 2.4.2, a microscopic approach for resonant inelastic light scattering on electrons in 2DES and the corresponding polarization selection rules were derived from the differential scattering cross section, utilizing the structure factor $S(\omega)$. Here, we present an approach, where the dielectric response function is utilized to explicitly simulate the spectral line shape of the low-energy Raman SDE_{00} spectra measured in the course of this thesis. The main difference between these two approaches is that the structure factor also considers the valence band states in a resonant scattering process, whereas

the method presented here only considers conduction band states.

For a non-interacting electron system, the response to an external perturbing field (here the electric field of an incoming light wave) is described by the Lindhard function $\chi_0(\omega, \boldsymbol{q})$ [Lin54] with frequency ω and an arbitrary wave vector $\boldsymbol{q}$. $\chi_0(\omega, \boldsymbol{q})$ has been calculated analytically for a 2DES at zero temperature by Stern [Ste67]. Hamilton and McWhorter [Ham69] have shown theoretically, that Raman scattering from free electron excitations is proportional to the imaginary part of the dielectric response function $\Im\,\chi_0(\omega, \boldsymbol{q})$, which follows from the fluctuation dissipation theorem. In this approach, N. David Mermin found a violation in the conservation of the local electron number which was corrected by using a relaxation time approximation leading to the so-called Lindhard-Mermin response function [Mer70]

$$\chi_{Mermin}(\omega, \boldsymbol{q}) = \frac{\left(1 + \frac{i}{\omega\tau_{\mathrm{sp}}}\right)\left[\chi_0(\omega + \frac{i}{\tau_{\mathrm{sp}}}, \boldsymbol{q})\right]}{1 + \left(\frac{i}{\omega\tau_{\mathrm{sp}}}\right)\left[\frac{\chi_0(\omega + \frac{i}{\tau_{\mathrm{sp}}}, \boldsymbol{q})}{\chi_0(0, \boldsymbol{q})}\right]}, \tag{3.3}$$

with τ_{sp} being the single-particle scattering time. The Lindhard dielectric response function χ_0 [Lin54], adapted for a 2DES is given by

$$\chi_0(\omega, \boldsymbol{q}) = \frac{e^2}{q\Omega} \int d^2k \frac{f_0(E_{\boldsymbol{k}}) - f_0(E_{\boldsymbol{k}+\boldsymbol{q}})}{E_{\boldsymbol{k}+\boldsymbol{q}} - E_{\boldsymbol{k}} - \hbar\omega}. \tag{3.4}$$

Here, Ω denotes the effective Raman cross section, f_0 is the temperature-dependent Fermi-Dirac distribution, and k is the absolute value of the electron wave-vector parallel to the quantum well plane. To obtain the line shape of our experimental spectra, Eq. (3.3) has to be computed numerically in the relevant energetic interval $[\omega_0, \omega_1]$ (corresponding to the Stokes Raman shift). Then its imaginary part is predicted to be proportional to the Raman differential cross section [Fas87], which reads

$$\frac{d^2\sigma}{d\Omega d\omega} \approx \left(1 - e^{-\hbar\omega k_B T}\right)^{-1} \Im\left[\chi_{Mermin}(\omega, \boldsymbol{q})\right]. \tag{3.5}$$

The obtained Lindhard-Mermin-type line shape of intrasubband spinflip excitations for a given $\boldsymbol{q}$ is schematically depicted in Fig. 3.4 as the orange solid line. This line shape corresponds to a transfer of $\boldsymbol{q}$ parallel to a crystal direction with zero spin splitting (cf. Fig. 2.17 (b)). The gray shaded area displays the single-particle continuum for intrasubband spinflip excitations, as shown at the bottom of Fig. 2.15. The high-energy cutoff (vertical dashed arrow) for this case is given by $E_q = \frac{\hbar^2}{m^*} k_F q$ (see Eq. (2.19)).

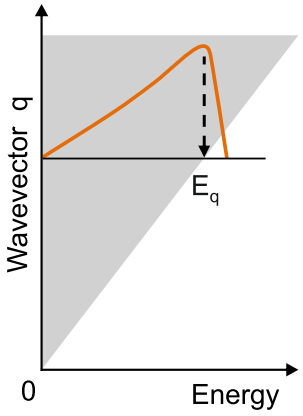

Figure 3.4 | Schematic Lindhard-Mermin-type line shape of intrasubband spinflip excitations (orange solid line) for a wave-vector transfer $\boldsymbol{q}$ in crystal directions with zero spin splitting. The high-energy cutoff is marked as the vertical black dashed arrow. The gray shaded area displays the single-particle continuum for intrasubband spinflip excitations.

3.2.2 Transformations of the Lindhard-Mermin response function

In Eq. (3.3), the Lindhard dielectric response function χ_0 needs to be evaluated at frequencies $\omega + \frac{i}{\tau_{\mathrm{sp}}}$ and 0, i.e.,

$$\chi_0(\omega + \frac{i}{\tau_{\mathrm{sp}}}, \boldsymbol{q}) = \frac{e^2}{q\Omega} \int d^2k \frac{f_0(E_{\boldsymbol{k}}) - f_0(E_{\boldsymbol{k}+\boldsymbol{q}})}{E_{\boldsymbol{k}+\boldsymbol{q}} - E_{\boldsymbol{k}} - \hbar\omega - \hbar\frac{i}{\tau_{\mathrm{sp}}}}, \tag{3.6}$$

and

$$\chi_0(0, \boldsymbol{q}) = \underbrace{\frac{e^2}{q\Omega} \int d^2k \frac{f_0(E_{\boldsymbol{k}}) - f_0(E_{\boldsymbol{k}+\boldsymbol{q}})}{E_{\boldsymbol{k}+\boldsymbol{q}} - E_{\boldsymbol{k}}}}_{X}. \tag{3.7}$$

For a simpler notation, the abbreviation X is introduced in Eq. (3.7). In the following, we will separate the imaginary from the real part in Eq. (3.6), which is done by expanding the fraction in Eq. (3.6) by its complex conjugate

$$\chi_0(\omega + \frac{i}{\tau_{\mathrm{sp}}}, \boldsymbol{q}) = \underbrace{\frac{e^2}{q\Omega} \int d^2k \frac{\left(f_0\left(E_{\boldsymbol{k}}\right) - f_0\left(E_{\boldsymbol{k}+\boldsymbol{q}}\right)\right)\left(E_{\boldsymbol{k}+\boldsymbol{q}} - E_{\boldsymbol{k}} - \hbar\omega\right)}{\left(E_{\boldsymbol{k}+\boldsymbol{q}} - E_{\boldsymbol{k}} - \hbar\omega\right)^2 + \left(\frac{\hbar}{\tau_{\mathrm{sp}}}\right)^2}}_{A}$$

$$+ i \underbrace{\frac{e^2}{q\Omega} \int d^2k \frac{\left(f_0(E_{\boldsymbol{k}}) - f_0(E_{\boldsymbol{k}+\boldsymbol{q}})\right)\left(\frac{\hbar}{\tau_{\mathrm{sp}}}\right)}{\left(E_{\boldsymbol{k}+\boldsymbol{q}} - E_{\boldsymbol{k}} - \hbar\omega\right)^2 + \left(\frac{\hbar}{\tau_{\mathrm{sp}}}\right)^2}}_{B} \tag{3.8}$$

$$= A + iB.$$

Here, A represents the real ($\Re$) and B the imaginary ($\Im$) part of Eq. (3.6). As we have seen in Eq. (3.5), the simulation of our spectra requires only the imaginary part of the Lindhard-Mermin response function. Hence, we reformulate the expression by using another complex conjugated expansion

$$\begin{aligned}\chi_{\text{Mermin}}(\omega,\boldsymbol{q}) &= \frac{\left(1+\frac{i}{\omega\tau_{\text{sp}}}\right)[A+iB]}{1+\left(\frac{i}{\omega\tau_{\text{sp}}}\right)\left[\frac{A+iB}{X}\right]} \\ &= \frac{A+iB+\frac{i}{\omega\tau_{\text{sp}}}A-\frac{1}{\omega\tau_{\text{sp}}}B}{1-\frac{1}{\omega\tau_{\text{sp}}}\frac{B}{X}+\frac{i}{\omega\tau_{\text{sp}}}\frac{A}{X}} \\ &= \frac{\left(A+iB+\frac{i}{\omega\tau_{\text{sp}}}A-\frac{1}{\omega\tau_{\text{sp}}}B\right)\left(1-\frac{1}{\omega\tau_{\text{sp}}}\frac{B}{X}-\frac{i}{\omega\tau_{\text{sp}}}\frac{A}{X}\right)}{\left(1-\frac{1}{\omega\tau_{\text{sp}}}\frac{B}{X}\right)^2+\left(\frac{1}{\omega\tau_{\text{sp}}}\frac{A}{X}\right)^2},\end{aligned} \tag{3.9}$$

which yields

$$\Im[\chi_{\text{Mermin}}(\omega,\boldsymbol{q})] = \frac{-\frac{1}{\omega\tau_{\text{sp}}X}\left(A^2+B^2\right)+B+\frac{A}{\omega\tau_{\text{sp}}}}{\left(1-\frac{1}{\omega\tau_{\text{sp}}}\frac{B}{X}\right)^2+\left(\frac{1}{\omega\tau_{\text{sp}}}\frac{A}{X}\right)^2}. \tag{3.10}$$

3.2.3 Numerical evaluation of the integrals

To obtain the desired spectra using Eq. (3.5), the expressions A, B (from Eq. (3.8)) and X (from Eq. (3.7)) must be calculated numerically. The integration variable is the wave vector $\boldsymbol{k}$, which we will now discuss in detail. We begin with the simplest case of considering single-particle transitions in the absence of an intrinsic spin-orbit field, where the electron spins are degenerate. Figure 3.5 shows a cut through the energy paraboloid at the Fermi energy (gray circle) in k-space together with all involved wave vectors, that have to be taken into account for the calculations. Due to the radially symmetrical structure, we will consider $\boldsymbol{k}$ in polar coordinates. The fixed transferred wave vector into the 2DES is represented by $\boldsymbol{q}$, φ_x is the angle between $\boldsymbol{q}$ and the [100] direction, and is fixed during the calculation (note that the angle φ, used in Fig. 2.12 and in the experimental part of this work is measured relative to the $[\bar{1}10]$ direction). The angle between $\boldsymbol{q}$ and $\boldsymbol{k}$ is represented by γ, ξ is the angle between $\boldsymbol{k}$ and the [110] direction. The integration over $\boldsymbol{k}$ is performed as follows:

$$\int d^2k = \int_0^\infty k\,dk \int_0^{2\pi} d\xi \approx \int_{k_F-\Delta k_F}^{k_F+\Delta k_F} k\,dk \int_0^{2\pi} d\xi. \tag{3.11}$$

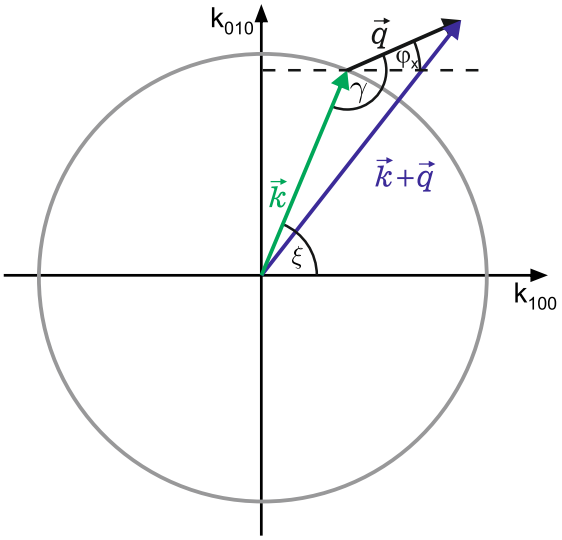

Figure 3.5 | Schematic cut through the energy paraboloid at the Fermi energy (gray circle) in k-space with all wave vectors involved in the calculation of the electronic energy states. The transferred wave vector into the 2DES is denoted by $\boldsymbol{q}$, ξ is the orientation of the electron wave vector $\boldsymbol{k}$.

From Eq. (2.19), we know that the high energy cutoff of a SDE_{00} single-particle transition is given by $E(\boldsymbol{k}+\boldsymbol{q})-E(\boldsymbol{k}) \sim \frac{\hbar^2 \boldsymbol{q}\boldsymbol{k}}{m^*}$. In this approximation $q \ll k \simeq k_F$ is assumed, which leads to the conclusion that only transitions in the vicinity of the Fermi wave vector k_F are contributing to SDE_{00} transitions. A maximum transition energy ΔE is related to a maximum momentum change Δk_F. This allows us to integrate more efficiently, by considering a relevant energy interval of $k_F \pm \Delta k_F$, where Δk_F was varied in the testing process, until the simulation outcome converged to satisfaction. The integration of ξ from 0 to 2π takes all electrons, irrespective of the direction of their crystal momentum into account. For the calculation of the desired spectra, the transition energies that have to be calculated read

$$\Delta E = E_{\boldsymbol{k}+\boldsymbol{q}} - E_{\boldsymbol{k}} = \frac{\hbar^2 \left|\boldsymbol{k}+\boldsymbol{q}\right|^2}{2m^*} - \frac{\left|\boldsymbol{k}\right|^2}{2m^*}. \tag{3.12}$$

Here, the sum of $\boldsymbol{k}$ and $\boldsymbol{q}$ is calculated by simple vector geometry (see Fig. 3.5) and reads

$$\left|\boldsymbol{k}+\boldsymbol{q}\right|^2 = \boldsymbol{k}^2 + \boldsymbol{q}^2 + 2kq\cos(\varphi_x - \xi). \tag{3.13}$$

Putting everything together, A, B and X can be numerically evaluated and plugged into Eq. (3.5) for a set of values of ω in the relevant Stokes energy interval $[\omega_0, \omega_1]$ to generate a SDE_{00} intrasubband Raman spectrum for a system with no spin splitting due to vanishing spin-orbit coupling effects. This is already the case for a wave-vector transfer along $[1\bar{1}0]$ for sample A, and for [110] direction for sample B (see Fig. 2.12), where no effective spin-orbit field is present. Until now, the simulation results are

independent of φ_x, which is the direction of the transferred wave vector $\boldsymbol{q}$.

3.2.4 Including the spin-orbit field of the persistent spin helix

As we have seen in Sec. 2.3.3, two types of the persistent spin helix are of importance for this work, i.e., $\alpha = \pm\beta$ is leading to a maximum spin splitting for $\boldsymbol{k}$ parallel to the [110] (sample A), and the [$\bar{1}$10] (sample B) direction, respectively (see Fig. 2.12 (b) and (d)). For the simulation, a new set of wave vectors to perform the calculations has to be constructed, since the transition energies of the SDE_{00} excitations are changing due to lifting of the spin degeneracy. The transition energies for spin-flip SDE_{00} excitations split into

$$E_{\boldsymbol{k}+\boldsymbol{q}\pm\Delta\boldsymbol{k}} = \frac{\hbar^2|\boldsymbol{k}+\boldsymbol{q}\pm\Delta\boldsymbol{k}|^2}{2m^*}. \tag{3.14}$$

The sign of $\Delta\boldsymbol{k}$ corresponds to the magnetic quantum number $m_s = \pm 1$ of the transitions shown in Fig. 2.17 (a). All involved wave vectors are schematically sketched in Fig. 3.6. Here, the case of sample A is shown, with a shift of the energy parabolas

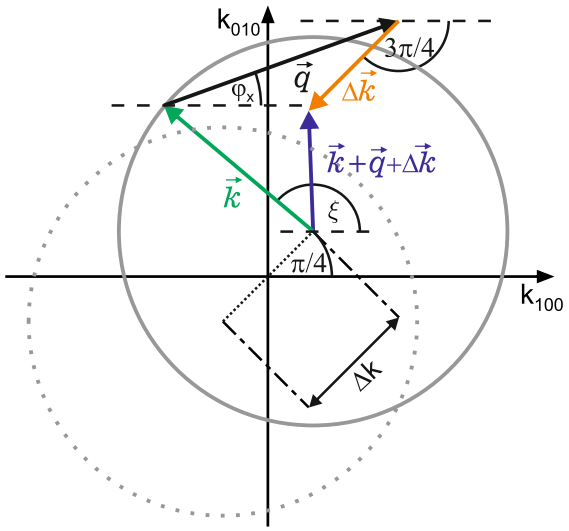

Figure 3.6 | Schematic cut through the spin-split energy paraboloids for a finite effective spin-orbit field. The angular conventions are adopted from Fig. 3.5. For reasons of simplicity, only the lower-energetic transition ($\boldsymbol{k}$ originates in the center of the gray solid circle) is shown. For the higher-energetic transition, $\boldsymbol{k}$ must originate in the center of the gray dotted circle and $\Delta\boldsymbol{k}$ (orange arrow) point in the antiparallel direction ($\frac{7}{4}\pi$).

by $\Delta\boldsymbol{k}$, with maximum spin splitting in [110] direction. The angular conventions still hold, in analogy with Fig. 3.5, with the modification that the centers of the two Fermi circles (gray spheres) are now shifted by $\Delta\boldsymbol{k}/2$ each. In this exemplary case, the lower energetic transition (corresponding to $m_s = -1$ in Fig. 2.17 (a)) is shown, where an electron is raised from a spin state higher in energy to the lower one. The wave vectors necessary for the higher-energetic $m_s = +1$ transition are not shown in Fig. 3.6, but in this case, $\boldsymbol{k}$ has to originate in the center of the dotted gray sphere, and $\Delta\boldsymbol{k}$

(orange arrow) is pointing into the antiparallel direction ($\frac{7}{4}\pi$). For the calculation, the necessary vector components are given by

$$|\boldsymbol{k}+\boldsymbol{q}\pm\Delta\boldsymbol{k}|^2 = \tag{3.15}$$
$$\boldsymbol{k}^2+\boldsymbol{q}^2+\Delta\boldsymbol{k}^2+2kq\cos(\varphi_x-\xi)\pm 2k\Delta k\cos(\xi+\frac{3\pi}{4})\pm 2\boldsymbol{q}\Delta\boldsymbol{k}\cos(\varphi_x+\frac{3\pi}{4}).$$

With this, the transition energies of the possible intrasubband spin-density excitations read

$$\Delta E^{\pm}_{S,\varphi_x} = E_{\boldsymbol{k}+\boldsymbol{q}\pm\Delta\boldsymbol{k}}-E_{\boldsymbol{k}} = \frac{\hbar^2|\boldsymbol{k}+\boldsymbol{q}\pm\Delta\boldsymbol{k}|^2}{2m^*}-\frac{|\boldsymbol{k}|^2}{2m^*} =$$
$$\frac{\hbar^2}{2m^*}\left[\boldsymbol{q}^2+\Delta\boldsymbol{k}^2+2kq\cos(\varphi_x-\xi)\pm 2k\Delta k\cos(\xi+\frac{3\pi}{4})\pm 2q\Delta k\cos(\varphi_x+\frac{3\pi}{4})\right]. \tag{3.16}$$

The integration over $\boldsymbol{k}$ is carried out in analogy to the above shown calculation (see Eq. (3.11)) for systems without spin-orbit coupling, with the only difference that the two components (for each sign of $\Delta\boldsymbol{k}$) have to be calculated independently and be added up in the last step. To clarify this line-shape analysis procedure, Fig. 3.7 shows two experimentally acquired spectra (solid black lines) of sample A, exemplary for a wave-vector transfer along the crystal directions with minimum ($\varphi = 0°$) and maximum spin splitting ($\varphi = 90°$). Note, that φ is measured relative to the $[\bar{1}10]$ direction (cf. Fig. 2.12 (b)) and this convention also holds for all experimental results in Chap. 4. The bottom single-peak spectrum for $\varphi = 0°$, where no effective spin-orbit field is present, can be well reproduced by the simulation (orange open dots). The following material parameters were used for this line-shape analysis: An electron temperature of $T = 12\,\mathrm{K}$, a single-particle scattering time of $\tau_{\mathrm{sp}} = 3\,\mathrm{ps}$ and an electron density of $n = 2.7\times10^{15}\,\mathrm{m}^{-2}$. The parameter dependencies will be discussed in more detail in Sec. 4.6.1. To simulate the upper spectrum for $\varphi = 90°$, where a maximum spin-orbit field is present, the superposition (red crosses in Fig. 3.7) of the two necessary components I_q^+ and I_q^- (blue and green open dots in Fig. 3.7) is obtained by optimizing $\Delta\boldsymbol{k}_\varphi$ (see Eqs. (2.16) and (2.31)) to match the experimental spectra. The extracted peak splittings are just twice the spin splitting $\Delta E_{S,\varphi}$ for the associated in-plane directions, as discussed around Fig. 2.17.

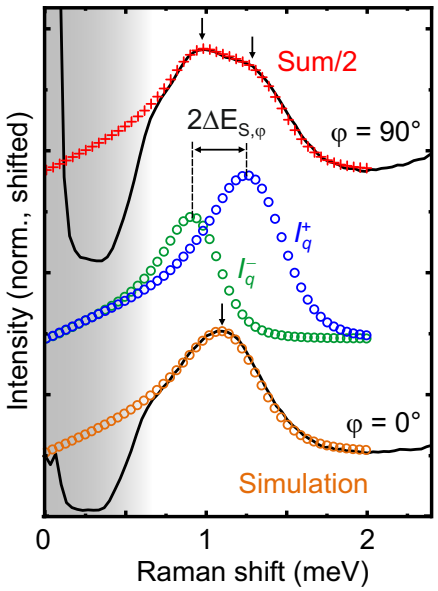

Figure 3.7 | Lindhard-Mermin line-shape analysis of measured spectra from sample A (black solid lines) exemplary for minimum (bottom spectrum) and maximum (top spectrum) spin splitting. The colored scatter plots are the calculated simulations. The gray shaded area is the spectrometer cut off.

3.2.5 Including an external in-plane magnetic field

To complete the line-shape analysis for the performed experiments, the simulation is extended by an external in-plane magnetic field. In Sec. 2.5.1, we deduced the spin splitting $\Delta E_{S,B}(\varphi_x)$ (see Eq. (2.38)) of the system under the influence of an external magnetic field, but only for a certain crystal direction φ_x. In order to simulate the line shape of the obtained spectra, the integrals A, B, and X (from Eqs. (3.7) and (3.8)) need to be calculated, where all possible electronic wave vector orientations ξ are taken into account (cf. Fig. 3.5). In analogy to Eqs. (2.36) and (2.38), we can write for the spin splitting

$$\begin{aligned}\Delta E_{S,B}(\varphi_x,\xi) &= g\mu_B|\boldsymbol{B}_{\mathrm{tot}}(\varphi_x,\xi)| \\ &= \Big[g^2\mu_B^2B_0^2 + 8\alpha^2\boldsymbol{k}^2(1+\sin(2\xi)) + 4\alpha\boldsymbol{k}g\mu_BB_0 \\ &\quad\cdot(\sin(\varphi_x+\xi)+\cos(\varphi_x-\xi))\Big]^{\frac{1}{2}}.\end{aligned} \tag{3.17}$$

This expression includes the total spin splitting caused by the intrinsic spin-orbit coupling together with the external in-plane magnetic field ($\boldsymbol{B}_{\mathrm{ext}} \perp \boldsymbol{q}$). The energies of the two involved Zeeman-splitted spin states read

$$E_{\boldsymbol{k}}^{\pm} = \frac{\hbar^2\boldsymbol{k}^2}{2m^*} \pm \frac{1}{2}\Delta E_{S,B}(\varphi_x,\xi). \tag{3.18}$$

With this, we can construct the energies $E^{\pm}_{\boldsymbol{k}}$ and $E^{\pm}_{\boldsymbol{k}+\boldsymbol{q}}$, which have to be inserted into the well-known integrals A, B and X

$$\begin{aligned} E^{\pm}_{\boldsymbol{k}} = \frac{\hbar^2\boldsymbol{k}^2}{2m^*} \pm \frac{1}{2}\Bigg[& g^2\mu_B^2 B_0^2 + 8\alpha^2\boldsymbol{k}^2(1+2\sin(\xi)\cos(\xi)) \\ & + 4\alpha\boldsymbol{k}g\mu_B B_0\left(\sin(\varphi_x+\xi)+\cos(\varphi_x-\xi)\right)\Bigg]^{\frac{1}{2}}, \end{aligned} \tag{3.19}$$

$$\begin{aligned} E^{\pm}_{\boldsymbol{k}+\boldsymbol{q}} = & \frac{\hbar^2}{2m^*}(\boldsymbol{k}^2+\boldsymbol{q}^2+2kq\cos(\varphi_x-\xi)) \\ & \pm \frac{1}{2}\Bigg[g^2\mu_B^2 B_0^2 + 8\alpha^2(\boldsymbol{k}^2+\boldsymbol{q}^2+2kq\cos(\varphi_x-\xi))(1+2\sin(\xi)\cos(\xi)) \\ & + 4\alpha\sqrt{\boldsymbol{k}^2+\boldsymbol{q}^2+2kq\cos(\varphi_x-\xi)}g\mu_B B_0 \\ & \cdot\left(\sin(\varphi_x+\xi)+\cos(\varphi_x-\xi)\right)\Bigg]^{\frac{1}{2}}. \end{aligned} \tag{3.20}$$

To finally obtain the line shape of the relevant SDE_{00} spectra, the two possible spin-flip transitions $E^{+}_{\boldsymbol{k}+\boldsymbol{q}} - E^{-}_{\boldsymbol{k}}$ and $E^{-}_{\boldsymbol{k}+\boldsymbol{q}} - E^{+}_{\boldsymbol{k}}$ have to be simulated independently, and then be added up.

Chapter 4

Experimental results

4.1 Introduction

This chapter covers the measurement results obtained in the course of this thesis. The main goal of this work was to utilize spin-density excitations to draw conclusions about the intrinsic spin-orbit field and extract its parameters precisely. The Zeeman-like spin splitting characteristic of these spinflip excitations makes them a powerful tool for the investigation of the large spin splitting anisotropy. By application of an external in-plane magnetic field, the intrinsic spin-orbit field is manipulated and detailed information about important spin-orbit parameters can be accessed. To gain a deeper understanding of the SDE, selected spectroscopic images were analyzed, using the numerical lineshape analysis described in Sec. 3.2.

4.2 Sample characterization

We start with a first characterization of all used samples in this work. RILS measurements on sample A and B were already performed in the course of the thesis of Christoph Schönhuber [Sch16a], where a different measurement setup was used. In his work, another cryostat without external magnetic fields and no sample rotary stage was available. Furthermore, different sample pieces of the wafers were used. Due to inhomogeneities of the wafers, e.g., differences in the doping concentration or deviations in the quantum well width, the resonance conditions for detailed analyses of the spin-density excitations are varying. Since we are performing near-resonant RILS measurements, all recorded spectra are dominated by the photoluminescence of the fundamental interband transition of the samples. The goal was to find a compromise

for ideal measurement conditions for SDE spectra, by choosing suitable laser excitation wavelengths for each sample.

4.2.1 Photoluminescence

Photoluminescence (PL) spectroscopy on Gallium arsenide-based materials is a powerful tool to characterize two-dimensional electron systems. This method allows an experimental determination of the interband transition energy E_G which will be presented in this section. In addition, the temperature of the electron gas can be estimated from the Fermi edge (see Sec. 4.2.3). Gallium arsenide is a direct band gap semiconductor, which enables a strong photoluminescence response after laser excitation energies above the interband transition energy E_G. A schematic of the PL process is sketched in Fig. 4.1. The incoming laser light excites an electron from the valence band into the conduction band above the Fermi energy, where free electronic states are available (green arrow). Due to thermalization processes (orange arrows) predominantly by acoustic phonon emission, the energy of the electron is reduced until it recombines radiatively while conserving its momentum. All samples used in this work possess charge carrier densities above $2.7{\times}10^{15}\,\mathrm{m}^{-2}$, leading to a strong Coulomb-screening effect between electron and holes, suppressing the formation of excitons. If the charge-carrier density falls below $1 \times 10^{15}\,\mathrm{m}^{-2}$, a transition between free electrons and the excitonic regime appears [Kle85, Fol93, Shi95]. In Sec. 4.3.2, we will see, that via an external gate, the charge-carrier density can be tuned and this excitonic transition is observable.

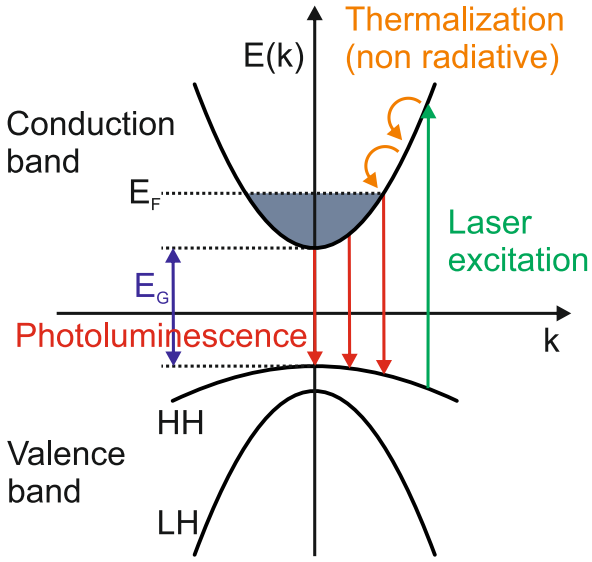

Figure 4.1 | Schematic of the photoluminescence effect for quasi-free electrons in a 2DES. Here the dispersion of the lowest conduction band and the two highest valence bands (HH: heavy hole, LH: light hole) are sketched in momentum space. The Fermi energy lies inside the conduction band due to the high n-doping concentration. Vertical transitions from the Fermi sea into the HH valence band are marked by red arrows.

Considering quasi-free electrons, the radiative recombination processes are approximated by vertical transitions in momentum space, since the k-vector of photons is

negligible. In Fig. 4.1, only transitions from the heavy hole valence band to the lowest conduction band are shown. For this scenario, the band bending of the heavy hole band can be neglected. Due to the conduction band bending, the PL linewidth is, besides homogeneous and inhomogeneous broadening mechanisms, predominantly caused by the position of the Fermi energy. For higher excitation energies, also transitions between the light hole valence band and higher situated conduction bands are enabled.

In Fig. 4.2 the photoluminescence spectra of all investigated samples are plotted. They were recorded in backscattering geometry with no external magnetic field. The laser excitation power for sample A and B was chosen to be 10 mW, and for sample C, 5 mW. The most obvious feature is the energetic difference for the photoluminescence maxi-

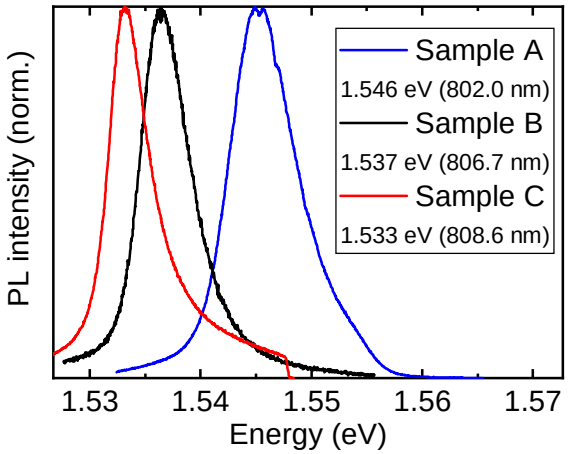

Figure 4.2 | Photoluminescence spectra for all investigated samples. The extracted energetic positions of the PL maxima correspond to the band gap size, given in the inset.

mum of the three samples. According to the manufacturer's specification, the quantum well width of all samples is 12 nm and one would expect a comparable PL transition energy. From the nextnano++ simulations in Sec. 2.2.2, we get a contradictory result of the transition energies, which predicts for sample A the smallest, and for sample C the largest transition energy. The deviations could stem from different band bendings and inhomogeneities of the effective quantum well width throughout the wafers. For different sample pieces of the same wafer, we observed a change in the transition energy of up to ≈ 4 meV. This was already reported by Christoph Schönhuber for sample A and B in Ref. [Sch16a]. To ensure comparability of the measurement data, all experiments were carried out at the same sample pieces and attention was also paid to a constant measuring spot during rotation of the sample. The band bending effect might be increased for asymmetric quantum wells (sample A and B), since the recombination of charge carriers from the quantum well with ionized donors is leading to a flattening of the potential and thus increasing the band gap. Sample C is a symmetrically

grown quantum well and possibly is not affected by this effect, which might explain the smaller size of the band gap.
Another reason for the difference of the PL transition energies, especially for sample A and B, might stem from the band gap renormalization effect (BGR), which causes a reduction of the band gap size for increasing carrier density and decreasing quantum well width [Kle85, Das90, Haa92]. The optically determined electron density of sample B is markedly higher than for sample A (cf. Tab. 2.1), by assuming a comparable quantum well width this could be an explanation for the increased PL energy of sample A.

4.2.2 Resonances of spin-density excitations

RILS experiments require near resonant laser excitation, which is realized by tuning the laser energy in the vicinity of the fundamental interband transition energy of the quantum well. An optimum resonance condition is reached, when the low-energy spin-density excitations can be spectrally well separated from the photoluminescence of the fundamental transition energy.
Later in this work, the intrinsic spin-orbit fields of the [001]-grown, asymmetric quantum well samples A and B are superimposed by external in-plane magnetic fields (see Sec. 4.6). It has turned out, that due to these external fields, additional hot-PL resonances appear in the vicinity of the SDE_{00} spectra. To avoid this disruptive influence, the resonance series were performed under external in-plane magnetic fields for sample A and B.

Sample A

Figure 4.3 shows RILS spectra of sample A for different laser excitation wavelengths from 791.5 nm to 793.5 nm, recorded in cross-polarized backscattering geometry with an incident laser power of 10 mW. For a clearer depiction, all spectra are vertically shifted and the x-axis represents an absolute wavelength scale. Measurements in Fig. 4.3 (a) are performed at zero external magnetic field with a sample tilting angle of $\theta = 35°$, inducing a wave-vector transfer of $q = (9.10 \pm 0.2) \times 10^6\,\mathrm{m}^{-1}$ (the variation stems from the different used laser wavelengths, see Eq. (3.1)). The spectrometer exposure time is 10 s. Fig. 4.3 (b) shows measurements taken for in-plane external magnetic fields $B_{\mathrm{ext}} = 6\,\mathrm{T}$, oriented parallel to the intrinsic spin-orbit field (see Fig. 3.3 (a)) with a tilting angle $\theta = 40°$, leading to a slightly higher wave-vector transfer of $q = (10.20 \pm 0.2) \times 10^6\,\mathrm{m}^{-1}$. The spectrometer exposure time is 240 s.
The diagonal black dashed line marks the Rayleigh backscattered laser light for each

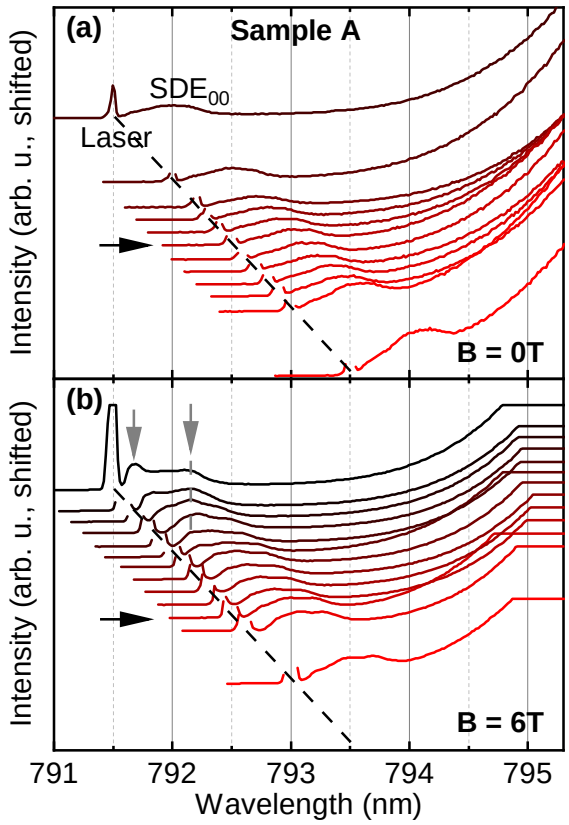

Figure 4.3 | Resonance series for sample A. The laser excitation wavelength was varied from 791.5 nm to 793.5 nm (diagonal black dashed line). The SDE_{00} signal is located at a constant distance to the incidence laser line. On the right hand side of each spectrum, the PL from the fundamental band gap is visible. (a) Measured at zero external magnetic field. (b) Same as (a) but with an in-plane external magnetic field of 6 T. Two emerging hot PL resonances are marked by the gray arrows. The spectrum marked by the black arrow was chosen for following measurements.

recorded spectrum. Its intensity is suppressed, since it lies inside the spectrometer cutoff region, which depends on the individual spectrometer settings and can be adjusted between 0.2 and 0.25 nm above the excitation laser wavelength. The tips of the laser lines are cut for better visibility of the spectra lying on top of each other. The RILS SDE_{00} signal is located at a constant distance to the laser. At the right hand side of each spectrum, the high-energetic tail of the photoluminescence from the fundamental transition energy is visible. Its peak maximum is located at 802.0 nm (cf. Fig. 4.2). By increasing the laser excitation wavelength, the SDE signal shifts towards the spectrally fixed PL. Due to the longer spectrometer exposure time chosen in Fig. 4.3 (b), the PL saturates, and a lower signal to noise ratio is achieved. In Fig. 4.3 (b), besides the SDE signal, we see additional peaks appearing at around 792 nm (marked with gray arrows). The right peak is visible in the upper five spectra at a fixed wavelength of 792.2 nm (gray dashed vertical line), the left peak is located inside the spectrometer cutoff, but is visible in the two upper spectra and vanishes for higher excitation wavelengths. These peaks can be attributed to hot-PL resonances, originating from photoluminescence transitions of higher situated subbands. We can conclude, that the resonance conditions for the SDE_{00} are changing in the presence of an external magnetic field. For detailed peak-splitting analyses of the SDE spectra (see Sec. 4.6), any disturbing

peak would falsify our results. For higher laser wavelengths around 793 nm, the SDE spectra are superimposed by the PL and would also disturb a detailed analysis. The excitation wavelength $\lambda_{\text{laser}} = 792.5\,\text{nm}$ (marked by the horizontal black arrows) has turned out to be the best resonance condition for further measurements.

Sample B

We now turn to the resonance series of sample B. In Fig. 4.4, RILS spectra for laser excitation wavelengths between 789.1 and 798.5 nm with an in-plane external magnetic field of 5 T are shown in cross-polarized backscattering geometry. The tilting angle of the sample is $\theta = 40°$, inducing a wave-vector transfer of $q = (10.18 \pm 0.06) \times 10^6\,\text{m}^{-1}$. The laser excitation power is 10 mW, and the exposure time of the spectrometer is 20 s.

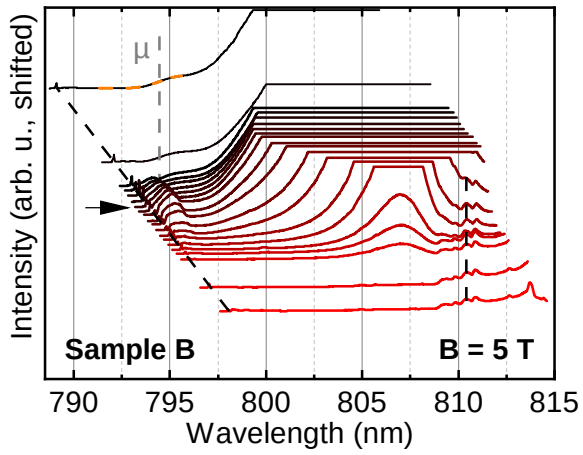

Figure 4.4 | Resonance series for sample B with an in-plane external magnetic field of 5 T. The laser excitation wavelength is varied from 789.1 to 798.5 nm. A clear resonance for $\lambda_{\text{laser}} = 793.8\,\text{nm}$ (black arrow) is visible for both, the SDE and PL resonance. The orange dashed line is a computed Fermi-Dirac fit, μ is the corresponding chemical potential (gray vertical dashed line).

As for sample A, the spectra are shifted vertically for clearer display, and the tips of the backscattered Rayleigh laser signal (along the diagonal black dashed line) are cut for better visibility of the SDE peaks. One notices a strong resonance for $\lambda_{\text{laser}} = 793.8\,\text{nm}$ (black horizontal arrow) for both, the SDE_{00} peak and the PL on the right hand side of the spectra, which saturates in the resonance region. In the upper two spectra for $\lambda_{\text{laser}} = 789.1$ and 792 nm, a shoulder in the high energetic PL flank at constant spectral position $\lambda_\mu = 794.45\,\text{nm}$ is visible (gray dashed vertical line). It can be attributed to the so-called Fermi edge. Laser excited electrons above the Fermi energy (cf. Fig. 4.1) are undergoing non-radiative thermalization processes (mainly scattering on acoustic phonons) until reaching the Fermi energy, where they recombine radiatively. The orange dashed line in the upper spectrum shows a computed Fermi-Dirac fit (see Eq. (4.1)), which was performed for the relevant spectral section. The extracted chemical potential of $\lambda_\mu = 794.45\,\text{nm}$ (1.5606 eV) is marked by the vertical gray dashed line, and a 2DES temperature of 11 K could be extracted. We estimate

the Fermi energy of this sample by determining the distance between $\mu = 1.5606\,\mathrm{eV}$ and the lowest energy of emitted PL photons, which we extract from the center of the low-energetic flank of the PL signal (not shown) $\lambda_c = 1.5377\,\mathrm{eV}$, recorded at the same experimental conditions. From this approach, we get a value of $E_F = 22.9\,\mathrm{meV}$, neglecting the band bending of the heavy hole band. For laser excitation wavelengths above $\lambda_\mu = 794.45\,\mathrm{nm}$, the resonance condition vanishes. This so-called Pauli blocking behavior is expected, because the excitation laser energy shifts below the Fermi energy of the sample, where no more free electron states are available, leading to a quenching of the laser absorption and consequently the PL and the SDE signal. In this regime, at around 810 nm multiple sharp peaks appear (black dashed vertical line) which can be attributed to localized defect states, caused by single excitons localized at sample inhomogeneities. A similar effect was reported by Brunner et al. [Bru94], where narrow PL peaks were detected at the low-energy side of the main luminescence in GaAs/AlGaAs heterojunctions.
In conclusion, a laser excitation wavelength of 793.8 nm was used for all further measurements on this sample. For this resonance condition, the SDE signal is well separated from the PL signal.

Sample C

Figure 4.5 shows the resonance series for the [110]-grown, symmetrical quantum well sample C, measured in backscattering geometry (cross-polarized) with a sample tilting angle of $\theta = 30°$ ($q = (7.91 \pm 0.03) \times 10^6\,\mathrm{m}^{-1}$) at zero external magnetic field. The intrinsic spin-orbit field for this sample points perpendicular to the 2DES plane (see last part of Sec. 2.3.1), so for wave-vector transfers in all in-plane crystal directions no spin splitting is observable and we expect the SDE signal to have a single-peak character. The laser wavelength was varied between 790.17 and 797.46 nm with a power of 5 mW and the spectra were recorded with a spectrometer exposure time of 60 s.
As for sample B, a clear resonance for the SDE and PL peaks is observable for $\lambda_{\mathrm{laser}} = 794.94\,\mathrm{nm}$ (marked by the black arrow). For all spectra, the PL saturates. In the upper spectra, the Fermi edge is visible, and a Fermi-Dirac fit was performed (orange dashed line). We extract a chemical potential at $\lambda_{\mu,\mathrm{LH}} = 795.8\,\mathrm{nm}$ (1.5580 eV) and a temperature of 11 K from this simulation. By increasing the laser wavelength above the resonance, the SDE resonance vanishes and the PL signal narrows, but does not disappear as for sample B. In the bottom two spectra at fixed wavelength $\lambda_{\mu,\mathrm{HH}} = 800.52\,\mathrm{nm}$ (1.5487 eV) a second shoulder in the PL flank appears. We assume this to

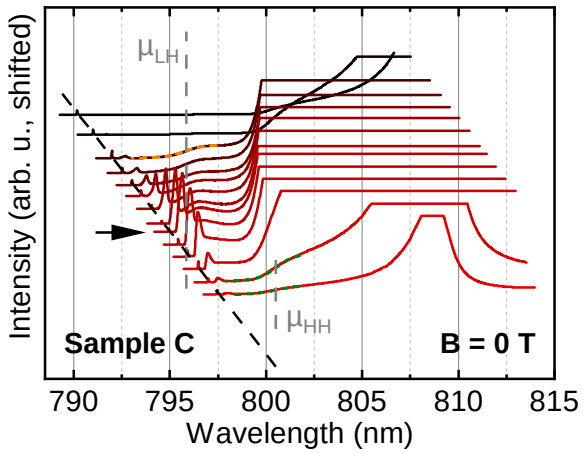

Figure 4.5 | Resonance series for the [110]-grown, symmetric quantum well sample C. The laser excitation wavelength was varied between 790.17 and 797.46 nm. A clear resonance for $\lambda_{\text{laser}} = 794.94\,\text{nm}$ (black arrow) is visible for both the SDE and PL. The Fermi edge appears at two positions (at μ_{LH} and μ_{HH}) we assume a transition between the light hole and the heavy hole resonance (see text).

be the Fermi edge again, which can be explained considering a transition from the light hole to the heavy hole resonance (see Fig. 4.1). This transition is related to a change of the resonance condition, which results in a weakening of the PL intensity. The green dashed lines are fits with the Fermi-Dirac distribution function with an electron temperature of $T = 11\,\text{K}$. By using the extracted chemical potential $\mu_{\text{HH}} = 1.5487\,\text{eV}$ and the center of the low-energetic flank of the PL from Fig. 4.2 (recorded at the same experimental conditions), the Fermi energy is estimated to a value of 17.3 meV, neglecting the band bending of the heavy hole band. The energetic difference between the heavy hole and the light hole band is $\sim 9.19\,\text{meV}$, located at the Fermi wave vector. In the course of this work, RILS spectra with markedly higher laser wavelength around $\lambda_{\mu,\text{HH}} = 800.52\,\text{nm}$ were also recorded (not shown), but no clear defined SDE resonances were found due to the fact, that a long PL tail was superimposing the relevant spectral region.

4.2.3 Excitation-dependent temperature of the 2DES

In the last part of this section, the Fermi edge of sample C is investigated in detail and the 2DES temperature dependence on the incident laser power is estimated for realistic measurement conditions. The nominal sample temperature inside the cryostat is 1.8 K (see Sec. 3.1.1). The 2DES temperature is an important parameter for the Lindhard-Mermin lineshape analysis (see Sec. 3.2) and we will see that the estimated values are in good agreement with the required parameters for the reproduction of our experimental spectra (see Fig. 3.7).

For electrons and holes thermalized to the same temperature, the high-energetic flank of the PL can be approximated by a Fermi-Dirac distribution for direct electron-hole

recombination [Esi87, Ahr93]. It is given by

$$f(E) = \frac{1}{e^{\frac{E-\mu}{k_B T}} + 1}, \tag{4.1}$$

with the chemical potential μ, the Boltzmann constant k_B and the electron temperature T.

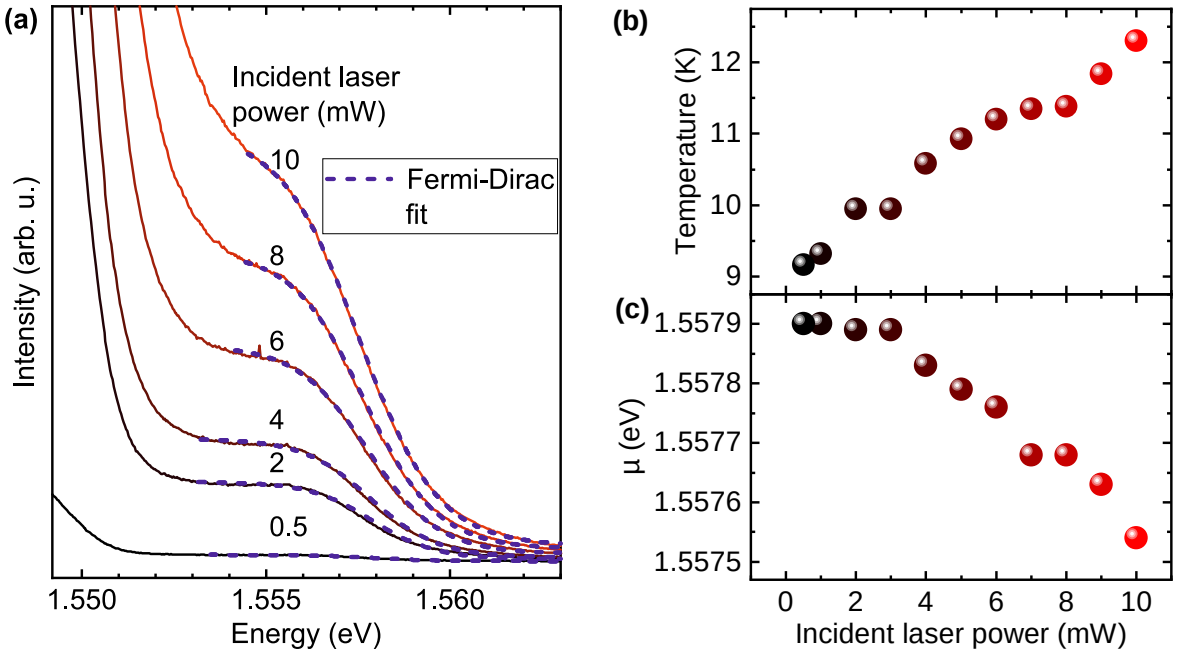

Figure 4.6 | (a) Incident laser power series from 0.5 to 10 mW on sample C. The high-energetic flank of the photoluminescence is shown. For low excitation powers, a clear shoulder is visible, that can be attributed to the Fermi edge. For higher laser powers the lower energetic part of the Fermi edge gets superimposed by the flank of the photoluminescence maximum. The blue dashed lines are computed Fermi-Dirac fits. (b) Extracted 2DES temperature from Fermi-Dirac fits. (c) Extracted chemical potential of the Fermi-Dirac fits.

Figure 4.6 (a) shows a waterfall plot of the high energetic PL flank (solid lines) of sample C for different incident laser excitation powers from 0.5 to 10 mW. Note that the x-axis in this plot is an absolute energy scale. The incident laser energy of 1.5655 eV ($\lambda_{\text{laser}} = 791.97$ nm) has been selected, where the Fermi edge is not superimposed by the SDE signal and the PL is sufficiently far away (see Fig. 4.5). Spectra were recorded in a typical measurement scenario in backscattering geometry with a sample tilting of $\theta = 30°$ in cross-polarized detection geometry with a spectrometer exposure time of 60 s.

For low laser excitation powers (0.5 - 6 mW), a clear shoulder is visible at the high-energy PL flank which smoothly disappears for increasing laser power due to a more

intense PL signal. The blue dashed lines are Fermi-Dirac fits, calculated after Eq. (4.1). The two extracted fitting parameters temperature T and chemical potential μ versus the incident laser power are plotted in Fig. 4.6 (b) and (c). For increasing laser power, the electron temperature rises linearly which can be explained by the heating due to the laser radiation. Simultaneously, the chemical potential μ decreases for higher excitation powers. This effect can be interpreted as a depopulation of electrons from the quantum well. The incident laser photon energy lifts electrons from the quantum well into the barrier material, where they are captured by donor nuclei from the doping layers. This effect is also often referred to as "optical gating" [Cha86, Gri12]. We assume, that this is also the reason, that the optically determined charge carrier densities from our experiments are lower than the specified values from the manufacturer of sample A and B, because they were determined by magneto-transport measurements without laser illumination (see Tab. 2.1).
In conclusion we have seen that for realistic measurement conditions, at a nominal sample temperature of 1.8 K, the 2DES is heated due to laser illumination. All experimentally obtained spectra, supported by the Lindhard-Mermin lineshape analysis (see Secs. 3.2 and 4.6.1), were recorded for a laser power of 10 mW. They are in best agreement with the simulation, when an electron temperature of $T \approx 12\,\mathrm{K}$ is used, which is confirmed by the here presented estimation.

4.3 Electrical gating

The built-in electric field in sample A and B determines the strength of the Bychkov-Rashba SO field, as discussed in Sec. 2.3.2. It has been shown by different groups, that the Bychkov-Rashba SO field can be manipulated via electrical gates, when an external electric field is applied [Nit97, Mil03, Stu09]. In the context of the persistent spin helix state for [001]-grown GaAs/AlGaAs heterostructures, the ratio of Bychkov-Rashba (α) and Dresselhaus (β) SO-field strength is of importance (see Sec. 2.3.3). It was demonstrated in Refs. [Koh12, Ish14], that electrical gating can be used to adjust the ratio of α/β in order to create or even lift the persistent spin helix regime.
In this section, measurements on sample B*, equipped with a semitransparent nickel-chromium top gate are shown (transparency $\sim 50\,\%$), where the 2DES is used as a back-gate contact (see Fig. 2.7). We will start by characterizing the gate with an I-V diagram to find the maximum possible voltage range without destroying the sample. Next, we will discuss in how far the charge-carrier density is affected by the gate voltage. The impact of an external electric field on the spin splitting of the SDE_{00} spectra

will be discussed in the last part of this section.

The measured resistance between the two top-gate contacts and the four back-gate contacts is $\sim$3 kΩ. For all gate-dependent measurements, the two top gate and the four back-gate contacts were each short-circuited to ensure the best possible conductivity. The resistance between back and top gate is $\sim$3 MΩ, indicating no leak currents and therefore a correct function of the gate. The sample was placed inside the cryostat at nominal $T = 1.8$ K and illuminated with an effective laser power of 10 mW. The gate voltage was supplied by a "Keithley Instruments - Model 2400 SourceMeter" device. To prevent damage to the sample by reaching the breakdown voltage, a maximum compliance current of 100 μA was defined. Note, that all given gate voltage values in this section refer to the applied voltage at the top gate.
All spectra presented in this section were recorded in grazing-incidence geometry (see Sec. 3.1.3). This geometry provides a lower signal yield, but an external magnetic field can be applied perpendicular to the sample surface, which will be important later for Landau quantization (see sec. 4.4) and cyclotron resonance experiments (see sec. 4.5).

4.3.1 I-V characteristics

At first, the maximum voltage range for gate measurements was determined in an I-V diagram, shown in Fig. 4.7. For $U > 0.92$ V, an exponential increase of the current occurs, which is a typical diode behavior in forward direction.
The maximum permissible current of 100 μA was reached at $U = 1.125$ V. For negative voltages $U < -5$ V, the current saturates at $\sim -5.4\,\mu$A. This behavior can be attributed to the fact that for negative top gate voltages, the 2DES (operating as back gate), is getting depleted to the point that it can no longer serve as a capacitor plate, and no more significant change of the current can be performed.

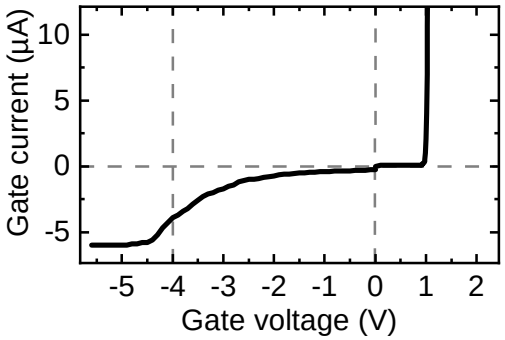

Figure 4.7 | I-V characteristics of sample B*. A typical diode-like behavior with an exponential increase of the current for $U > 0.92\,\mathrm{V}$ is visible. A maximum compliance current of $100\,\mu\mathrm{A}$ was set to prevent gate damage. For negative voltages $U < -5\,\mathrm{V}$, the current saturates at $\sim -5.4\,\mu\mathrm{A}$.

4.3.2 Photoluminescence response

Figure 4.8 (a) shows a 3D waterfall plot of photoluminescence spectra for gate voltages between $-10\,\mathrm{V} < U < 1.125\,\mathrm{V}$. The optimum laser excitation energy for best resonance of the SDE peaks, determined in Sec. 4.2.2 of 1.562 eV (793.8 nm) was used. Because of the high dynamic range of the PL intensity, spectra for negative gate voltages were taken at a spectrometer exposure time of 0.2 s, for positive gate voltages, the exposure time of 1 s was used. To compensate the change in absolute intensity, the y-axis for spectra taken at positive gate voltages is multiplied by the factor 0.2.
In Figures 4.8 (b)-(d) the most important quantities of the PL are extracted: (b) shows the maximum intensity, (c) the energetic position of the maximum and (c) the FWHM of the PL peak. The vertical gray dashed lines are a guide for the eye. In the region around 0 V, no significant change in the PL intensity is visible, while a smooth shift of the PL energy can be observed over a relatively wide gate voltage range. The PL position at $U = 0\,\mathrm{V}$ is consistent with the value, determined for sample B (1.537 eV) in Fig. 4.2, so no significant change in the fundamental transition energy due to the gate is verifiable. For negative gate voltages, the charge-carrier density is decreasing and a band bending effect (also discussed in Sec. 4.2.1) of the quantum well leads to an increase of the fundamental transition energy, indicated by a blueshift of the PL energy. By further ramping down the gate voltage, the FWHM decreases rapidly for $U < -2.6\,\mathrm{V}$ and a PL intensity maximum occurs at $U = -4\,\mathrm{V}$ and saturates for $U < -5\,\mathrm{V}$ at an absolute energy position of 1.5458 eV. This behavior indicates a transition of the PL into an excitonic regime due to the fact that the electron-hole Coulomb interaction is not screened sufficiently. As already discussed in Sec. 4.2.1, this excitonic transition takes place at a charge-carrier density of around $1 \times 10^{15}\,\mathrm{m}^{-2}$ [Kle85, Fol93, Shi95].

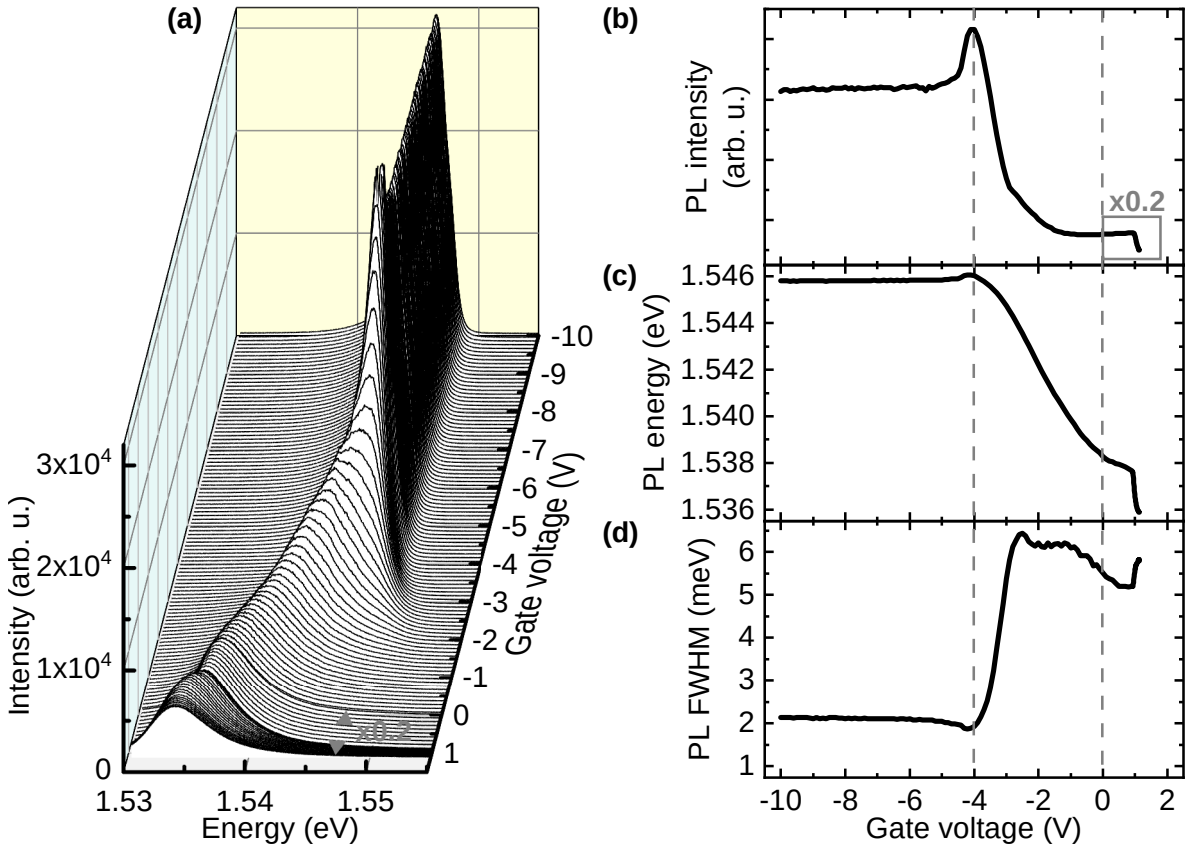

Figure 4.8 | (a) 3D waterfall plot of photoluminescence spectra at different external gate voltages for sample B*. The laser excitation energy is 1.562 eV. (b)-(d) Detailed analysis of PL peak: energetic position, intensity and full width at half maximum (FWHM).

In an illustrative explanation, the depletion of charge carriers reaches a point, where the 2DES is no more filled up completely with electrons, leading to more and more localized electron puddles due to an inhomogeneous potential landscape of the 2DES. Excitons are created by the incident laser radiation, their binding energy depends on the quantum well thickness. In Ref. [Maa84] it was found to be ~ 12 meV for a 12 nm wide GaAs quantum well.

For increasing the charge-carrier density in the 2DES by ramping up the gate voltage, a redshift of the PL energy due to a band bending effect is observable. For $U > 0.92$ V, where an exponentially increasing current flows between top and back gate, we see an abrupt decrease of the PL intensity and energetic position of the signal while the FWHM is increasing. There is no longer a well-defined system, and charge carriers that were previously available for recombination might be torn apart and carried away by the relatively high current flow.
In conclusion, the PL measurements have shown the functionality of the gate and a

change in the charge-carrier density can be performed effectively. In the next step, we are interested in the response of electronic spin-density excitations to external gate voltages.

4.3.3 Electronic Raman response: Tuning of the Bychkov-Rashba parameter

Before we turn to a detailed analysis of the spin splitting of electronic intrasubband spin-density excitations (SDE_{00}) under the influence of an external gate voltage, we will focus on the resonance condition of the SDE_{00} for a fixed laser energy, but different gate voltages. All spectra were recorded with the same measurement parameters as in Fig. 4.8 (a), where the optimum resonance laser excitation energy of 1.562 eV was used (as determined in Sec. 4.2.2). To obtain the low-energy RILS spectra, the cut-off frequency of the triple-Raman spectrometer was moved close to the incident laser energy and the spectrometer exposure time was increased to 60 s. Note that the shown spectra are plotted in the typical x-axis assignment, showing the Stokes Raman shift on the positive side of the x-axis.

Figure 4.9 (a) shows a waterfall plot of RILS measurements on sample B* for different gate voltages between $-4\,\mathrm{V} < U < 1.2\,\mathrm{V}$. The transferred wave vector of $q = 7.92 \times 10^6\,\mathrm{m}^{-1}$ along $\varphi = 90°$ (cf. Fig. 2.12 (d)), is resulting in a SDE_{00} single peak with its maximum at a relative energy position of 1 meV. Figure 4.9 (b) is the same as (a), but for $\varphi = 0°$, resulting in a SDE_{00} double peak (see Sec. 2.17). On the right hand side of all spectra, the high energetic flank of the PL from the fundamental band gap is visible. For gate voltages between $-0.8\,\mathrm{V} < U < 1\,\mathrm{V}$, a shoulder between the SDE_{00} and the PL is observable and can be attributed to the Fermi edge (see Sec. 4.2.3). For sweeping the gate voltage from negative to positive values (increasing the charge-carrier density), the shoulder shifts towards lower Raman energies (the total energy is increased, due to the flipped x-axis), and intensifies the SDE_{00} peak for $U > 0.8\,\mathrm{V}$. Fermi-Dirac fits were performed for all spectra in the gate voltage range between $-0.8\,\mathrm{V} < U < 1\,\mathrm{V}$. The orange dashed line in Fig. 4.9 (a) exemplarily shows the fit for $U = 0\,\mathrm{V}$, the extracted chemical potential for this fit is $\mu = 1.5579\,\mathrm{eV}$. For sample B (equipped with no gate), a value of $\mu = 1.5606\,\mathrm{eV}$ (2.7 meV higher) was found (see Fig. 4.4). In principle, the application of a metallic top gate creates a Schottky barrier, which leads to a bending of the potential curve (cf. Fig. 2.6) due to the creation of a space-charge region. This might explain the slight increase of the chemical potential, indicating a higher charge-carrier density.

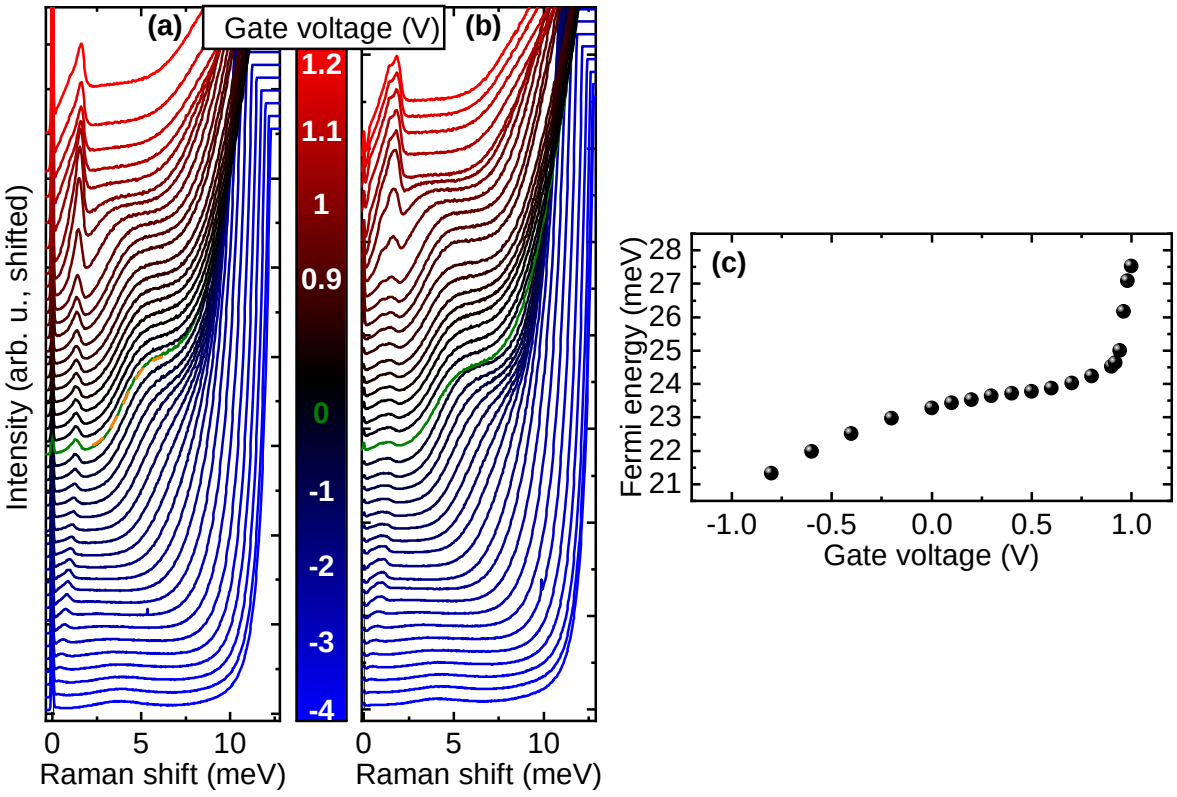

Figure 4.9 | RILS waterfall plots of sample B* for a set of different gate voltages. The SDE_{00} signal is located at around 1 meV. The high-energetic tail of the PL is visible on the right hand side of all spectra. (a) The wave-vector transfer points along $\varphi = 90°$, resulting in single peak spectra. The orange dotted line shows one exemplary Fermi-Dirac fit. (b) Same as (a), but for $\boldsymbol{q}$ pointing along $\varphi = 0°$, resulting in double-peak spectra. (c) Extracted Fermi energy versus gate voltage from Fermi-Dirac fits of (a).

Figure 4.9 (c) shows the extracted Fermi energy for all spectra, where the shoulder is visible. This was done by measuring the distance between μ and the center of the low-energetic PL flank for each spectrum (as previously shown). Negative gate voltages have a stronger effect of a change in the Fermi energy, because of the steeper slope compared to positive voltages. This might be an indication of the square root dependence of the carrier density N_s on the Fermi wave vector k_F from Eq. (2.21). We can conclude here, that the effect of varying the charge-carrier density through the gate is more efficient for negative gate voltages. This holds for gate voltages $< 0.92\,\mathrm{V}$, since above this value the system is no more well-defined due to flowing currents (see Fig. 4.7).

Next we want to focus on the SDE_{00} resonances in detail. Figures 4.10 (a) and (b) are normalized spectra from Fig. 4.9 (a) and (b), showing a zoom in the relevant spectral

region. For $\varphi = 90°$ a narrow peak (single peak) and for $\varphi = 0°$ a broadened (double peak) feature ca be observed (see Sec. 2.4.3). For easier reference, the single peak is labeled as "s", the double peaks are labeled as "d_1" and "d_2".

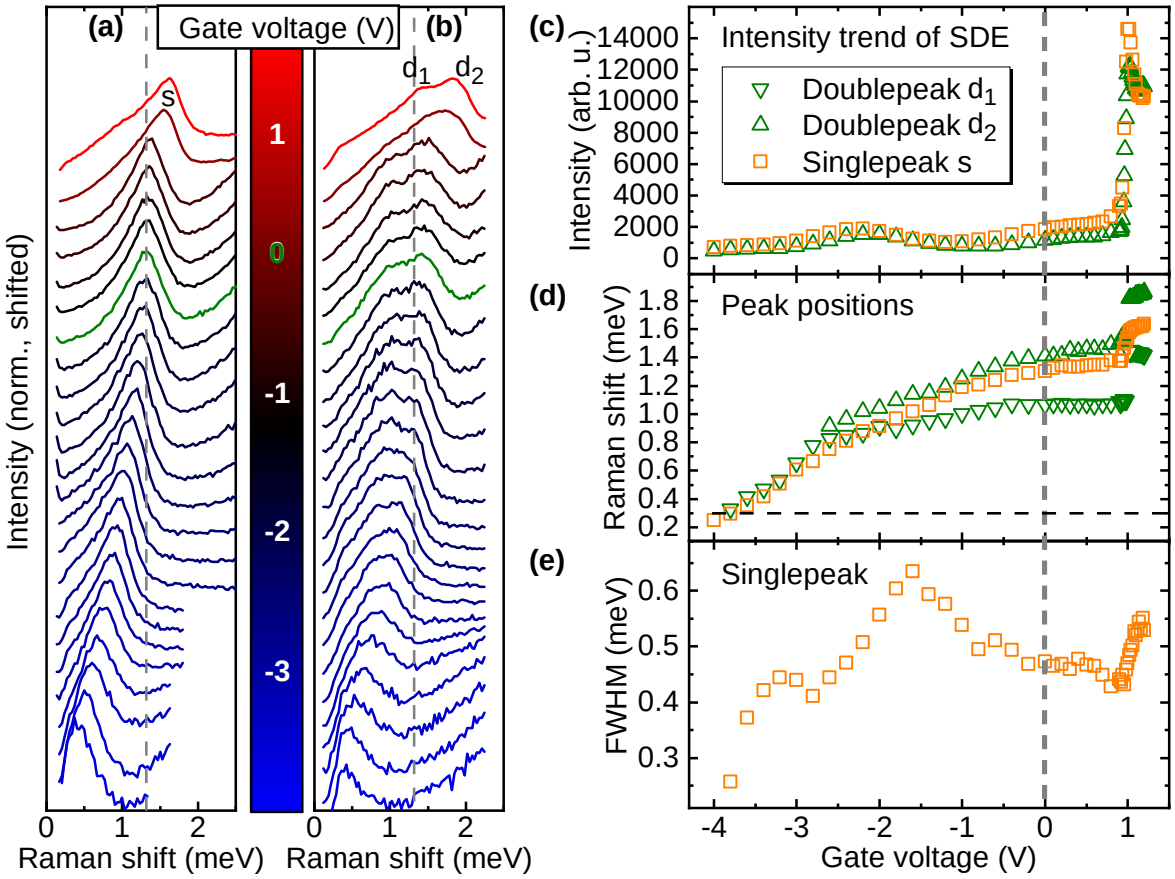

Figure 4.10 | Normalized RILS spectra of sample B* in the low-energetic region of the SDE_{00} resonances for a wave-vector transfer $\boldsymbol{q}$ along the single-peak direction (a): $\varphi = 90°$ and along the double-peak direction (b): $\varphi = 0°$. Important peak parameters extracted from (a) and (b): (c) Maximum intensity, (d) Energetic peak positions, (e) FWHM of single peak "s". The vertical gray dashed lines serve as a guide for the eye.

The most important peak parameters are extracted in Fig. 4.10 (c)-(e). The maximum intensity of the SDE peak is shown in (c), (d) shows the energetic positions of all peak maxima, and (e) shows the FWHM of peak "s". For negative gate voltages, the intensity of all peaks is almost constant with a small hump at $U \sim -2.1\,\mathrm{V}$. This small resonance might originate from a hot PL signal, visible in the bottom spectra of Fig. 4.9 (a) and (b) at around 4 meV. For positive gate voltages, between $0.8\,\mathrm{V} < U < 0.92\,\mathrm{V}$, the strong intensity increase was discussed previously due to a shift of the resonance with the Fermi edge. For $U > 0.92\,\mathrm{V}$ the intensity decreases, which might be due to the onset of current flowing between the top gate and the back gate. Fig. 4.10 (d) shows

the energetic position of peak "s" and all recognizable sub peaks "d_1" and "d_2" (visible for gate voltages $U > -2.6\,\mathrm{V}$). The high-energetic cutoff of all peaks is proportional to the charge-carrier density of the 2DES (see Eqs. (2.19) and (2.21)). For this reason the energetic peak positions are shifted by changing the gate voltage. Again we see a steeper slope for negative gate voltages that might stem from the square root dependence of the charge-carrier density N_s on the Fermi wave vector k_F from Eq. (2.21).

We have seen, that the main effect of tuning the gate voltage results in a change of the charge-carrier density. In the next step we will investigate if there is also an observable effect due to an emerging electric field, affecting the Bychkov-Rashba parameter (α). An electric field caused by a gate voltage perpendicular to the 2DES plane should have an effect on both, the cubic Dresselhaus term (see Eq. (2.8)) which is neglected here, and the Bychkov-Rashba SO-interaction (electric dipole field between the 2DES and the ionized dopant Si-nuclei). However, in the following we will investigate the effect of a gate voltage on the Bychkov-Rashba parameter in a simplified picture. We start by examining the full width at half maximum (FWHM) of the single peak. For a wave-vector transfer along $\varphi = 90°$, the spin splitting of the SDE single peak is described by [Ric96, Ber06]

$$\Delta E_{S,\varphi=90°} = 2(|\alpha| - \beta) \cdot k_F. \tag{4.2}$$

This means, that for equal strengths of $|\alpha|$ and β, the peak width is expected to be minimal (see Sec. 2.3.3). In Fig. 4.10 (e), the FWHM of the single peak is plotted against the applied gate voltage. We observe a prominent maximum at $U = -1.6\,\mathrm{V}$ that might stem from a hot-PL resonance (mentioned above), and two minima at $U = -2.8\,\mathrm{V}$ and $U = 0.8\,\mathrm{V}$, that might be a hint for the condition of $\alpha = -\beta$, initiated by a change in the electric field. However, the significance of this observation is reduced by the low signal to noise ratio, especially for negative gate voltages, where the SDE_{00} peak is near the spectrometer cutoff region.

We will further discuss another approach to detect a change in the Bychkov-Rashba parameter due to external gating. The spin splitting in direction with maximum SO-field directly depends on $|\alpha|$ (see Eq. (4.2)), but in single peak direction this $|\alpha|$-dependency can be neglected. By putting these two premises in relation to each other, we can extract the gate dependent value of $|\alpha|$ from our measurement data. Fig. 4.11 (a) displays the extracted high energetic cutoff $E_{q,\varphi=90°}$ of peak "s" from Fig. 4.10 (a). After

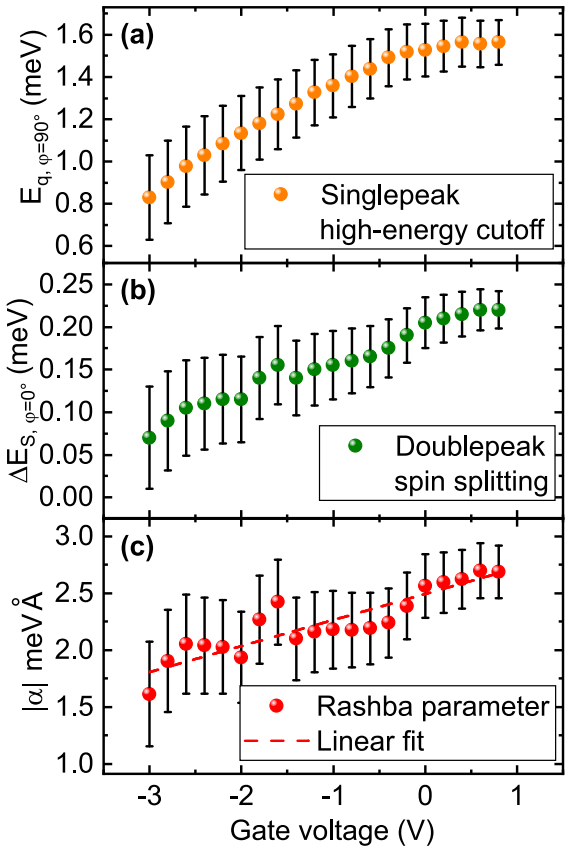

Figure 4.11 | (a) High-energy cutoff of SDE_{00} single peak (from 4.10 (a)). (b) Extracted spin splitting of SDE_{00} double peak (from 4.10 (b)). (c) Calculated Bychkov-Rashba parameter $|\alpha|$, calculated after Eq. (4.5).

Eq. (2.19), it is given by

$$E_{q,\varphi=90°}(U) = \frac{\hbar^2}{m^*}\, q\, k_F(U), \tag{4.3}$$

with $k_F(U)$ representing the gate-voltage-dependent Fermi wave vector. This energetic position should not strongly be affected by a slight variation of the peak width $\Delta E_{S,\varphi=90°}$, induced by a change of α. Next, we will investigate the spin splitting $\Delta E_{S,\varphi=0°}$ extracted from Fig. 4.10 (d), under influence of an external gate voltage. The extracted values are displayed in Fig. 4.11 (b). Note, that the energetic separation of the peaks "d_1" and "d_2" is twice the spin splitting $\Delta E_{S,\varphi=0°}$ (see Sec. 2.4.3). As a consequence of Eq. (2.31) it can be written as

$$\Delta E_{S,\varphi=0°}(U) = 2(|\alpha| + \beta)k_F(U), \tag{4.4}$$

with the assumption that the gate voltage acts only on the Fermi wave vector k_F. For a small change of $|\alpha(U)|$, we assume $|\alpha(U)| = \beta$ and rewrite Eq. (4.4) as

$$\Delta E_{S,\varphi=0°}(U) = 4\,|\alpha(U)|\,k_F(U).$$

By using Eq. (4.3), we eliminate $k_F(U)$ and write

$$|\alpha(U)| = \frac{\Delta E_{S,\varphi=0^\circ}(U)}{E_{\boldsymbol{q},\varphi=90^\circ}(U)} \cdot \frac{\hbar^2 q}{4m^*} \tag{4.5}$$

This result is plotted in Fig. 4.11 (c). The error bars for this consideration are quite high due to noise, but the tendency for an increase of $|\alpha|$ for positive gate voltages, and a decrease for negative gate voltages is demonstrated. This is expected, because the induced external electric field for positive gate voltages points parallel to the intrinsic electric field and vice-versa (cf. Fig. 2.6 (c)). From this measurement, the intrinsic Bychkov-Rashba SO-field strength (at zero gate voltage) of $|\alpha| = (2.56 \pm 0.30)\,\text{meV Å}$ can be extracted.
Later in external in-plane magnetic field measurements (see Sec. 4.6.1) we extract for sample B the value of $|\alpha| = (3.25 \pm 0.25)\,\text{meV Å}$. Those measurements were acquired in backscattering geometry and without a semitransparent top gate, which might be the reason for the deviation.

4.4 Out-of-plane external magnetic fields: Magneto luminescence

In the presence of an out-of plane external magnetic field, the density of states of a 2DES is subject to Landau quantization (see Sec. 2.5.2), which strongly affects the photoluminescence response and can be used as an accurate tool to determine the charge-carrier density. In the first part of this section, magnetoluminescence measurements on sample B* in grazing-incident geometry are utilized to determine the electron density of this sample. In the second part, the effect of an external gate voltage on the magneto luminescence is demonstrated.

4.4.1 Determination of the charge-carrier density

The PL maximum for this sample is located at 1.537 eV (806.7 nm), which was determined in Figs. 4.2 and 4.8. To avoid interferences with the emerging cyclotron resonances of quasi free electrons from the 2DES (later shown in Sec. 4.5), a laser excitation energy of 1.698 eV (730 nm) was used, which is sufficiently above the fundamental transition energy. Since this investigation was performed at the gated sample B*, the gate voltage was pinned to 0 V in the first part of this section. Figure 4.12 (a) shows a logarithmic 3D waterfall plot of PL spectra for an external out-of plane magnetic field

sweep from 0 to 4 Tesla in 0.1 T steps. For $B_{\text{ext}} = 1.1\,\text{T}$, 10 Landau resonances appear in the high-energetic PL flank.

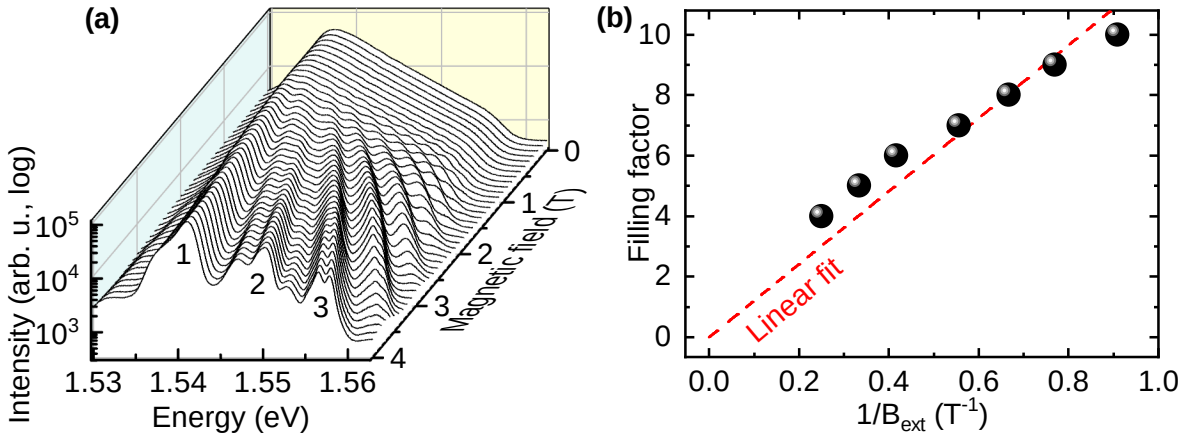

Figure 4.12 | (a) PL spectra of sample B* for magnetic fields from 0 to 4 T in 0.1 T steps. (b) Fan diagram: Filling factor plotted against 1/B.

This number represents the filling factor of the system and is reduced by increasing $\boldsymbol{B}_{\text{ext}}$, due to depopulation of the highest occupied Landau level (see Sec. 2.5.2). For $B_{\text{ext}} > 1.6\,\text{T}$, additional peaks emerge besides the resonances marked as "2" and "3". They might be assigned to hole resonances, since valence band states are also subjected to Landau quantization. However, they are not counted in the electron filling factor determination. The filling factor versus the inverse external magnetic field is plotted in Fig. 4.12 (b). By using Eq. (2.42), a charge carrier density of $n_{2D} = (5.84 \pm 0.23) \times 10^{15}\text{m}^{-2}$ can be extracted from the slope of linear fit (red dashed line in Fig. 4.12 (b)). This electron density is in good agreement with the density extracted for sample B from RILS measurements shown later in Sec. 4.6.1. It should be stressed at this point, that the pinning of the gate voltage to 0 V leads to a drain of the charge carriers, which are radiatively generated by the incident laser. Therefore we assume that the actual charge-carrier density for this sample is somewhat higher.

4.4.2 Effect of electrical gating

In Sec. 4.3.2 we have seen that by tuning the external gate voltage, one can efficiently change the charge-carrier density of the 2DES. This effect can also be addressed by investigating the responding Landau resonances in external out-of plane magnetic fields. Fig. 4.13 shows photoluminescence spectra of sample B* for different gate voltages at fixed external magnetic fields for 2, 4 and 6 T. The filling factors (number of Landau resonances) at zero gate voltage for each magnetic field are in accordance with

the results from Fig. 4.12. Most prominent in all shown measurements, besides the electron Landau resonances, is the appearance of additional peaks (hole resonances) for $B_{\text{ext}} > 1.6\,\text{T}$, which we have already seen in Fig. 4.12 (a). Understanding of the complex structure of these hole resonances is beyond the scope of this thesis.
Compared to the I-V characteristics from Sec. 4.3.1 (conducted at zero external magnetic field), the threshold voltage of 0.92 V, before the current limit is reached, significantly increases. This might be explained by a damping effect of the electron injection into the 2DES, since for out-of plane external magnetic fields, charge carriers are forced into lateral cyclotron trajectories. This is supported by the measurement shown in Fig. 4.13 (a), where the filling factor for positive gate voltages (injection of charge carriers) in the shown range only increases by one count, whereas in the negative direction, it decreases by four counts.
When comparing the PL spectra for negative gate voltages below $U < -3.7\,\text{V}$, in which the system is in the excitonic regime, it is noticeable that a peak splitting can be detected for all measurements. This can be attributed to a splitting into the neutral (X^0, right peak) and charged (X^-, left peak) exciton. For n-doped systems, one expects the formation of negatively charged excitons, where the binding energy compared to the neutral exciton is reduced by about 1-2 meV [Kau00]. From Fig. 4.13 (a) we extract an energetic difference of 1.2 meV between both peaks. An exact determination of the energetic difference from Fig. 4.13 (b) and (c) is not possible, since the intensity of peak X^- increases with higher magnetic fields and saturates in both measurements. In principle, this excitonic splitting should also be visible in measurements without external magnetic field (see Fig. 4.8 (a)), which is not the case. It is possible that under the influence of an external magnetic field, the 2DES is not depopulated as much, so that charged excitons may also be generated.

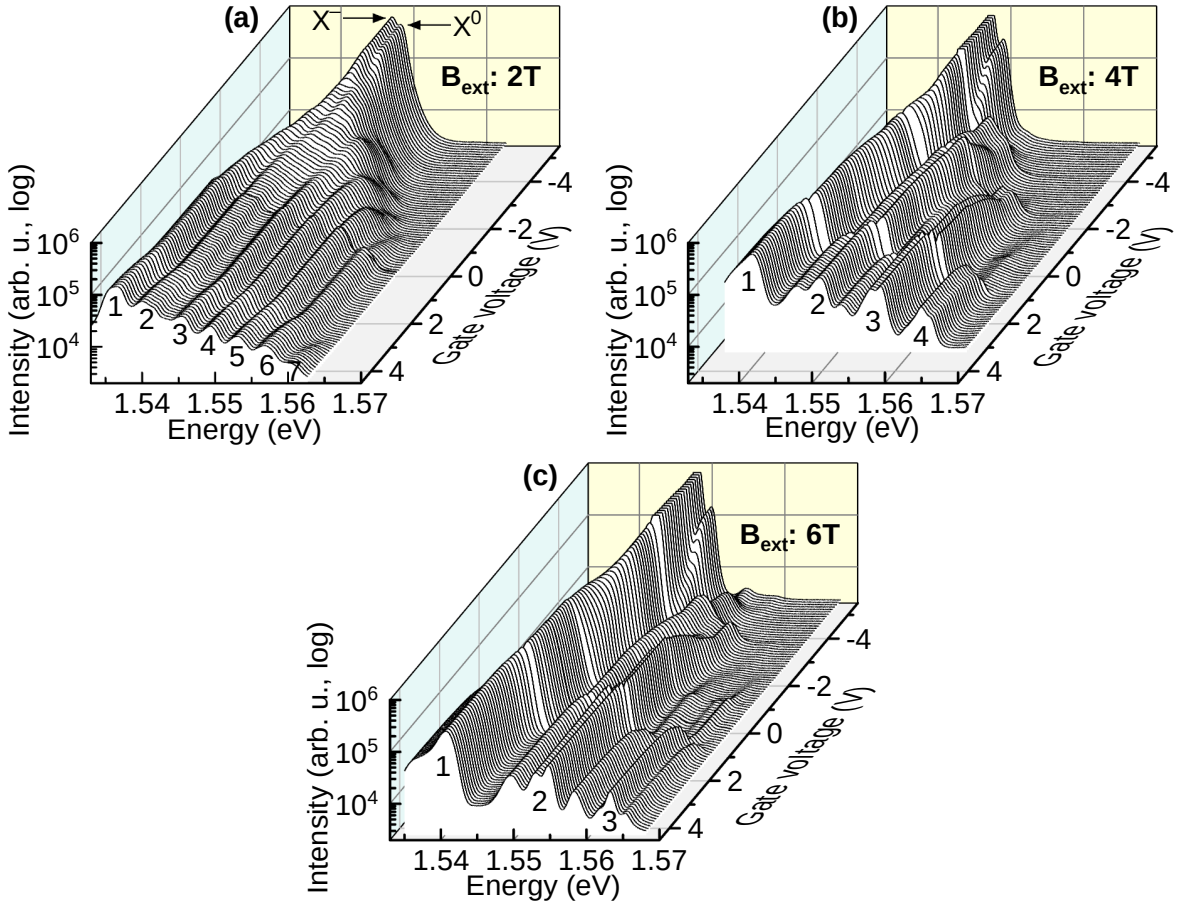

Figure 4.13 | PL spectra of sample B* for gate sweeps at fixed out-of plane external magnetic fields $B_{\text{ext}} = 2, 4$ and 6 Tesla. For higher magnetic fields, a complex structure of additional hole Landau resonances appears.

4.5 Out-of-plane external magnetic fields: Spin-density excitations

Now we turn to resonant inelastic light scattering measurements on spin-density excitations in the presence of an external out-of plane magnetic field. For this purpose, the laser excitation energy has been tuned to the optimum resonance condition for each sample (see Sec. 4.2.2). Besides the Landau quantization of the photoluminescence signal in our RILS spectra (see Sec. 4.4), we expect cyclotron resonances of quasi-free electrons in the 2DES, because of the high electron densities. The transition from the spinflip SDE regime (see Sec. 2.4.3) into the cyclotron resonance regime with increasing magnetic field will be investigated in this section. Related studies have been carried out by Jusserand et al. [Jus03], and Schönhuber [Sch16a], with the difference, that these measurements were each conducted in backscattering geometry to ensure a wave-vector

transfer due to tilting of the sample (see Sec. 3.1.3), causing an in-plane component of the external magnetic field. In the present work, however, we were able to observe the transition of the spinflip SDE regime into the cyclotron resonance regime in an exact out-of plane external magnetic field with a simultaneous wave-vector transfer. This is realized by utilizing the grazing-incidence measurement geometry (see Sec. 3.1.3).
We start with an overview, showing all emerging low-energy Raman resonances together with the photoluminescence and its superpositions in the relevant spectral range. This will be demonstrated on sample B, since it provides the stronger signal due to its higher electron density and mobility, compared to sample A. Next, we will focus on the transition of SDE resonances into the cyclotron resonance regime for moderate external magnetic fields and determine the effective electron mass. At the end of this section, we will turn to polarized scattering geometry, allowing only nonspinflip excitations of charge-density type.

4.5.1 Near resonant magnetic field sweep: overview

Since an optically excited 2DES shows a very complex resonance pattern under the influence of a perpendicular magnetic field, an overview of the relevant spectral region is achieved by a magnetic field sweep over a wider range. The spectrometer and camera settings were optimized for a comprehensive representation of the photoluminescence together with low-energetic RILS spectra. The wave-vector transfer is parallel to the [110] crystal direction, where for sample B a SDE single peak occurs (see Fig. 2.12 (d)). The laser power was set to 10 mW and a spectrometer exposure time of 10 s is used.
Figure 4.14 (a) shows a waterfall plot of RILS spectra for an out-of plane external magnetic field sweep from 0 to 6 Tesla in crossed-polarized geometry with a wave-vector transfer of $q = 7.92 \times 10^6\,\mathrm{m}^{-1}$. On the right hand side, the PL maximum at 24.8 meV (absolute energy 1.537 eV) appears. For increasing $\boldsymbol{B}_{\mathrm{ext}}$, we see cyclotron resonances linearly fan out from 0 meV. Starting at around 1 T, a complex pattern of double resonances between cyclotron resonances and photoluminescence Landau resonances emerges. A clearer illustration of all appearing peaks is given in Fig. 4.14 (b), showing a heatmap (energy versus magnetic field) of all spectra in a logarithmic intensity scale. The horizontal line at 0 meV is the Rayleigh backscattered laser light. Close to the coordinate origin, the SDE_{00} resonance (green diffuse signal) is located at about 1.5 meV, for increasing magnetic field it shows a slight redshift. By further increasing $\boldsymbol{B}_{\mathrm{ext}}$, it smoothly changes into a Landau fan, which develops continuously for moderate magnetic fields and shows discrete clusters (double resonances) for $B_{\mathrm{ext}} \gtrsim 1\,\mathrm{T}$. The

clusters at very low Raman shifts (above the Rayleigh laser line), at $B_{\text{ext}} \gtrsim 1\,\text{T}$ can be attributed to "resonance fluorescence", stemming from direct radiative recombinations of excited electrons. The splitting of the PL for increasing magnetic fields is much more complex and shows also non-linear characteristics. This might be explained by an additional Landau quantization of the valence band, which complicates the resonance situation considerably. Since we will study the influence of external magnetic fields on low-energy SDE excitations, we can conclude from these measurements that SDE resonances only exist for moderate B-fields.

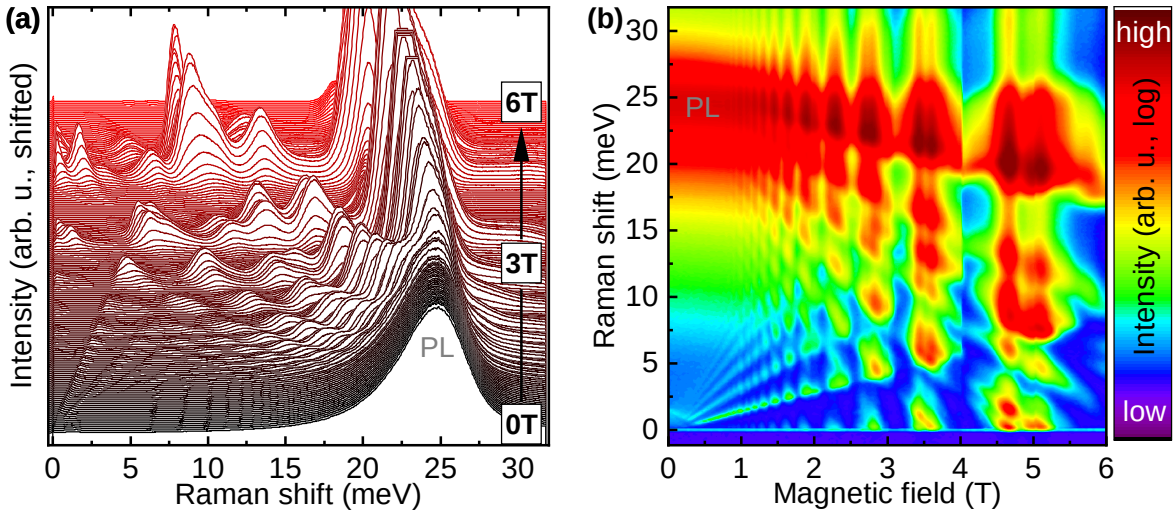

Figure 4.14 | (a) Waterfall plot of RILS spectra of sample B for an external out-of plane magnetic field sweep between 0 and 6 Tesla. (b) Heatmap of spectra from (a) in a logarithmic intensity scale. The emerging clusters for higher magnetic fields are attributed to double resonances of PL Landau transitions and cyclotron resonances.

4.5.2 SDE response and cyclotron resonances

Sample B

We start by analyzing the low-energetic spectral region from Fig. 4.14 with a relatively long spectrometer exposure time of 240 s, but otherwise the same experimental settings. The two extreme cases for a wave-vector transfer $\boldsymbol{q}$ along crystal directions with minimum ($\varphi = 90°$, single peak) and maximum ($\varphi = 0°$, double peak) spin splitting (see Sec. 2.4.3) are plotted in Fig. 4.15 (a) and (b). In these waterfall plots, an out-of plane external magnetic field sweep between 0 and 0.4 T is shown. In the lower magnetic field region between 0 and $\sim 0.16\,\text{T}$, the emerging SDE peaks are labeled as "s" (single peak),"d_1" and "d_2" (double peak). At zero external magnetic field, "s" is located at 1.51 meV, "d_1" at 1.25 meV, and "d_2" at 1.67 meV. By increasing the external magnetic

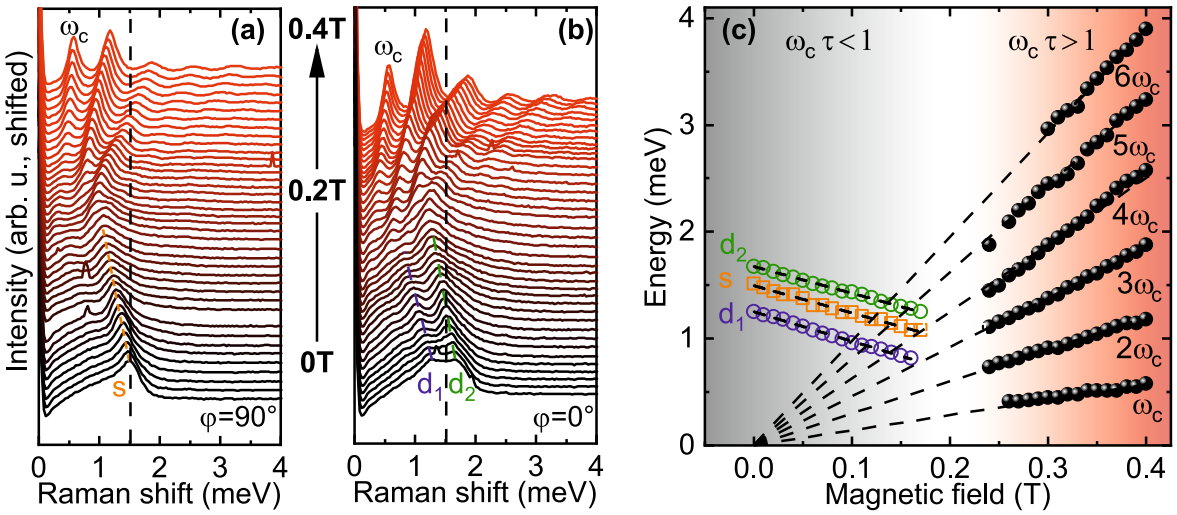

Figure 4.15 | (a) Waterfall plot of RILS spectra from sample B for different external magnetic fields perpendicular to the 2DES plane. The wave-vector transfer points along $\varphi = 90°$. (b) Same as (a), but for a wave-vector transfer along $\varphi = 0°$. (c) Energetic position of all peak maxima from (a) and (b) versus external magnetic field. In the lower field region (gray shaded area), the visible SDE_{00} resonances linearly shift to lower energies. For higher fields (red shaded area), cyclotron resonances appear in a typical Landau fan (black dashed lines are linear fits).

field, we observe a linear redshift for all SDE peaks. The peaks "d_1" and "d_2" also move slightly apart during their shift towards lower energies. At a field of $B_{\text{ext}} \sim 0.16\,\text{Tesla}$, a transition from the SDE regime into a cyclotron resonance regime occurs. In the transition region we see a superposition of the SDE signal with cyclotron resonances, for $B_{\text{ext}} > 0.30\,\text{T}$ a number of 6 cyclotron resonances can be resolved. All energetic peak positions versus external magnetic field are extracted in Fig 4.15 (c). The plot is divided into two zones, which are marked by a color gradient. Together with the single-particle scattering time τ_{sp} and the cyclotron frequency ω_c (see Sec. 2.5.2), we can interpret that in the red zone, the external magnetic field is sufficient for the electrons to perform full cyclotron motions, i.e., $\omega_c\,\tau_{\text{sp}} > 1$. In the gray zone, the magnetic field is too weak for cyclotron resonances to occur ($\omega_c\,\tau_{\text{sp}} < 1$).

In between those two zones, at approximately 0.16 T, where the first cyclotron resonances appear, the magnetic field is sufficient for electrons performing one circular movement ($\omega_c\,\tau_{\text{sp}} = 1$), thus one can estimate the electron scattering time to be 2.8 ps. This value is in good agreement with the single-particle lifetime τ_{sp} which was used in our Lindhard-Mermin simulations (see Fig. 3.7). Another important parameter for the Lindhard-Mermin simulations is the effective electron mass m^* (see Eq. (2.39)), which can be extracted from the slope of the cyclotron resonance linear fits (black dashed

lines). Considering all visible cyclotron resonances, we extract the following values from Fig. 4.15 (c):

ω_c	$2\,\omega_c$	$3\,\omega_c$	$4\,\omega_c$	$5\,\omega_c$	$6\,\omega_c$
$0.079\,m_e$	$0.077\,m_e$	$0.075\,m_e$	$0.073\,m_e$	$0.072\,m_e$	$0.071\,m_e$

The decreasing effective electron mass for higher order cyclotron resonances can probably be explained by the nonparabolicity of the conduction band [Eke89, Ruf90]. Another reason for this behavior is the penetration of the electron wave function into the AlGaAs barrier material, since the effective mass for bulk AlGaAs is lower than for GaAs. Due to a finite height of the potential barrier, higher energetic transitions are more probable to penetrate into the barrier material, which reduces their mass. Since we want to extract a realistic value of m^* for the Lindhard-Mermin simulations of our experimental SDE_{00} spectra, which occur close to the Fermi energy (see Eq. (3.11)), the lowest order transition ω_c provides the best value of $0.079\,m_e$ for sample B.
To quantitatively compare the linear shift of the SDE_{00} resonances "s", "d_1" and "d_2" for moderate external magnetic fields, we will describe the occurring shift of their energetic positions in terms of a negative effective electron mass via the relation $E = \hbar\,\frac{eB}{m^*}$. We extract the following values:

s	d_1	d_2
$-0.045\,m_e$	$-0.042\,m_e$	$-0.046\,m_e$

One possible mechanism for the redshift of the SDE peaks might be explained by a gradual increasing of Landau quantization for electron states inside the conduction band. By increasing the external magnetic field, Landau levels move apart from each other (see Sec. 2.5.2), creating energy gaps that doesn't allow the finite electron states of an SDE excitation to be addressed. However, further experimental and theoretical investigations are required to understand the physical mechanisms of this effect. For a comparable 2DES system, but only considering Dresselhaus SO interaction, R. Winkler [Win03] analytically calculated a vanishing spin splitting at a perpendicular external magnetic field of $B_{\text{ext}} = 0.8\,\text{T}$. In Ref. [Sch08], a full quantum mechanical approach to describe the ballistic cyclotron motion of electrons under the influence of Bychkov-Rashba spin-orbit coupling is investigated, aiming to describe a magnetic focusing effect in semiconductor quantum wells. Until now, there has been no theoretical treatment of a system with both, Dresselhaus and Bychkov-Rashba SO interaction, under influence of a perpendicular external magnetic field, which would be indispensable for our investigated system.

Sample A

Similar experiments were performed for sample A. Because of the different orientation of the intrinsic effective spin-orbit field, induced by the configuration of $\alpha \sim \beta$ (see Fig. 2.12 (b)), the minimum spin splitting direction arises for a wave-vector transfer pointing along $\varphi = 0°$. Waterfall RILS spectra for different external magnetic fields perpendicular to the 2DES plane are shown in Fig. 4.16 (a). Spectra with a wave-vector transfer pointing along $\varphi = 90°$ (maximum spin splitting) are depicted in Fig. 4.16 (b). The magnetic field is varied between 0 and 0.6 Tesla and the incident laser wavelength is 792.5 nm (chosen after Sec. 4.2.2). All other settings are the same as for sample B. At first glance one recognizes an overall less favorable signal to noise ratio than for sample B which is most probably due to the lower electron density and mobility for this sample. In the bottom spectra of Fig. 4.16 (a), a prominent PL signal from the fundamental transition is visible. Since this distracting PL signal was stronger in Fig. 4.16 (b), the spectra were processed by subtracting the background via an exponential fit of the PL flank. Thus the cyclotron resonances are better recognizable. The

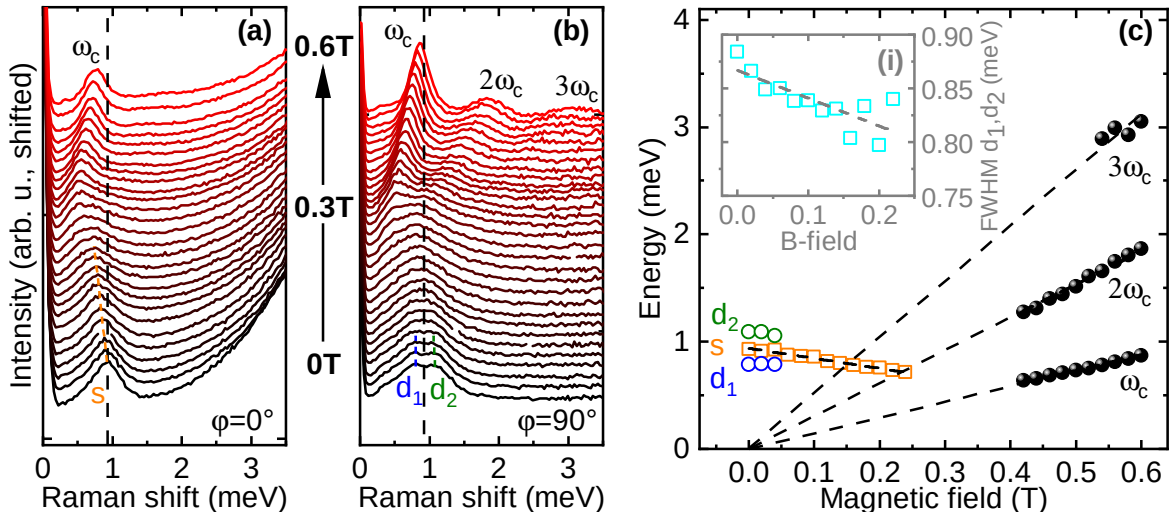

Figure 4.16 | (a) Waterfall plot of RILS spectra from sample A for different external magnetic fields perpendicular to the 2DES plane. The wave-vector transfer points along $\varphi = 0°$. On the right hand side of all spectra, the PL is visible. (b) Same as (a), but for a wave-vector transfer along $\varphi = 90°$. All spectra were processed by subtracting the PL background via an exponential fit. (c) Energetic position of all peak maxima from (a) and (b) versus external magnetic field. The single peak "s" linearly shifts to lower energies for increasing magnetic field. Due to the low signal to noise ratio, the peak splitting of "d_1" and "d_2" is only recognizable for the 3 measurements around $B_{ext} = 0$ T. For higher fields, cyclotron resonances appear in a typical Landau fan (black dashed lines are linear fits). The inset (i) shows the extracted FWHM of the SDE double peak from (b) in the lower magnetic field region.

SDE single peak "s" for $\varphi = 0°$ at zero external magnetic field is located at 0.94 meV.

For $\varphi = 90°$, the two peaks "d_1" and "d_2" are located at at 0.79 meV and 1.09 meV, respectively. Overall, the peaks are at lower energetic positions compared to sample B, which is due to the lower charge-carrier density n of this sample. The SDE cutoff frequency (given by Eq. (2.19)) linearly scales with the wave-vector transfer $\boldsymbol{q}$ and the Fermi wave vector $k_F = \sqrt{2\pi n}$ (see Eq. (2.21)). The difference in $\boldsymbol{q}$ due to the slightly lower laser wavelength, compared to the measurements for sample B, is negligible, so k_F decreases for smaller n.
As for sample B, the SDE single peak "s" linearly shifts towards lower Raman energies for increasing magnetic field. The double-peak feature is only separable in the three bottom spectra of Fig 4.16 (b) to fields of 0.04 Tesla. For higher fields, the peak is blurred out and a slight redshift is visible. For magnetic fields higher than 0.42 T, one cyclotron resonance for $\boldsymbol{q}$ pointing along $\varphi = 0°$, and three resonances for $\boldsymbol{q}$ pointing along $\varphi = 0°$ are observable. All peak positions from Figs. 4.16 (a) and (b) are tracked in Fig. 4.16 (c). The effective electron masses, extracted from the shown linear fits (black dashed lines) are:

ω_c	$2\,\omega_c$	$3\,\omega_c$
$0.079\,m_e$	$0.075\,m_e$	$0.067\,m_e$

As for sample B, we extract $0.079\,m_e$ for the effective electron mass near the Fermi energy. For higher orders, m^* decreases more rapidly which might originate from the double sided doping of this sample and a resulting increased probability density of electrons $|\chi_0|^2$ inside the barrier (see Sec. 2.2.2). Furthermore, according to the nextnano++ simulation of the conduction band potential profile, shown in Fig. 2.5 (c), the quantum well barrier height of this sample is not as high as for sample B (see Fig. 2.6 (c)), which might also increase the probability density of electrons inside the barrier.
Next, we are interested in the progress of the double-peak feature from Fig. 4.16 (b) for increasing external magnetic fields. Because no spectral separation of "d_1" and "d2" can be observed here, the full width at half maximum (FWHM) of the SDE signal was evaluated and is shown in insert (i) in Fig. 4.16 (c) for magnetic fields between 0 and 0.22 T. We see a decrease of the width from 0 to ∼0.18 T, which is contrary to the behavior of sample B, where the peaks positions "d_1" and "d_2" slightly diverged for increasing magnetic field. However this behavior is not significant, because of the low signal to noise ratio. At $B_{ext} \gtrsim 0.18$ T, the FWHM is increasing, which might be an indication for cyclotron resonances to set in ($\omega_c\,\tau_{sp} = 1$). From this, we estimate the single-particle scattering time to be $\tau_{sp} \sim 2.5$ ps, which is comparable to the observed

value for sample B.

4.5.3 Nonspinflip excitations: Polarized measurement geometry

So far we have investigated the intrasubband spin-density excitations in depolarized scattering geometry, with both the incoming and scattered light linearly polarized, but rotated 90 degrees relative to each other. Schönhuber et al. [Sch14] have shown, that in backscattering geometry (see Sec. 3.1.3) for in-plane spin orientations, only spinflip transitions contribute to the intrasubband spin-density excitations in depolarized geometry. In parallel polarization (incoming and scattered light are oriented parallel to each other), nonspinflip excitations of charge-density type are allowed due to polarization selection rules [Ham69, Pin88] (see Sec. 2.4.1). The main results of this section are published in the appendix of Ref. [Gel20].

We present measurements on sample B, recorded under the same experimental conditions as shown in Fig. 4.15, but conducted in polarized measurement geometry. In Figs. 4.17 (a) and (b), the recorded RILS spectra are taken for different external magnetic fields ($B_\perp$) and a wave vector transfer pointing along $\boldsymbol{q} \parallel [110]$ ($\varphi = 90°$) and $\boldsymbol{q} \parallel [\bar{1}10]$ ($\varphi = 0°$), respectively. We will start by discussing the bottom spectra

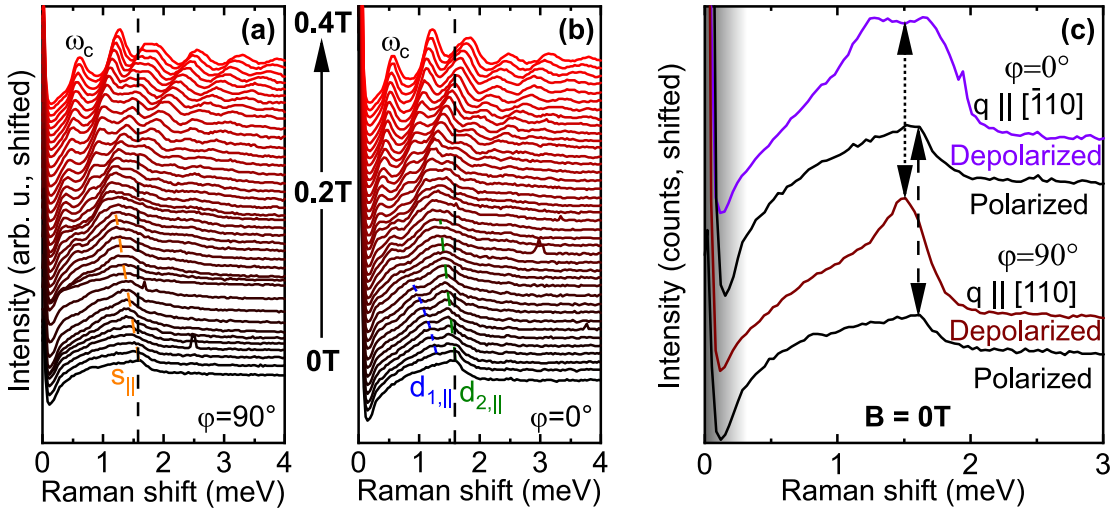

Figure 4.17 | (a) RILS spectra of sample B in polarized measurement geometry for different external magnetic fields $\boldsymbol{B}_\perp$. The wave-vector transfer points along $\varphi = 90°$. (b) Same as (a) but with the wave-vector transfer pointing along $\varphi = 0°$. (c) Comparison of polarized and depolarized RILS spectra for a wave-vector transfer in two different in-plane directions of sample B. The spectra are shifted vertically for better visibility. The gray shaded area marks the spectrometer cutoff.

taken for zero external magnetic field. In both Figs. 4.17 (a) and (b), single peaks with maximum at 1.61 meV are observed, with the peak in Fig. 4.17 (b) showing a slightly increased intensity. To compare these spectra with the measurements taken in depolarized geometry, Fig. 4.17 (c) shows all measurements taken at zero external magnetic field together. In depolarized geometry, the single peak (brown line) recorded along $\varphi = 90°$ lies in the middle between the two spin-split maxima for $\varphi = 0°$ (purple line). In polarized geometry, only a single peak emerges for both orientations of φ (black lines). This is expected, since in this scattering geometry only transitions within a spin subband contribute, and, hence, their energies are approximately independent of the spin splitting for a given wave-vector transfer $\boldsymbol{q}$. There are only very small deviations expected due to the slightly different Fermi momenta for the different in-plane directions. This effect is, however, negligibly small. The remaining collective shift due to electron-electron exchange interaction between the excitations in polarized and depolarized scattering geometry is only about 0.1 meV (difference between vertical double arrows in Fig. 4.17 (c)). This result is consistent with previous investigations [Ber90, Sch16a].

Let us now turn to the external magnetic field dependency. For $\varphi = 90°$ (Fig. 4.17 (a)), peak "$s_{\parallel}$" shows a redshift, similar to measurements in depolarized geometry (cf. Fig. 4.15 (a)). In Fig. 4.17 (b), a second peak "$d_{1,\parallel}$" emerges for finite magnetic fields between 0.01 and 0.15 T and shifts nonlinear towards lower energies. This second peak is not expected, since only nonspinflip transitions are allowed in polarized geometry. The external magnetic field might cause a disturbance, so that spinflip transitions may partially be possible. For better comparison, all peak positions for depolarized and polarized measurement geometry for small magnetic fields are tracked in Fig. 4.18. The filled symbols represent the peak positions measured in polarized geometry, the open symbols show the results from depolarized geometry. For a wave-vector transfer along $\varphi = 90°$ (minimum spin splitting direction), the slope of "$s_{\parallel}$" (solid orange square) is comparable with "s" (open orange square), recorded in depolarized geometry. For measurements along $\varphi = 0°$ (maximum spin splitting direction), the shifts of the observable peaks "$d_{1,\parallel}$" and "$d_{2,\parallel}$" differ significantly from the measurements in depolarized geometry. At this point, the origin of the peak "$d_{1,\parallel}$" is not clear, which only occurs for finite magnetic fields. Also the mechanisms for the reduced shift of peak "$d_{2,\parallel}$" is not understood, which requires further experimental and theoretical investigation. Finally it should be noted that in polarized measurements, the observed cyclotron resonances are located at the same energetic positions, compared to measurements in depolarized geometry (cf. Figs. 4.15 (a) and (b)). This indicates the single-particle character of

these excitations, which was also reported in Ref. [Sch97].

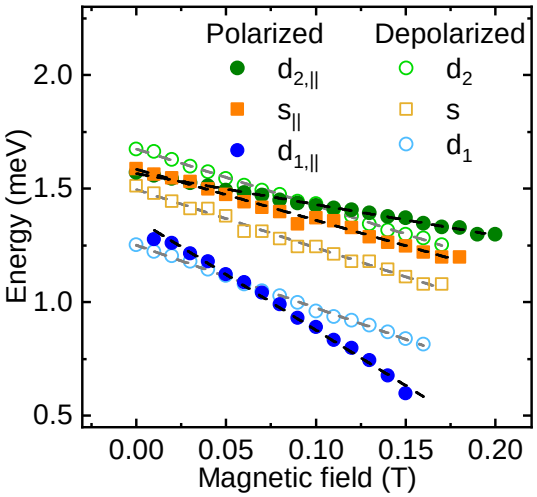

Figure 4.18 | Comparison of the energetic peak positions from polarized and depolarized RILS spectra for external magnetic fields $\boldsymbol{B}_\perp$. The peaks were extracted from Figs. 4.15 and 4.17.

4.6 In-plane external magnetic fields

In this section, a further understanding of the spin-orbit parameters is obtained by performing RILS experiments on two different in-plane orientations of the persistent spin helix. In particular, we compare the two configurations $\alpha = \beta$ (sample A) and $\alpha = -\beta$ (sample B). A wave-vector transfer $\boldsymbol{q}$ into arbitrary in-plane crystal directions is realized by rotating the samples on a rotary stage (see Sec. 3.1.3), allowing us to map the spin splitting anisotropy for in-plane spins (see Sec. 2.4.3). Maximum spin splitting occurs parallel to [110] or parallel to $[1\bar{1}0]$ crystal directions respectively, depending on the configuration of $\alpha = \pm\beta$. By applying an in-plane external magnetic field, a superposition of the intrinsic spin-orbit field and the external field occurs, which allows us to modulate the effective magnetic field (see Sec. 2.5). This has a direct impact on the spin splitting, detected in our SDE spectra. Via the numerical Lindhard-Mermin lineshape analysis, we determine the relevant material parameters. We find that the linear strength of the spin-orbit parameters $|\alpha| = \beta$ is comparable for both samples, while the electron g factors are markedly different. In addition, the external field measurements allow us to determine the strength of the internal spin-orbit fields, which are as high as $B_{SO} \sim 18\,\mathrm{T}$ for both investigated samples. The main results of this section were published in Refs. [Gel18, Gel20].

4.6.1 Angular mapping of the spin-splitting anisotropy

Sample A

We will start by discussing the RILS experiments on sample A. Figure 4.19 (a) shows a waterfall plot of depolarized spectra, taken at zero external magnetic field for a tilt angle of $\theta = 35°$, leading to a wave-vector transfer of $q = 9.1 \times 10^6$ m^{-1}. A spectrometer exposure time of 240 s is used for each spectrum. The sample is rotated via the rotary stage in steps of 15° between positions $\varphi = 0°$ and $\varphi = 360°$. All spectra are normalized and vertically shifted for better comparison. The gray shaded area marks the triple Raman spectrometer cutoff. One clearly recognizes a lineshape evolution from a typical Lindhard-Mermin lineshape ($\varphi = 0°$) to a superposition of two spectra with two different maxima (indicated by gray dashed lines), with a maximum peak distance at $\varphi = 90°$. This pattern repeats periodically when φ is rotated by 360°, which follows the expected spin splitting due to the effective spin-orbit field, shown in Fig. 2.12 (b).

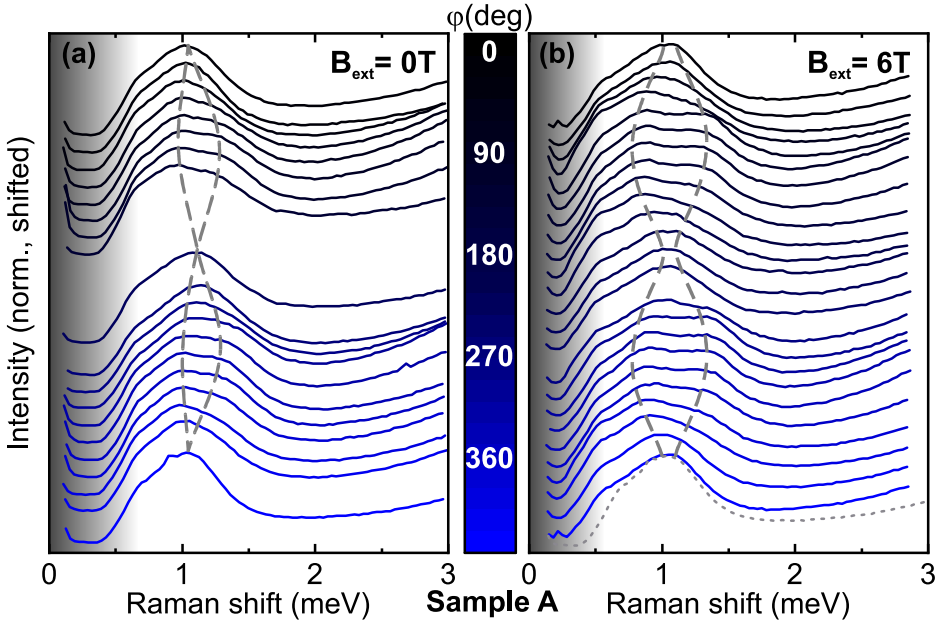

Figure 4.19 | (a) Waterfall plot of depolarized RILS spectra of sample A at a tilt angle of $\theta = 35°$, corresponding to a wave-vector transfer of $q = 9.1 \times 10^6$ m^{-1} for different in-plane directions φ (relative to $[\bar{1}10]$) at zero external magnetic field. (b) Same as (a) but for an in-plane external magnetic field of $B_{\text{ext}} = 6$ T. For comparison of the single peak width, a spectrum taken at zero external field is inserted (dotted gray spectrum at the bottom). The gray shaded area marks the spectrometer cutoff. The positions of the maxima are traced by the gray dashed lines.

When an external magnetic field $\boldsymbol{B}_{\text{ext}}$ is applied in-plane to the effective spin-orbit field $\boldsymbol{B}_{\text{SO}}$ (as indicated in Fig. 3.3 (a)), for each position of φ, the transferred wave vector

is perpendicular to the magnetic field ($\boldsymbol{B}_{\text{ext}} \perp \boldsymbol{q}$). This leads to a superposition of the intrinsic and the external field, disturbing the unidirectionality of the total effective magnetic field acting on electrons inside the 2DES. Figure 4.19 (b) shows a φ series for $B_{\text{ext}} = 6\,\text{T}$, oriented parallel to the intrinsic SO-field $\boldsymbol{B}_{\text{so}}$, so they add up. The distance of the two different maxima increases globally due to the increased effective spin-orbit field, as indicated by the gray dashed lines. For $\varphi = 0°$ and 180°, where no intrinsic SO-field is present, a peak splitting emerges, which can only be induced by the external field. To clarify this effect, a single peak spectrum (gray dotted line), recorded at zero external field has been inserted in Fig. 4.19 (b).

For an accurate extraction of the maxima positions, i. e., the cutoff energies of the spin-flip transitions, all recorded spectra were reproduced by the computational Lindhard-Mermin lineshape analysis, based on the Lindhard-Mermin line shape [Mer70, Fas87], described in Sec. 3.2. A detailed analysis of the two extreme cases $\varphi = 0°$ and $\varphi = 90°$ is exemplarily shown in Fig. 3.7, where the measured lineshape can be nicely reproduced by the simulation. The single peak lineshape at $\varphi = 0°$ is best rendered, when we use the following material parameters: An electron temperature of 12 K, which is in accordance with the estimated 2DES temperature from Sec. 4.2.3), a single-particle scattering time of $\tau_{\text{sp}} = 3\,\text{ps}$ (we found a comparable value of 2.5 ps in Sec. 4.5.2 under the influence of perpendicular magnetic fields), and an electron density of $n = (2.7 \pm 0.3) \times 10^{15}\,\text{m}^{-2}$. Here, the arithmetic mean value of n, obtained from all Lindhard-Mermin simulations was taken. We assume that the short electron lifetime is caused by the strong Landau damping of the SDE_{00}, which lies energetically inside the single-particle continuum (see Fig. 2.15). The smaller electron density here, as compared to the indicated value of the manufacturer (determined by transport measurements [Wal12a], see Table 2.1) might be explained by the strong laser illumination in our experiments. This "optical gating" effect has been discussed at the end of Sec. 4.2.3.

All spectra with nonzero spin splitting are reproduced by the superposition of two simulated curves I_q^+ and I_q^- (see Fig. 3.7). By varying Δk_φ (see Eqs. (2.16) and (2.31)), the simulation is adapted until it matches the measured spectra. From the simulation data, we extract $\Delta E_{S,\varphi}$, which is twice the spin splitting (see Fig. 2.17 (b)), for the corresponding in-plane crystal direction.

All results of the Lindhard-Mermin analysis for sample A are summarized in Fig. 4.20. In this polar plot, the inner open circles represent the extracted spin splittings $\Delta E_{S,\varphi}$ versus φ, the angle relative to $[\bar{1}10]$ in-plane direction, for zero external magnetic field. Maximum spin splitting occurs at $\varphi = 90°$ and 270°. At this positions, we extract

$\Delta E_S = (0.19 \pm 0.01)$ meV, whereas for $\varphi = 0°$ and 180°, no spin splitting is observable (cf. [Sch14]). The solid gray line represents the computed values for the expected $\sin\varphi$ dependent spin splitting after Eq. (2.16). By adapting this calculation to the measured data, under consideration of Eq. (2.31), we obtain the intrinsic spin-orbit parameters $(\alpha + \beta)/2 = \alpha = \beta = (3.50 \pm 0.25)$ meV Å when using $n = 2.7 \times 10^{15}\,\mathrm{m}^{-2}$ for the electron density in the 2DES, as received from the lineshape analysis, discussed above. Compared to the obtained parameters α and β in Ref. [Wal12a], from a different piece of the wafer, they are somewhat higher here. Those experiments were performed at a higher nominal temperature of $T = 40\,\mathrm{K}$. Moreover a transient in Δk stemming from a finite excitation spot size [Sal14], has not been taken into account in the analysis. Compared to RILS experiments in Ref. [Sch14], the parameter values are also slightly higher here. This can be explained by a different laser excitation energy used in our experiments, leading to different resonance conditions and, therefore, a changed electron density, corresponding to a different electric field across the quantum well.

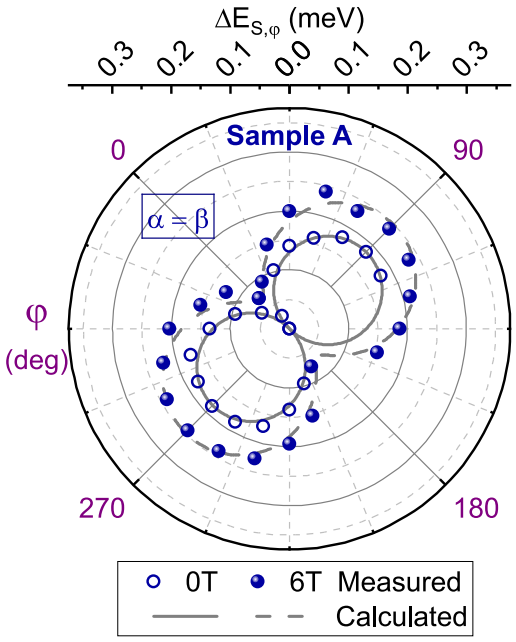

Figure 4.20 | Polar plot of extracted peak splittings versus angle φ (relative to $[\bar{1}10]$ in-plane direction) for sample A at zero external magnetic field (inner open circles) and for external in-plane magnetic fields of 6 Tesla (outer solid circles). The gray lines show the calculated $\sin\varphi$ dependence of the peak splitting (see Eqs. (2.36 and 2.38)).

Let us now turn to the detailed analysis of the peak splittings from Fig. 4.19 (b), obtained in an external magnetic field of $B_{\mathrm{ext}} = 6\,\mathrm{T}$ for sample A. The extracted peak splittings from our Lindhard-Mermin lineshape analysis are shown in Fig. 4.20 as the blue solid dots. As stated above, a global increase of the spin splittings can be found due to a disturbance of the unidirectional character of the intrinsic spin-orbit field $\boldsymbol{B}_{\mathrm{SO}}$. We find an increased spin splitting with maxima at $\Delta E_S = (0.24 \pm 0.01)$ meV at $\varphi = 90°$ and 270°, where $\boldsymbol{B}_{\mathrm{ext}}$ is oriented parallel to $\boldsymbol{B}_{\mathrm{SO}}$. Along the orthogonal in-plane axis,

i.e., $\varphi = 0°$ and 180°, a finite spin splitting of $\Delta E_S = 0.15\,\text{meV}$ emerges. This can only stem from a Zeeman splitting, induced by the applied external magnetic field $\boldsymbol{B}_{\text{ext}}$. Again, the computed values (gray dashed line in Fig. 4.20) are in good agreement with the extracted spin splittings from our experiments. They were calculated by using the relation $\Delta E_{S,B}(\varphi) = g\mu_B|\boldsymbol{B}_{\text{tot}}(\varphi)|$ (see Eqs. (2.36 and 2.38)), with $\boldsymbol{B}_{\text{tot}}$ being the total effective magnetic field constituted by a superposition of $\boldsymbol{B}_{\text{ext}}$ and $\boldsymbol{B}_{\text{SO}}$. The calculation matches best with the measured spin splittings, using the same values for $\alpha = \beta$ and n as for $B_{\text{ext}} = 0\,\text{T}$, and a $|g|$ factor of 0.16 ± 0.04. According to [Yug07], this g factor corresponds to a symmetric GaAs quantum well with nominal width of 8 nm, and will be discussed later in more detail.

Sample B

We will now turn to measurements on sample B, which has a negative Bychkov-Rashba spin-orbit parameter $\alpha = -\beta$. The orientation of the intrinsic spin-orbit field $\boldsymbol{B}_{\text{SO}}$ is also unidirectional, but compared to sample A, its maximum field strength points along the orthogonal in-plane direction (see Fig. 2.12 (c)). Our measured RILS spectra for sample B taken at zero external magnetic field are shown in Fig. 4.21 (a). The spectra were recorded for a tilt angle of $\theta = 40°$ ($q = 10.2 \times 10^6\ \text{m}^{-1}$) and a spectrometer exposure time of 10 s for each spectrum. Spectra recorded along prominent crystal directions (minimum and maximum spin splitting directions) are colored blue for clearer presentation. In contrast to sample A, the maximum spin splitting now emerges for $\varphi = 0°$ and 180°, whereas a single peak is present for $\varphi = 90°$ and 270°, respectively. For all intermediate positions of φ between minimum and maximum spin splitting, a redshift of the spectra can be observed. With a constant wave-vector transfer $\boldsymbol{q}$ and electron density n, one would not expect such a shift, since the high-energy cutoff of the SDE single peak is described by $E_q = \frac{\hbar^2}{m^*} k_F\, q$, with $k_F = \sqrt{2\pi n}$ (see Eqs. (2.19) and (2.21)). If a spin splitting due to the two different spinflip transitions is considered we expect the two comprising transitions E_q^+ and E_q^- (see discussion around Fig. 2.17) to distribute symmetrically around the single-peak energy E_q, as we have seen for sample A. We assume this shift to originate from a change in n caused by inhomogeneities of the donor distribution in the sample: The laser spot may vary locally on the sample surface during a φ series, if the rotation axis is not aligned perfectly with the laser position. In other recorded φ series (not shown) at a different measurement spot, a slight blueshift of the spectra for the intermediate φ positions was observed. Figure 4.21 (b) shows measurements for an external in-plane magnetic field of $B_{\text{ext}} = 6\,\text{T}$, which was, as for sample A, applied parallel to the intrinsic spin-orbit field $\boldsymbol{B}_{\text{SO}}$. For maximum

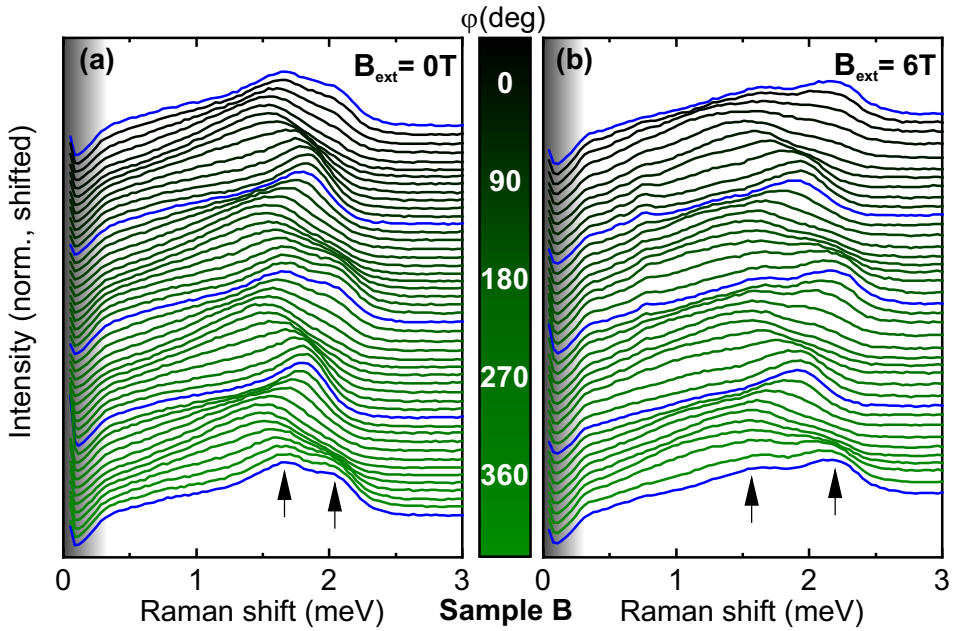

Figure 4.21 | (a) Waterfall plot of depolarized RILS spectra of sample B at a tilt angle of $\theta = 40°$, corresponding to a wave-vector transfer of $q = 10.2 \times 10^6$ m^{-1} for different in-plane directions φ (relative to $[\bar{1}10]$) at zero external magnetic field. (b) Same as (a) but for an in-plane external magnetic field of $B_{\text{ext}} = 6$ T. The gray shaded area marks the spectrometer cutoff. For better orientation, crystal directions with minimum and maximum spin splitting are marked as the blue solid lines.

spin splitting directions ($\varphi = 0°$ and $180°$), we clearly see a diverging of the two comprising sub peaks (exemplary highlighted by black arrows), as we expect it due to the superposition of $\boldsymbol{B}_{\text{ext}}$ and $\boldsymbol{B}_{\text{SO}}$. Again, for all intermediate positions of φ between minimum and maximum spin splitting, a redshift of the spectra occurs, since the same spot position as for zero external field measurements was used. All spin splittings were extracted by using the Lindhard-Mermin lineshape analysis. The results are shown in Fig. 4.22. We extract a maximum spin splitting of $\Delta E_S = (0.20 \pm 0.01)$ meV at $\varphi = 0°$ and $180°$ for zero zero external magnetic field (green open circles) and $\Delta E_S = (0.34 \pm 0.01)$ meV for $B_{\text{ext}} = 6$ T. The extracted sample parameters from the Lindhard-Mermin lineshape analysis are an electron temperature of $T = 12$ K (comparable with sample A and Sec. 4.2.3), a single particle scattering time of $\tau_{\text{sp}} = 3$ ps and an electron density of $n = (5.8 \pm 0.7) \times 10^{15}$ m^{-2}. The larger error is due to the fluctuation in the electron density discussed above. As for sample A, the arithmetic mean value of n, obtained from all Lindhard-Mermin simulations was taken. The gray solid and dashed lines in Fig. 4.22 show the calculations for the angular dependent spin splitting $\Delta E_{S,B}(\varphi)$ (see above), where the electron density is fixed at $n = 5.8 \times 10^{15}$ m^{-2} and for the spin orbit parameters we use $\alpha = -\beta = (-3.25 \pm 0.25)$ meV Å. The deviation

from the calculated values in particular for $B_{\text{ext}} = 0\,\text{T}$ might stem from the above discussed sample inhomogeneity and change of the measurement position while rotating the sample. The measurements at $B_{\text{ext}} = 6\,\text{T}$ are fitting much closer to the calculated values. The clearly enlarged spin splitting, compared to sample A can be explained by

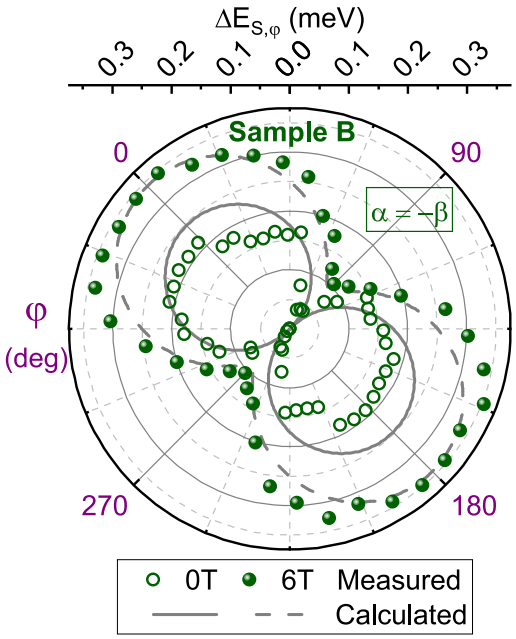

Figure 4.22 | Same as in Fig. 4.20, but for sample B at a tilt angle of $\theta = 40°$, corresponding to a wave-vector transfer of $q = 10.2 \times 10^6\ \text{m}^{-1}$. The increased peak splitting is due to the higher electron density of this sample.

the higher electron density of sample B. This is obtained by the relation $k_F = \sqrt{2\pi n}$ and Eq. (2.31), which leads to an increase of $\Delta E_{S,\varphi}$. We extract a $|g|$ factor of 0.23 ± 0.07 from these measurements for sample B, which is surprisingly almost 50% larger than the determined value for sample A. After Ref. [Yug07], this value corresponds to a symmetric GaAs quantum well width of about 10 nm. It should be stressed, that the here presented analysis is only concerning an isotropic in-plane g factor. In fact, an anisotropy for GaAs-AlGaAs quantum wells with asymmetric quantum-well potential was reported in Refs. [Kal93, Sal01, Eld11, Nef11], where the strength of the g factor anisotropy depends on the potential asymmetry. For the two in-plane crystal directions [110] and [1$\bar{1}$0], a difference of 20% was found in Ref. [Nef11] for a GaAs-AlGaAs quantum well. In our experiments (cf. Fig. 4.20 and 4.22), we cannot clearly resolve such an anisotropy due to our experimental error margins. We will discuss this point in more detail in Sec. 4.6.2.

We saw that the model of vector addition between external and intrinsic fields is in good agreement with the single particle picture and therefore the experiments can be well described. With the here obtained parameters from the angular resolved measurements under the influence of an external magnetic field, we can in principle compute the maximum spin-orbit field. The energy paraboloids for spin up and down, shown in

Figs. 2.12 (b) and (d) are shifted towards each other by Δk (see Eq. (2.15)) for the case $\alpha = \pm\beta$. By plugging Eq. (2.15) into Eq. (2.31) and assuming the spin splitting to be Zeeman-type ($\Delta E_S = g\mu_B B_{\mathrm{SO}}$), the magnitude of the maximum intrinsic spin-orbit field is described by

$$B_{\mathrm{SO}} = \frac{4\alpha k_F}{g\mu_B} \tag{4.6}$$

When we insert our extracted parameters from the above shown measurements, we receive for sample A: $B_{\mathrm{SO}} \sim (19.9 \pm 4.1)\,\mathrm{T}$ and for sample B: $B_{\mathrm{SO}} \sim (18.6 \pm 3.9)\,\mathrm{T}$. The errors are quite high, since the external magnetic field was fixed in the above shown measurements, allowing to extract only a rather unprecise value of the g factor. Furthermore, this procedure is also prone to be influenced by sample inhomogeneities, because a stable measurement spot can not be guaranteed while rotating the sample. In the following section, we will demonstrate a more accurate method to verify the here determined intrinsic spin-orbit field values.

4.6.2 Determining the intrinsic effective spin-orbit field strength

In this section, we will demonstrate how an accurate determination of the maximum field strength of the intrinsic spin-orbit field can be achieved for sample A and B. This is done by fixing the wave-vector transfer $\boldsymbol{q}$ into the maximum spin splitting direction for each sample, i.e., [110] for sample A and $[1\bar{1}0]$ for sample B. In backscattering geometry, the external magnetic field points parallel or antiparallel to the maximum intrinsic spin-orbit field $\boldsymbol{B}_{\mathrm{SO}}$, since $\boldsymbol{B}_{\mathrm{ext}} \perp \boldsymbol{q}$ (see Fig. 3.3 (a)). This allows us to directly superimpose $\boldsymbol{B}_{\mathrm{SO}}$ with the external magnetic field $\boldsymbol{B}_{\mathrm{ext}}$ [Wal12b]. With this method, the laser position is kept fixed and uncertainties due to sample inhomogeneities, as discussed in the previous section, are reduced.

Depolarized RILS spectra for both samples are recorded for different external magnetic fields, ranging from $-6\,\mathrm{T}$ to $+6\,\mathrm{T}$, shown in Fig. 4.23 (a) and (b). A wave-vector transfer along maximum spin splitting direction with $\boldsymbol{q} \parallel [110]$ ($\varphi = 90°$) for sample A, and $\boldsymbol{q} \parallel [1\bar{1}0]$ ($\varphi = 0°$) for sample B is realized. In both spectra we clearly see a linear convergence of the spin splitting from positive to negative external magnetic fields. We assume the intrinsic spin-orbit field to be enhanced for $\boldsymbol{B}_{\mathrm{ext}}$ pointing parallel to $\boldsymbol{B}_{\mathrm{SO}}$ ($B_{\mathrm{ext}} > 0\,\mathrm{T}$) and attenuated for antiparallel orientation ($B_{\mathrm{ext}} < 0\,\mathrm{T}$). In direct comparison, we see that the energetic position of the SDE peaks for sample B is higher than for sample A. This is on the one hand due to the higher electron density of sample B

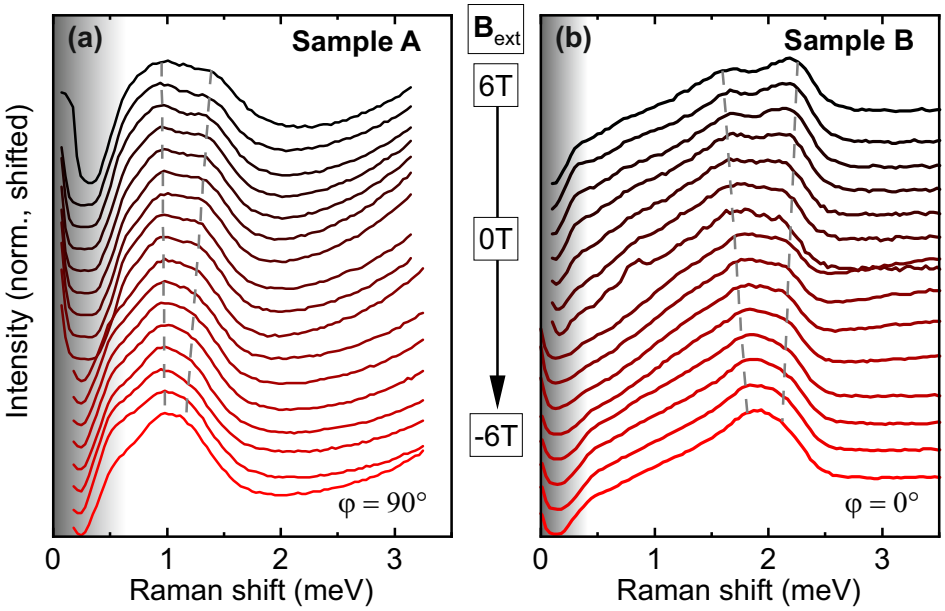

Figure 4.23 | (a) Depolarized RILS spectra of sample A for a set of different external magnetic fields, oriented parallel towards $\boldsymbol{B}_{\mathrm{SO}}$ for $B_{\mathrm{ext}} > 0\,\mathrm{T}$ and antiparallel for $B_{\mathrm{ext}} < 0\,\mathrm{T}$. A linear convergence of the spin splittings due to a superposition of $\boldsymbol{B}_{\mathrm{ext}}$ and $\boldsymbol{B}_{\mathrm{SO}}$ is observable. (b) Same as (a), but for sample B

(see Sec. 2.4.1). On the other hand, for sample B, a higher wave-vector transfer was realized, also increasing the energetic position of the SDE cutoff (cf. [Sch14]).
For both samples, the peak splittings were extracted via the Lindhard-Mermin lineshape analysis, and plotted against the applied external magnetic field in Fig. 4.24. The orange shaded area marks the accessible magnetic field range of our cryostat. In this area, we observe a linear shift of the measured peak splittings, which are clearly separated for both samples. At $B_{\mathrm{ext}} = 0\,\mathrm{T}$, the peak splitting of sample B is in good agreement with the calculated values for $\varphi = 0°$ and 180° (see Fig. 4.22), which confirms the above-derived values for α and β. This result also supports the presumption, that the angle resolved measurements may have been influenced by sample inhomogeneities. We extract the strength of the intrinsic spin-orbit field $\boldsymbol{B}_{\mathrm{SO}}$ by extrapolating the spin splittings (dashed lines) until their intersection with the x axis. For both samples we receive a value of $\sim(18 \pm 1)\,\mathrm{T}$, which is in good agreement with the previously computed values (see Eq. (4.6)). The effective $|g|$ factors can be derived from the slopes of the dashed lines: For sample A we extract 0.17 ± 0.01, and for sample B 0.24 ± 0.01, which is in almost perfect agreement with the values determined from angular-resolved measurements with fixed magnetic field (gray dashed lines in Figs. 4.20 and 4.22).
All experimentally determined parameters are summarized in table 2.1. We assume that the approximate equivalence of the spin-orbit parameters for sample A and B is

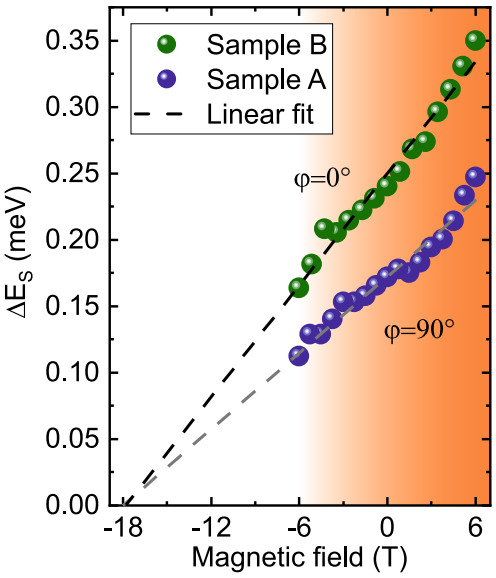

Figure 4.24 | Spin splittings for both investigated samples, extracted via Lindhard-Mermin lineshape analysis with a wavevector transfer along maximum spin splitting crystal direction. The experimentally accessible magnetic field range of the cryostat is shaded orange. Dashed line: Linear fit and extrapolation of the spin splittings.

just by coincidence. The different doping profiles seems to result in approximately the same magnitude of the Bychkov-Rashba coefficient $|\alpha|$ in both samples. The obvious difference of the g factors, extracted from Fig. 4.24 is, however, unclear. Sample B, which has the larger electron density n, shows a g factor, almost 50% larger than the g factor of sample A. For a quantum well width of 12 nm, one would expect a negative g factor [Le 97, Mal00], and $|g|$ is supposed to decrease with increasing Fermi energy (and same well width).

At this point it should be stressed, that the difference in g factors does not originate from an in-plane g factor anisotropy, which is reported in Refs. [Kal93, Eld11, Nef11]. In Ref. [Nef11], a maximum anisotropy of the g factor was found for [110] and [1$\bar{1}$0] crystal direction in a GaAs-AlGaAs heterojunction. These are the directions of maximum spin splitting in our experimental findings for sample A and B respectively (cf. Fig. 4.20 and 4.22). However, since the electric field is reversed, comparing sample A with sample B, the in-plane direction of the maximum and minimum g factors should also be interchanged. This will be discussed in the following: The nondiagonal elements of the in-plane g tensor can be expressed as [Kal93, Eld11]

$$g_{xy} = g_{yx} = \frac{2\gamma e}{\hbar^3 \mu_B} \left(\langle p_z^2 \rangle \langle z \rangle - \langle p_z^2 z \rangle \right). \tag{4.7}$$

γ is the bulk Dresselhaus coefficient [Dre55] and $\langle\rangle$ indicates the expectation value for the electron wave function. For a symmetric quantum-well potential, the expression $\langle p_z^2 \rangle \langle z \rangle - \langle p_z^2 z \rangle$ vanishes and an isotropic g factor is obtained. The asymmetry of the potential scales with the magnitude of the offdiagonal element g_{xy}, i.e., larger asym-

metry leading to a larger magnitude of the offdiagonal element. From the electronic wave functions of sample A and B (cf. Figs. 2.5 (c) and 2.6 (c)) and Eq. (4.7) it follows that $g_{xy} > 0$ for sample A and $g_{xy} < 0$ for sample B, provided that $\gamma > 0$. In our experiments, the external magnetic field $\boldsymbol{B}_{\mathrm{ext}}$ is small compared to the intrinsic field $B_{\mathrm{SO}} \sim 18\,\mathrm{T}$, and points in arbitrary in-plane directions φ, as defined above. For this case, $g(\varphi)$ can be written as [Eld11]

$$g(\varphi) = -\sqrt{g_{xx}^2 + g_{xy}^2 + 2g_{xx}g_{xy}\cos(2\varphi)}. \tag{4.8}$$

We must consider that in our backscattering experiments we have $\boldsymbol{B}_{\mathrm{ext}} \perp \boldsymbol{q}$, meaning that, for a wave-vector transfer along the maximum spin splitting direction, e.g., in sample A, $\boldsymbol{q} \parallel [110]$, $\boldsymbol{B}_{\mathrm{ext}} \parallel [1\bar{1}0]$, and so on. By employing Eq. (4.8), we receive the following relations: $|g_{110}| = |g(180°)| > |g_{1\bar{1}0}| = |g(-90°)|$ for sample A and $|g_{1\bar{1}0}| = |g(-90°)| > |g_{110}| = |g(180°)|$ for sample B. With this we can confirm that a maximum in-plane g factor is present in the direction of maximum spin splitting, i.e., [110] for sample A and $[1\bar{1}0]$ for sample B. Consequently, the significant difference of the measured g factors cannot be explained by the g factor anisotropy.
It is unclear if the difference in g factors can be explained by residual collective effects in the Landau-damped SDE, leading to an enhancement of the spin-orbit field and, hence, an increased spin splitting. In experiments from Baboux et al. [Bab12], an amplification of the intrinsic spin-orbit field - due to collective effects - up to a factor of five was reported on the basis of RILS experiments on intersubband SDEs in GaAs-AlGaAs quantum wells. This was also confirmed in studies on intrasubband SDEs in a CdMnTe quantum well [Bab13]. For the situation in Fig. 4.24, where $\boldsymbol{B}_{\mathrm{ext}}$ is parallel to $\boldsymbol{B}_{\mathrm{SO}}$, we can rewrite Eq. (2.31) for a Zeeman-like energy splitting as follows

$$\Delta E_{S,max} = 2(|\alpha| + \beta)k_F + g\mu_B B_{\mathrm{ext}} = g\mu_B \left[B_{\mathrm{so}} + B_{\mathrm{ext}}\right]. \tag{4.9}$$

The effect of a collective spin-orbit field may be modeled by Eq. (4.9), containing g as an effective g factor. At this point we cannot say if a possible many-particle interaction effect influences just the g factor or the spin-orbit field.
We found approximately the same magnitude of the intrinsic spin-orbit field B_{SO} for both samples A and B, and can conclude from Eq. (4.6), that the relation k_F/g has to be the same both samples. In our case, the larger k_F (sample B) is compensated by a larger g factor and vice versa. Whether this behavior is significant or coincidental requires more experimental and theoretical investigations.

Chapter 5

Conclusion

In this work a new measurement setup was developed, in which the spin-orbit interaction in 2DES in GaAs-AlGaAs single quantum wells was investigated. Object of research was the analysis of samples where the condition for the PSH is realized. In these highly specialized samples, the PSH condition is present in two different configurations. In particular, the two [001]-grown samples differ in the sign of the Bychkov-Rashba parameter, which results in a different orientation of the intrinsic effective spin-orbit field. The main goal of this work was to perform and analyze RILS experiments on intrasubband SDE. By transferring an in-plane wave vector $\boldsymbol{q}$ into the 2DES plane, RILS experiments allow the measurement of the spin splitting at the Fermi energy in dependence of the in-plane crystal direction. For the experiments in a split-coil magnetocryostat a special sample holder was constructed, enabling different configurations of the magnetic field with respect to $\boldsymbol{q}$, associated with the RILS experiments. In addition, a sample rotator allows in-situ sample rotation, for realizing transfer of $\boldsymbol{q}$ in arbitrary crystal directions. The interpretation of the obtained spectra from the RILS experiments is supported by a numerical line-shape analysis, which allows to determine important spin-orbit field parameters of the samples, the electron $|g|$ factor and the single-particle scattering time.

The experimental results start with basic characterization measurements of the used samples. By tuning the laser excitation wavelength, the best SDE resonance conditions for all investigated samples was determined. This is followed by an estimation of the excitation-dependent temperature of the 2DES, utilizing the Fermi edge in photoluminescence spectra. For realistic measurement conditions, an electron temperature of $T \approx 12\,\mathrm{K}$ was extracted, confirming the result of the numerical line-shape analysis,

where best simulation results are obtained for comparable temperatures.
Using a semitransparent electrical top gate and the 2DES as a back gate contact, it was shown that the charge carrier density inside the 2DES can effectively be changed. It has been demonstrated, that the charge carrier density can be reduced by a factor of 5, until the excitonic regime is reached. Furthermore, the electrical gate was intended to manipulate the strength of the Bychkov-Rashba spin-orbit field parameter $|\alpha|$. By performing gate voltage sweeps, we were able to detect a change of $|\alpha|$.

In the presence of external magnetic fields, perpendicular to the 2DES, we observed the smooth transition of a translationally invariant 2DES (in which the transferred quasi-momentum $\boldsymbol{q}$ is still a good quantum number) into a completely Landau-quantized system. For moderate magnetic fields, from the circulation period of the cyclotron resonances, a single-particle scattering time of $\tau_{\mathrm{sp}} = 2.8\,\mathrm{ps}$ is estimated. This confirms the independently determined value from the numerical line-shape analysis simulation. Also the effective electron mass, playing an important role in the line-shape analysis, was extracted from the cyclotron resonances. At small external magnetic fields, $\boldsymbol{q}$ is a good quantum number, allowing the observation of intrasubband SDE. It is remarkable that we found the energetic positions of the SDE maxima to decrease with increasing magnetic field. It remains to be investigated whether this decrease is due to the exchange interaction of the electrons, which in principle should influence the energy of a collective SDE. Such a collective effect was predicted in Ref. [Ull03]. For intersubband transitions, an enhancement of the collective spin-orbit field by a factor of 5, compared to the SO-field of a non-interacting system was reported in Ref. [Bab12].

The main focus in this work was the investigation of the intrasubband SDE spin splitting and its angular dependence of the in-plane crystal direction. For both samples we could demonstrate an extreme anisotropy of the measured spin splitting caused by the spin-orbit field corresponding to the PSH. Furthermore, external in-plane magnetic fields parallel to the 2DES were applied, which vectorially add to the spin-orbit fields. This allows a direct quantitative determination of the intrinsic spin-orbit fields, for which a maximum strength of 18 T was found for the two samples. Furthermore, the effective $|g|$ factors of both samples were determined and found to differ by almost 50%. Contrary to initial expectations, the sample with the higher Fermi energy has the smaller $|g|$ factor, which might be explained by residual collective effects in the Landau-damped SDE. The comparable spin-orbit field strengths in both samples leads to the assumption that a larger Fermi wave vector k_F (dependent on the charge carrier

density) is compensated by a larger $|g|$ factor. A strong motivation for the future is to find out whether this is significant or just by coincidence. One possible approach would be a systematic investigation of samples equipped with an electric gate to tune the charge carrier density (and thus k_F) inside the 2DES. As a result it could be determined whether there is a compensating behavior of the $|g|$ factor, as addressed above.

A further promising possibility for the future would be to detect the PSH state via the spin splitting of the intrasubband SDE in symmetrical [110]-grown GaAs-AlGaAs quantum wells, which has not yet been demonstrated with this method. Since the spin-orbit field for this case is oriented perpendicular to the 2DES plane, it can be shown, that spinflip intrasubband SDE are only allowed in grazing incidence measurement geometry, where the laser is pointing on a cleaved edge of the prepared sample. We found, that the signal yield of a single quantum well is not sufficient to detect the spin splitting in the SDE spectra. By using symmetrical [110]-grown multi-quantum well samples, this effect might possibly be revealed.

Bibliography

[Ada85] S. Adachi, *GaAs, AlAs, and AlGaAs: Material parameters for use in research and device applications*, Journal of Applied Physics **58** (1985).

[Ahr93] R. Ahrenkiel and M. Ludstrom, *Minority-carrier lifetime in III-V semiconductors*, Semiconductors and semimetals, Academic Press, Inc. (1993).

[And62] R. L. Anderson, *Experiments on Ge-GaAs Heterojunctions*, Solid-State Electronics **5**, 341 (1962).

[Bab12] F. Baboux, F. Perez, C. A. Ullrich, I. D'Amico, J. Gómez, and M. Bernard, *Giant collective spin-orbit field in a quantum well: Fine structure of spin plasmons*, Phys. Rev. Lett. **109**, 166401 (2012).

[Bab13] F. Baboux, F. Perez, C. A. Ullrich, I. D'Amico, G. Karczewski, and T. Wojtowicz, *Coulomb-driven organization and enhancement of spin-orbit fields in collective spin excitations*, Phys. Rev. B **87**, 121303 (2013).

[Bai88] M. N. Baibich, J. M. Broto, A. Fert, F. N. Van Dau, F. Petroff, P. Eitenne, G. Creuzet, A. Friederich, and J. Chazelas, *Giant magnetoresistance of (001)Fe/(001)Cr magnetic superlattices*, Phys. Rev. Lett. **61**, 2472 (1988).

[Bar48] J. Bardeen and W. H. Brattain, *The transistor, a semiconductor triode*, Phys. Rev. **74**, 230 (1948).

[Ber90] M. Berz, J. F. Walker, P. Von Allmen, E. F. Steigmeier, and F. K. Reinhart, *Strong intermediate-state effects in exciton-mediated electronic intrasubband scattering in multiple-quantum-well structures*, Phys. Rev. B **42**, 11957 (1990).

[Ber06] B. A. Bernevig, J. Orenstein, and S.-C. Zhang, *Exact SU(2) symmetry and persistent spin helix in a spin-orbit coupled system*, Phys. Rev. Lett. **97**, 236601 (2006).

[Bin89] G. Binasch, P. Grünberg, F. Saurenbach, and W. Zinn, *Enhanced magnetoresistance in layered magnetic structures with antiferromagnetic interlayer exchange*, Phys. Rev. B **39**, 4828 (1989).

[Bir07] S. Birner, T. Zibold, T. Andlauer, T. Kubis, M. Sabathil, A. Trellakis, and P. Vogl, *Nextnano: General purpose 3-D simulations*, IEEE Transactions on Electron Devices **54**, 2137 (2007).

[Blu70] F. A. Blum, *Inelastic light scattering from semiconductor plasmas in a magnetic field*, Phys. Rev. B **1**, 1125 (1970).

[Bru94] K. Brunner, G. Abstreiter, G. Böhm, G. Tränkle, and G. Weimann, *Sharp-line photoluminescence of excitons localized at GaAs/AlGaAs quantum well inhomogeneities*, Appl. Phys. Lett. **64**, 3320 (1994).

[Bur80] E. Burstein, A. Pinczuk, and D. L. Mills, *Inelastic light scattering by charge carrier excitations in two-dimensional plasmas: Theoretical considerations*, Surf. Sci. **98**, 451 (1980).

[Byc84a] Y. A. Bychkov and E. I. Rashba, *Oscillatory effects and the magnetic susceptibility of carriers in inversion layers*, Journal of Physics C: Solid State Physics **17**, 6039 (1984).

[Byc84b] Y. A. Bychkov and E. I. Rashba, *Properties of a 2D electron gas with lifted spectral degeneracy*, JETP Lett. **39**, 78 (1984).

[Cha86] A. Chaves, A. Penna, and J. M. Worlock, *Optical control of two-dimensional electron density in a single asymmetric quantum well*, Surf. Sci. **170**, 618 (1986).

[Che76] J. R. Chelikowsky and M. L. Cohen, *Nonlocal pseudopotential calculations for the electronic structure of eleven diamond and zinc-blende semiconductors*, Phys. Rev. B **14**, 556 (1976).

[Che14] Y. S. Chen, S. Fält, W. Wegscheider, and G. Salis, *Unidirectional spin-orbit interaction and spin-helix state in a (110)-oriented GaAs/(Al,Ga)As quantum well*, Phys. Rev. B **90**, 121304 (2014).

[Dan89] G. Danan, A. Pinczuk, J. P. Valladares, L. N. Pfeiffer, K. W. West, and C. W. Tu, *Coupling of excitons with free electrons in light scattering from GaAs quantum wells*, Phys. Rev. B **39**, 5512 (1989).

[Das90] S. Das Sarma, R. Jalabert, and S.-R. Yang, *Band-gap renormalization in semiconductor quantum wells*, Phys. Rev. B **41**, 8288 (1990).

[Dat90] S. Datta and B. Das, *Electronic analog of the electro-optic modulator*, Appl. Phys. Lett. **56**, 665 (1990).

[Dav97] J. H. Davies, *The Physics of Low-dimensional Semiconductors: An Introduction*, Cambridge University Press (1997).

[Dre55] G. Dresselhaus, *Spin-orbit coupling effects in zinc blende structures*, Phys. Rev. **100**, 580 (1955).

[Dya71] M. I. Dyakonov and V. I. Perel, *Spin orientation of electrons associated with the interband absorption of light in semiconductors*, JETP Lett. **33**, 1053 (1971).

[Dya86] M. I. Dyakonov and V. Y. Kachorovskii, *Spin relaxation of two-dimensional electrons in non-centrosymmetric semiconductors*, Sov. Phys. Semicond. **20**, 110 (1986).

[Dya08] M. I. Dyakonov, *Spin physics in semiconductors*, Springer, Berlin (2008).

[Eke89] U. Ekenberg, *Nonparabolicity effects in a quantum well: sublevel shift, parallel mass, and Landau levels*, Phys. Rev. B **40**, 7714 (1989).

[Eld11] P. S. Eldridge, J. Hübner, S. Oertel, R. T. Harley, M. Henini, and M. Oestreich, *Spin-orbit fields in asymmetric (001)-oriented GaAs/AlGaAs quantum wells*, Phys. Rev. B **83**, 041301 (2011).

[Esi87] E. Esipov and Y. B. Levinson, *The temperature and energy distribution of photoexcited hot electrons*, Advances in Physics **36**, 331 (1987).

[Fab07] J. Fabian, A. Matos-Abiague, C. Ertler, P. Stano, and I. Žutić, *Semiconductor spintronics*, Acta Physica Slovaca **57**, 565 (2007).

[Fas87] G. Fasol, N. Mestres, A. Fischer, and K. Ploog, *Coupled plasmons and single particle excitations in the two-dimensional electron gas*, Physica Scripta **T19**, 109 (1987).

[Fol93] P. Folkes, M. Dutta, S. Rudin, H. Shen, W. Zhou, D. Smith, M. Taysing-Lara, P. Newman, and M. Cole, *Excitonic recombination of degenerate two-dimensional electrons with localized photoexcited holes in a single hetero-junction quantum well*, Phys. Rev. Lett. **71**, 3379 (1993).

[Fra17] C. Frankerl, *Experimental Raman spectroscopy and theoretical modeling of spin-density excitations in GaAs/AlGaAs quantum wells*, Master's thesis, Universität Regensburg (2017).

[Gam90] D. Gammon, B. V. Shanabrook, J. C. Ryan, and D. S. Katzer, *Spin-density waves in a quasi-two-dimensional electron gas*, Phys. Rev. B **41**, 311 (1990).

[Gam92a] D. Gammon, B. V. Shanabrook, J. C. Ryan, G. Brozak, and D. S. Katzer, *Exchange and correlation in quasi-two-dimensional plasmas in quantum well structures*, Surf. Sci. **263**, 471 (1992).

[Gam92b] D. Gammon, B. V. Shanabrook, J. C. Ryan, D. S. Katzer, and M. J. Yang, *Exchange and correlation in the nonhomogeneous electron gas in semiconductor heterojunctions*, Phys. Rev. Lett. **68**, 1884 (1992).

[Gan04] S. D. Ganichev, V. V. Bel'kov, L. E. Golub, E. L. Ivchenko, P. Schneider, S. Giglberger, J. Eroms, J. De Boeck, G. Borghs, W. Wegscheider, D. Weiss, and W. Prettl, *Experimental separation of Rashba and Dresselhaus spin splittings in semiconductor quantum wells*, Phys. Rev. Lett. **92**, 256601 (2004).

[Gel18] S. Gelfert, C. Frankerl, C. Reichl, D. Schuh, G. Salis, W. Wegscheider, D. Bougeard, T. Korn, and C. Schüller, *Magneto-Raman spectroscopy of spin-density excitations in (001)-grown GaAs-AlGaAs quantum wells in the regime of the persistent spin helix*, Spintronics XI, Proceedings of SPIE **10732** (2018).

[Gel20] S. Gelfert, C. Frankerl, C. Reichl, D. Schuh, G. Salis, W. Wegscheider, D. Bougeard, T. Korn, and C. Schüller, *Inelastic light scattering by intra-subband spin-density excitations in GaAs-AlGaAs quantum wells with balanced Bychkov-Rashba and Dresselhaus spin-orbit interaction: Quantitative determination of the spin-orbit field*, Phys. Rev. B **101**, 035427 (2020).

[Gov97] A. O. Govorov, *Resonant light scattering induced by Coulomb interaction*

in semiconductor microstructures, Journal of Physics: Condensed Matter **9**, 4681 (1997).

[Gra17] C. Gradl, *Anisotrope Lochspindynamik in GaAs/AlAs- Quantentrogstrukturen*, Dissertation, Universität Regensburg (2017).

[Gri12] M. Griesbeck, *Spin dynamics in high-mobility two-dimensional electron systems embedded in GaAs/AlGaAs quantum wells*, Dissertation, Universität Regensburg (2012).

[Haa92] S. Haacke, R. Zimmermann, D. Bimberg, H. Kal, D. E. Mars, and J. N. Miller, *Fermi enhancement and band-gap renormalization of AlGaAs/GaAs modulation-doped quantum wells*, Phys. Rev. B **45**, 1736 (1992).

[Ham69] D. C. Hamilton and A. L. McWhorter, *Light Scattering Spectra of Solids*, Springer, New York (1969).

[Has97] T. Hassenkam, S. Pedersen, K. Baklanov, A. Kristensen, C. B. Sorensen, P. E. Lindelof, F. G. Pikus, and G. E. Pikus, *Spin splitting and weak localization in (110) GaAs/$Al_xGa_{1-x}As$ quantum wells*, Phys. Rev. B **55**, 9298 (1997).

[Hir12] M. Hirmer, *Elektronische Raman-Streuung und die Spin-Bahn-Wechselwirkung in p-dotierten GaAs/AlGaAs Quantentrögen*, Dissertation, Universität Regensburg (2012).

[Ihn10] T. Ihn, *Semiconductor Nanostructures: Quantum States and Electronic Transport*, Oxford University Press (2010).

[Ish14] J. Ishihara, Y. Ohno, and H. Ohno, *Direct imaging of gate-controlled persistent spin helix state in a modulation-doped GaAs/AlGaAs quantum well*, Applied Physics Express **7**, 013001 (2014).

[Jus92] B. Jusserand, D. Richards, H. Peric, and B. Etienne, *Zero-magnetic-field spin splitting in the GaAs conduction band from Raman scattering on modulation-doped quantum wells*, Phys. Rev. Lett. **69**, 848 (1992).

[Jus95] B. Jusserand, D. Richards, G. Allan, C. Priester, and B. Etienne, *Spin orientation at semiconductor heterointerfaces*, Phys. Rev. B **51**, 4707 (1995).

[Jus00] B. Jusserand, M. N. Vijayaraghavan, F. Laruelle, A. Cavanna, and B. Etienne, *Resonant mechanisms of inelastic light scattering by low-dimensional electron gases*, Phys. Rev. Lett. **85**, 5400 (2000).

[Jus03] B. Jusserand, M. El Kurdi, and A. Cavanna, *Wave vector dependent inter-Landau-level transitions in modulation-doped quantum wells*, Phys. Rev. B **67**, 233307 (2003).

[Kal93] V. K. Kalevich and V. L. Korenev, *Electron g-factor anisotropy in asymmetric GaAs/AlGaAs quantum well*, JETP Lett. **57**, 571 (1993).

[Kam16] M. Kammermeier, P. Wenk, and J. Schliemann, *Control of spin helix symmetry in semiconductor quantum wells by crystal orientation*, Phys. Rev. Lett. **117**, 236801 (2016).

[Kau00] R. Kaur, A. J. Shields, J. L. Osborne, M. Y. Simmons, D. A. Ritchie, and M. Pepper, *Electron density dependence of the excitonic absorption thresholds of GaAs quantum wells*, Physica Status Solidi (A) Applied Research **178**, 465 (2000).

[Kil63] J. S. Kilby, *Miniature semiconducor integrated circuit*, US Patent 3115581 (1963).

[Kil76] J. S. Kilby, *Invention of the integrated circuit*, IEEE Transactions on Electron Devices **23** (1976).

[Kit63] C. Kittel and C.-Y. Fong, *Quantum theory of solids*, Wiley, New York **5** (1963).

[Kle85] D. A. Kleinman and R. C. Miller, *Band-gap renormalization in semiconductor quantum wells containing carriers*, Phys. Rev. B **32**, 2266 (1985).

[Koh12] M. Kohda, V. Lechner, Y. Kunihashi, T. Dollinger, P. Olbrich, C. Schönhuber, I. Caspers, V. V. Bel'kov, L. E. Golub, D. Weiss, K. Richter, J. Nitta, and S. D. Ganichev, *Gate-controlled persistent spin helix state in (In,Ga)As quantum wells*, Phys. Rev. B **86**, 081306 (2012).

[Koo09] H. C. Koo, J. H. Kwon, J. Eom, J. Chang, S. H. Han, and M. Johnson, *Control of spin precession in a spin-injected field effect transistor*, Science **325**, 1515 (2009).

[Kor09] J. D. Koralek, C. P. Weber, J. Orenstein, B. A. Bernevig, S.-C. Zhang, S. Mack, and D. D. Awschalom, *Emergence of the persistent spin helix in semiconductor quantum wells*, Nature **458**, 610 (2009).

[Kre96] O. Krebs and P. Voisin, *Giant optical anisotropy of semiconductor heterostructures with no common atom and the quantum-confined pockels effect*, Phys. Rev. Lett. **77**, 1829 (1996).

[Kug12] M. Kugler, *Lochspindynamik in p-dotierten GaAs/AlGaAs-Heterostrukturen*, Dissertation, Universität Regensburg (2012).

[Lan46] L. Landau, *On the vibrations of the electronic plasma*, Journal of Physics (USSR) **10**, 25 (1946).

[Le 97] P. Le Jeune, D. Robart, X. Marie, T. Amand, M. Brousseau, J. Barrau, V. Kalevich, and D. Rodichev, *Anisotropy of the electron Landé g factor in quantum wells*, Semicond. Sci. Technol. **12**, 380 (1997).

[Lin54] J. Lindhard, *On the properties of a gas of charged particles*, Danske Matematisk-fysiske Meddelelser. Det Kongelige Danske Videnskabernes Selskab **28**, 1 (1954).

[Maa84] J. C. Maan, G. Belle, A. Fasolino, M. Altarelli, and K. Ploog, *Magneto-optical determination of exciton binding energy in GaAs-GaAlAs quantum wells*, Phys. Rev. B **30**, 2253 (1984).

[Mal97] A. G. Mal'shukov, K. A. Chao, and M. Willander, *Magnetoresistance of a weakly disordered III-V semiconductor quantum well in a magnetic field parallel to interfaces*, Phys. Rev. B **56**, 6436 (1997).

[Mal00] A. Malinowski and R. Harley, *Anisotropy of the electron g factor in lattice-matched and strained-layer III-V quantum wells*, Phys. Rev. B **62**, 2051 (2000).

[Mar83] V. A. Marushchak, M. N. Stepanova, and A. N. Titkov, *Spin relaxation of conduction electrons in moderately doped gallium arsenide crystals*, Sov. Phys. Solid State **25**, 2035 (1983).

[Men86] J. Menéndez, A. Pinczuk, D. J. Werder, A. C. Gossard, and J. H. English, *Light scattering determination of band offsets in GaAs-AlGaAs quantum wells*, Phys. Rev. B **33**, 8863 (1986).

[Mer70] N. D. Mermin, *Lindhard dielectric function in the relaxation-time approximation*, Phys. Rev. B **1**, 2362 (1970).

[Mil03] J. B. Miller, D. M. Zumbühl, C. M. Marcus, Y. B. Lyanda-Geller, D. Goldhaber-Gordon, K. Campman, and A. C. Gossard, *Gate-controlled spin-orbit quantum interference effects in lateral transport*, Phys. Rev. Lett. **90**, 768071 (2003).

[Nef11] Y. A. Nefyodov, A. V. Shchepetilnikov, I. V. Kukushkin, W. Dietsche, and S. Schmult, *Electron g-factor anisotropy in GaAs/AlGaAs quantum wells of different symmetry*, Phys. Rev. B **84**, 233302 (2011).

[Nit97] J. Nitta, T. Akazaki, H. Takayanagi, and T. Enoki, *Gate control of spin-orbit interaction in an inverted* $In_{0.53}Ga_{50.47}As/In_{0.52}Al_{0.48}As$ *heterostructure*, Phys. Rev. Lett. **78**, 1335 (1997).

[Nur93] A. Nurmikko and A. Pinczuk, *Optical probes in the quantum Hall regime*, Physics Today **46**, 24 (1993).

[Pea67] W. B. Pearson, *Handbook of Lattice Spacings and Structure of Metals and Alloys*, Pergamon, New York (1967).

[Pin88] A. Pinczuk and G. Abstreiter, *Spectroscopy of Free Carrier Excitations in Semiconductor Quantum Wells*, Springer, Heidelberg (1988).

[Pin89] A. Pinczuk, S. Schmitt-Rink, G. Danan, J. P. Valladares, L. N. Pfeiffer, and K. W. West, *Large exchange interactions in the electron gas of GaAs quantum wells*, Phys. Rev. Lett. **63**, 1633 (1989).

[Rab15] A. Rabenstein and C. Gorini, *Raman scattering on a two dimensional electron gas*, Project work within the "Forschungsstudiengang", Universität Regensburg (2015).

[Ram28] C. V. Raman, *A new radiation*, Indian J. Phys. **2**, 368 (1928).

[Ras60] E. I. Rashba, *Properties of semiconductors with an extremum loop. I. Cyclotron and combinational resonance in a magnetic field perpendicular to the plane of the loop*, Sov. Phys. Solid State **2**, 1109 (1960).

[Ric93] D. Richards, B. Jusserand, H. Peric, and B. Etienne, *Intrasubband excitations and spin-splitting anisotropy in GaAs modulation-doped quantum wells*, Phys. Rev. B **47**, 16028 (1993).

[Ric96] D. Richards, B. Jusserand, G. Allan, C. Priester, and B. Etienne, *Electron spin-flip Raman scattering in asymmetric quantum wells: Spin orientation*, Solid-State Electronics **40**, 127 (1996).

[Ruf90] T. Ruf and M. Cardona, *Nonparabolicity of the conduction band in GaAs*, Phys. Rev. B **41**, 10747 (1990).

[Sal01] G. Salis, D. D. Awschalom, Y. Ohno, and H. Ohno, *Origin of enhanced dynamic nuclear polarization and all-optical nuclear magnetic resonance in GaAs quantum wells*, Phys. Rev. B **64**, 195304 (2001).

[Sal14] G. Salis, M. P. Walser, P. Altmann, C. Reichl, and W. Wegscheider, *Dynamics of a localized spin excitation close to the spin-helix regime*, Phys. Rev. B **89**, 045304 (2014).

[Sar99] S. D. Sarma and D.-W. Wang, *Resonant Raman scattering by elementary electronic excitations in semiconductor structures*, Phys. Rev. Lett. **83**, 816 (1999).

[Sch97] C. Schüller, R. Krahne, G. Biese, C. Steinebach, E. Ulrichs, D. Heitmann, and K. Eberl, *Multiple cyclotron resonances in GaAs-AlGaAs quantum wells detected by resonant inelastic light scattering*, Phys. Rev. B **56**, 1037 (1997).

[Sch03] J. Schliemann, J. C. Egues, and D. Loss, *Nonballistic Spin-Field-Effect Transistor*, Phys. Rev. Lett. **90**, 146801 (2003).

[Sch04] F. Schwabl, *Quantenmechanik*, Springer, Berlin (2004).

[Sch06] C. Schüller, *Inelastic Light Scattering of Semiconductor Nanostructures*, Springer, Berlin (2006).

[Sch08] J. Schliemann, *Cyclotron motion and magnetic focusing in semiconductor quantum wells with spin-orbit coupling*, Phys. Rev. B **77**, 125303 (2008).

[Sch14] C. Schönhuber, M. P. Walser, G. Salis, C. Reichl, W. Wegscheider, T. Korn, and C. Schüller, *Inelastic light-scattering from spin-density excitations in the regime of the persistent spin helix in a GaAs-AlGaAs quantum well*, Phys. Rev. B **89**, 085406 (2014).

[Sch16a] C. Schönhuber, *Inelastic light scattering in the regime of the persistent spin helix*, Dissertation, Universität Regensburg (2016).

[Sch16b] M. Schwemmer, A. Hanninger, M. Weingartner, M. Oltscher, M. Ciorga, D. Weiss, D. Schuh, D. Bougeard, T. Korn, and C. Schüller, *Deterministic transfer of spin polarization in wire-like lateral structures via the persistent spin helix*, Appl. Phys. Lett. **109**, 172106 (2016).

[Shi95] A. J. Shields, M. Pepper, D. A. Ritchie, M. Y. Simmons, and G. A. Jones, *Quenching of excitonic optical transitions by excess electrons in GaAs quantum wells*, Phys. Rev. B **51**, 18049 (1995).

[Skr84] B. J. Skromme and G. E. Stillman, *Excited-state-donor-to-acceptor transitions in the photoluminescence spectrum of GaAs and InP*, Phys. Rev. B **29**, 1982 (1984).

[Ste67] F. Stern, *Polarizability of a two-dimensional electron gas*, Phys. Rev. Lett. **18**, 546 (1967).

[Stu09] M. Studer, G. Salis, K. Ensslin, D. C. Driscoll, and A. C. Gossard, *Gate-controlled spin-orbit interaction in a parabolic GaAs/AlGaAs quantum well*, Phys. Rev. Lett. **103**, 027201 (2009).

[Sze07] S. M. Sze, *Physics of Semiconductor Devices*, Wiley-Interscience, Hoboken (2007).

[Tho06] S. E. Thompson and S. Parthasarathy, *Moore's law: the future of Si microelectronics*, Materials Today **9**, 20 (2006).

[Tre06] A. Trellakis, T. Zibold, T. Andlauer, S. Birner, R. K. Smith, R. Morschl, and P. Vogl, *The 3D nanometer device project nextnano: Concepts, methods, results*, Journal of Computational Electronics **5**, 285 (2006).

[Ull03] C. A. Ullrich and M. E. Flatté, *Anisotropic splitting of intersubband spin plasmons in quantum wells with bulk and structural inversion asymmetry*, Phys. Rev. B **68**, 235310 (2003).

[Uma09] V. Umansky, M. Heiblum, Y. Levinson, J. Smet, J. Nübler, and M. Dolev, *MBE growth of ultra-low disorder 2DEG with mobility exceeding* 35×10^6 $cm^2/V\,s$, Journal of Crystal Growth **311**, 1658 (2009).

[Wal12a] M. P. Walser, C. Reichl, W. Wegscheider, and G. Salis, *Direct mapping of the formation of a persistent spin helix*, Nature Physics **8**, 757 (2012).

[Wal12b] M. P. Walser, U. Siegenthaler, V. Lechner, D. Schuh, S. D. Ganichev, W. Wegscheider, and G. Salis, *Dependence of the Dresselhaus spin-orbit interaction on the quantum well width*, Phys. Rev. B **86**, 4 (2012).

[Wen88] L. Wendler, *Landau damped collective excitations of the quasi-two-dimensional polaron gas in double heterostructures*, Solid State Commun. **65**, 1197 (1988).

[Win03] R. Winkler, *Spin Orbit Coupling Effects in Two-Dimensional Electron and Hole Systems*, Springer, Berlin (2003).

[Win04] R. Winkler and M. Oestreich, *Spinelektronik*, in *Physik Journal*, Nr. 11, WILEY-VCH Verlag (2004).

[Wor83] J. M. Worlock, *Wave vector dependent magneto-optical interband transitions in semiconductors*, Solid State Commun. **48**, 1067 (1983).

[Yu91] H. Yu and J. C. Hermanson, *Collective electronic excitations in GaAs/AlGaAs quantum wells*, Phys. Rev. B **43**, 4340 (1991).

[Yu96] P. Y. Yu and M. Cardona, *Fundamentals of Semiconductors*, Springer, Berlin (1996).

[Yug07] I. A. Yugova, A. Greilich, D. R. Yakovlev, A. A. Kiselev, M. Bayer, V. V. Petrov, Y. K. Dolgikh, D. Reuter, and A. D. Wieck, *Universal behavior of the electron g factor in GaAs/AlGaAs quantum wells*, Phys. Rev. B **75**, 245302 (2007).

[Zee97] P. Zeeman, *The effect of magnetisation on the nature of light emitted by a substance*, Nature **55**, 347 (1897).

[Žut04] I. Žutić, J. Fabian, and S. Das Sarma, *Spintronics: Fundamentals and applications*, Reviews of Modern Physics **76**, 323 (2004).

List of publications

S. Gelfert, C. Frankerl, C. Reichl, D. Schuh, G. Salis, W. Wegscheider, D. Bougeard, T. Korn, and C. Schüller, *Inelastic light scattering by intrasubband spin-density excitations in GaAs-AlGaAs quantum wells with balanced Bychkov-Rashba and Dresselhaus spin-orbit interaction: Quantitative determination of the spin-orbit field,* Phys. Rev. B **101**, 035427 (2020). Awarded as Editors' Suggestion.

S. Gelfert, C. Frankerl, C. Reichl, D. Schuh, G. Salis, W. Wegscheider, D. Bougeard, T. Korn, and C. Schüller, *Magneto-Raman spectroscopy of spin-density excitations in (001)-grown GaAs-AlGaAs quantum wells in the regime of the persistent spin helix,* Spintronics XI, Proceedings of SPIE **10732** (2018).

Conference contributions and invited talks

IBM-Research Zurich invited by Dr. Gian Salis, Rüschlikon, Switzerland: Invited talk (2019).

ETH Zürich invited by Prof. Werner Wegscheider, Zürich, Switzerland: Invited talk (2019).

SPIE Optics + Photonics 2018, San Diego, United States: Invited talk (2018).

ICPS International conference on the physics of semiconductors, Montpellier, France: Poster contribution (2018).

20th International Winterschool Mauterndorf, Mauterndorf, Austria: Poster contribution (2018).

19th International Winterschool Mauterndorf, Mauterndorf, Austria: Poster contribution (2016).

Danksagung

Ich möchte mich recht herzlich bei allen bedanken, die mich auf dem Weg zum erfolgreichen Erstellen dieser Arbeit begleitet haben. An erster Stelle bedanke ich mich besonders bei meinem Betreuer Prof. Dr. Christian Schüller für die freundliche Aufnahme in seine Arbeitsgruppe und die hervorragende Betreuung in diesem interessanten Forschungsprojekt. Das entgegengebrachte Vertrauen und den offenen Umgang schätzte ich sehr.

Prof. Dr. Tobias Korn danke ich herzlich für seinen unermüdlichen Einsatz sowohl im Labor als auch bei fachlichen Fragen, darüber hinaus auch für das Korrekturlesen dieser Arbeit. Dieses Engagement ist nicht selbstverständlich und trug maßgeblich zum erfolgreichen Abschließen meiner Arbeit bei.

Bei Prof. Dr. Sergey Ganichev bedanke ich mich für die Übernahme der Zweitkorrektur dieser Arbeit sowie für die vielen interessanten Gespräche bei Konferenzaufenthalten.

Im Zuge seiner Masterarbeit leistete Christian Frankerl einen wichtigen Beitrag zu dieser Arbeit. Durch seine Flexibilität konnten wir trotz des defekten Cryostaten und den damit entstandenen Messpausen wichtige Ergebnisse durch die gemeinsam entwickelte Python-basierte Linienformanalyse erzielen.

Für seinen aufopfernden Einsatz bei der technischen Umsetzung vieler im Labor benötigten Aufbauten und Geräte gilt mein besonderer Dank unserem Techniker Christof Ermer. Des weiteren bedanke ich mich an dieser Stelle bei Dr. Sebastian Bange und Sebastian Krug für die tatkräftige Unterstützung bei vielen technischen Problemstellungen.

Bei meinem ehemaligen Bürokollegen Dr. Philipp Nagler bedanke ich mich für die sehr schätzenswerte Büroatmosphäre, die vielen wissenschaftlichen wie auch nichtwissenschaftlichen Gespräche sowie für das Korrekturlesen dieser Arbeit.

Ich bedanke mich herzlich bei Prof. Dr. Werner Wegscheider und Dr. Gian Salis für die Bereitstellung von hochwertigen Proben sowie für eine Einladung an die ETH Zürich und an die IBM-Research in Rüschlikon mit der Möglichkeit, dort vortragen zu dürfen. Ich erlebte inspirierende Einblicke in den dortigen Wissenschaftsbetrieb und durfte viele interessante Menschen kennenlernen. Außerdem möchte ich mich bei Prof. Dr. Dominique Bougeard für fruchtbare wissenschaftliche Diskussionen und die Bereitstellung einer wichtigen Probe bedanken.

Vielen herzlichen Dank an alle ehemaligen und derzeitigen Arbeitskollegen unseres Lehrstuhls: Dr. Christian Gradl, Johannes Holler, Michael Kempf, Sebastian Meier, Dr. Gerd Plechinger, Robin Puchert, Florian Raab, Simon Raiber, Dr. Christoph Schönhuber und Dr. Markus Schwemmer. Auch den Mitgliedern anderer Arbeitsgruppen gilt mein besonderer Dank, darunter Dr. Florian Dirnberger, Dr. Benjamin Geiger, Dr. Raphael Kozlovsky, Dr. Andreas Rabenstein sowie Dr. Michaela Trottmann.

Ich möchte mich herzlich bei Inessa Slavinskaya, Edgar Töws, Andreas Vogelsberg, Josef Wastlhuber und Richard Zumbil sowie der BKS-15-Wohngemeinschaft dafür bedanken, dass sie mir einen wichtigen Ausgleich außerhalb der Universität ermöglichten.

Zu allerletzt bedanke ich mich bei meinen Eltern Sieglinde und Stephan und meiner Schwester Verena mit Jakob und Jonah. In allen Phasen dieser Arbeit fand ich dort immer den nötigen Rückhalt.